Exfoliated Zeolite Sheets and Block Copolymers as Building Blocks for Composite Membranes

A DISSERTATION
SUBMITTED TO THE FACULTY OF THE GRADUATE SCHOOL
OF THE UNIVERSITY OF MINNESOTA
BY

Sudeep Maheshwari

IN PARTIAL FULFILLMENT OF THE REQUIREMENTS
FOR THE DEGREE OF
DOCTOR OF PHILOSOPHY

Frank S. Bates and Michael Tsapatsis, Advisors

August 2009

Acknowledgements

I would like to thank my advisors, Prof. Michael Tsapatsis and Prof. Frank S. Bates for providing me the opportunity to work in their labs. They have been a constant source of encouragement in my graduate career. Michael's calm demeanor, patience and understanding kept me motivated even during the adverse times. Frank gave me the independence to pursue my ideas. His critical feedback and commitment to excellence has made me a better scientist. Working with both of them has been a great learning experience.

During my graduate studies, I have greatly benefited from my interaction with a number of people. I am indebted to Sandeep Kumar for his immense help with TEM imaging. I would like to thank Maybelle Woo, Zhiping Lai, Kevin Davis, Adam Meuler, Alhad Phatak and Qiang Lan for intial training in lab. I am grateful to my collaborators in Texas A&M, Prof. Dan Shantz and Edgar Jordan, and Dr. Sonjong Hwang at Caltech for NMR results. I appreciate the help of my past and present colleagues: Josh Sheffel, Alex Lee, Rajiv Ranjan, Jungkyu Choi, Shubojit Ghosh and Michael Bluemle. It was fun sharing the office space with past and present inmates of Room 461.

Life outside work has been enjoyable, thanks to my friends and past roommates (especially Nazish Hoda). I enjoyed playing cricket with the members of Continental Cricket Club. My heart goes out to thank Nupur for her love and unwavering support over the past four years. Her encouragement and faith in me, especially over the last few difficult months, kept me going.

Last, and the most important, I would like to thank my family members. I would not have been able to pursue my graduate studies without the invaluable support of my mother, who took care of all the responsibilities in very challenging times. My father has been the real source of motivation for getting a PhD degree.

To my Parents

Abstract

Mixed matrix materials, comprising of zeolites incorporated in suitable matrix (polymeric or inorganic), are promising as future membrane materials with high permselectivity. However, they suffer from the drawback of low productivity due to increase in the membrane thickness by incorporation of micron-sized zeolites crystals as well as the low-permeability matrices employed currently. Nanocomposite membranes, consisting of thin zeolite sheets (~2 nm) embedded in an appropriate matrix, can provide a solution to this problem. This thesis addresses some of the material challenges to make such nanocomposite membranes.

A high permeability polymer was synthesized by combining the glassy polystyrene (PS) with the rubbery polydimethylsiloxane (PDMS) in a block copolymer architecture. The mechanical toughness of the material was optimized to facilitate the fabrication of thin free standing films and its gas transport properties were evaluated. The PS-PDMS-PS triblock copolymers were successfully hydrogenated for the first time to obtain the PCHE-PDMS-PCHE triblock copolymers (PCHE stands for polycyclohexylethylene). The hydrogenation reaction proceeded without any polymer chain breaking and the resultant polymer showed some interesting, rather unexpected thermodynamic properties. These polymeric materials are potentially useful as the matrix of nanocomposite membranes.

Highly crystalline zeolite sheets were obtained by exfoliation of zeolite lamellae. Preservation of crystal morphology and pore structure, which presents a major challenge during the exfoliation process, was successfully addressed in this work by judicious choice of operating conditions. Lamellae were exfoliated by surfactant intercalation and subsequently melt processing with polymers, resulting in polymer nanocomposites containing thin zeolite sheets (~2.5 nm) with well preserved pore structure. A method to obtain polymer-free exfoliated sheets was also developed to facilitate the fabrication of inorganic composite membranes. These zeolite sheets can be used as the selectivity-enhancement additive in composite membranes.

Table of Contents

List of Tables

List of Figures

1. Introduction

1.1 Membranes for Gas Separation

Isolation of gases is required in varied applications ranging from daily mundane products to very specialized ones. The market for gas separation is huge and growing. To give an idea, six of the top ten chemicals produced in United states (nitrogen, oxygen, ethylene, ammonia, propylene, and chlorine) are gaseous under usual conditions[1] and require separation processes to put them into meaningful use. With the advent of technology and growing environmental concerns, demands for efficient separation processes to produce high purity hydrogen and sequester carbon dioxide have emerged.

Various technologies have been employed in industry for gas separations. Cryogenic distillation, which uses difference in the boiling point of condensed gases, is the leading technology for the fractionation of air to produce oxygen.[2] Techniques based on differential adsorption properties of gases like pressure swing adsorption (PSA), have also been exploited for few gases. However, these techniques suffer from one or more drawbacks like large capital costs, and high operating costs due to energy intensive process, etc.[2] Membrane based separations, which rely on differences in the diffusivity and solubility of gases, are being seen as the promising technology for the future[2] due to lower energy requirements and simplicity of the operation. The membrane market was about $150 million in the year 2000 and is rapidly growing.[3] It is believed that among the various technologies, membranes have perhaps the greatest potential for future improvement by innovations in membrane material, process and system design. The main focus of this research is to develop advanced membrane materials for gas separation applications.

1.2 Polymers and Polymer-Zeolite Composites as Membrane Materials

A membrane material should have high selectivity for efficient separation and high permeability for large throughput. Additionally, it should be easily processable, scalable and have reasonable mechanical, thermal and chemical stability for smooth operation. Polymeric materials have dominated the membrane industry due to features such as low price, easy processability, mechanical robustness and flexibility. The real breakthrough was achieved by the formation of asymmetric membranes by Loeb and Sourirajan[4] in 1960's consisting of a very thin selective dense skin layer supported over a porous layer, which enabled high gas flux through the membrane with reasonable selectivity. Today, the state of art polymeric membranes are formed as asymmetric hollow fibers with thin skin layers (~100nm) as shown in Figure 1.1.

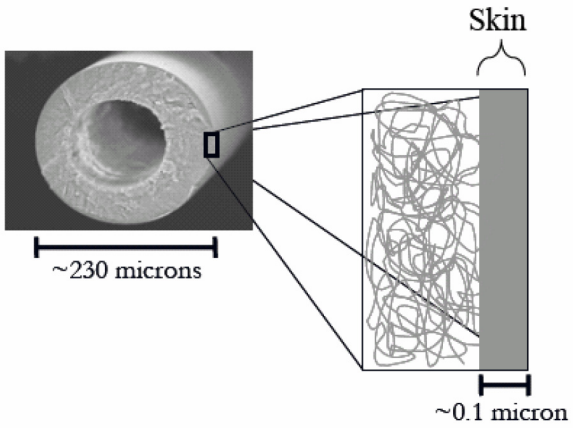

Figure 1.1. Asymmetric hollow fiber membrane for gas separation applications. The magnification on the right shows a schematic of asymmetric structure consisting of a dense skin layer on top of a porous structure.

While polymeric membranes have grown significantly in nitrogen production, their usages in other gas separations have been limited to small capacity low purity applications. This is due to the fact that polymeric materials have an internal tradeoff between permeability and selectivity. In 1991, Robeson complied gas transport data for various polymeric materials and plotted them on a selectivity vs. permeability scale, showing an upper bound on the performance of polymeric membranes.[5] Despite

numerous efforts in exploring new polymers, this upper bound has shifted very little in the last two decades.

Unlike polymeric materials, molecular-sieves or zeolites are well known for their very high selectivity. These inorganic materials have well defined molecular-sized pore channels which enable them to separate molecules based on size, shape or affinity differences. However, pure zeolite membranes pose processability issues. These materials lack the mechanical toughness and flexibility of polymers and are difficult to scale up for large scale gas separation applications based on current fabrication methods.

Addition of zeolite to polymeric membranes offers hope that the internal tradeoff between permeability and selectivity of polymeric materials may be overcome. Such membranes are often called mixed-matrix membranes or composite membranes and have been the subject of intense research over the last decade. Polymer-zeolite composite materials are expected to combine the useful properties of these two materials (processability, mechanical toughness from polymer and high selectivity from zeolites), to provide next generation membranes for an in-kind replacement for polymeric gas separation membranes.

There have been numerous attempts to disperse various zeolites in suitable polymer matrices to enhance performance[6-11] and some progress has been made in the last decade.[12] But many new challenges have been identified. One of the major challenges is the formation of mixed matrix membranes into asymmetric hollow fibers (as shown in Figure 1.1). The zeolite crystals used for making these membranes are micron-sized, which rules out the formation of thin skin layers (~100 nm). Increasing the thickness of skin layer to accommodate micron-sized zeolites is unattractive as it results in reduction of gas flux through the membrane. Another key limitation is the high amount of zeolite required (20-40 wt %) to obtain significant selectivity improvements. The isotropic shape of zeolite particles necessitates larger loading to increase tortuosity (and hence the diffusion path length) and retard transport of one of the molecules. At such a high zeolite loading, the composite membrane loses its mechanical strength and ease of

processability. The flux of the desired gas also suffers adversely as a result of higher zeolite loadings.

Layered zeolite materials consisting of nanometer-thick sheets with suitable pore channels can provide the material to replace the isotropic micron-sized zeolite crystals in mixed matrix membranes. The concept is depicted in the schematic shown in Figure 1.2. The ultra-thin layers, produced by exfoliation of layered zeolites into individual sheets, can be accommodated in the thin skin layer of polymeric hollow fibers without increasing the thickness. The high aspect ratio of these ultra-thin sheets will induce significant tortuosity even at low zeolite loadings, thereby providing the selectivity enhancement. Moreover, dispersion of nanometer-thick layers in polymers is known to enhance the mechanical toughness of the polymeric materials.[13] Thus, replacing the micron-sized isotropic zeolite crystals with nanometer-thick porous zeolite layers can solve some of the current issues preventing the development of mixed matrix membrane technology.

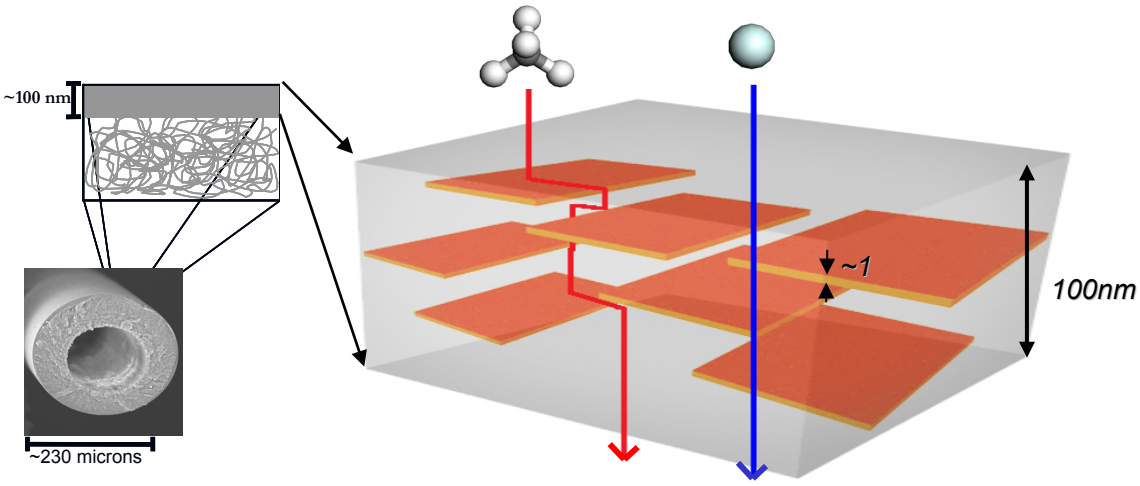

Figure 1.2. Cartoon illustrating the idea of nanocomposite membrane. Layered material dispersed in skin layer will distinguish gas molecules based on their size.

This work has focused on developing the building blocks (viz. nanometer thick zeolite layers and polymer matrix) for 'polymer-layered zeolite' composite membranes. In this dissertation, I present a process methodology to exfoliate a layered zeolite into

nanometer-thick sheets, with emphasis on preserving the high aspect ratio and pore structure of zeolite during exfoliation process. The resultant material can be useful for the fabrication of hydrogen selective mixed matrix membranes.

It is necessary to balance the transport properties of the matrix and the zeolite sheets to optimize the performance of the mixed matrix membrane.[14] Since, the choice of layered zeolite (and hence its transport properties) is often very restrictive due to limited number of candidates, an ability to systematically vary the gas transport property of the matrix can help in achieving the required balance. A novel block copolymer system was designed for this purpose. Although, the initial motivation was to develop a polymer system with tunable gas transport properties, the block copolymer was found to be an attractive candidate for studying basic polymer mixing thermodynamics. A detailed study on the synthesis and thermodynamic properties of the block copolymer is presented.

1.3 Mixed Matrix Membranes with Inorganic Matrices

Inorganic membranes are attractive for high temperature, high pressure separation applications, where polymeric materials cannot be used. One such application that has gained prominence in the face of growing environmental concern is the separation of carbon dioxide from hydrogen in the turbine fuel feeds in coal-based gasification plants. As stated in the NRC report on Novel Approaches to Carbon Management, "there is a need for novel membranes that can perform the separation of CO_2 and H_2 at high temperatures and pressures."[15] Several high temperature hydrogen selective membranes made of zeolites, silica, metal and other materials have been reported.[16] However, despite their promising separation properties, these membranes suffer from either high fabrication costs, difficulties in scale up or long term stability limitations. A mixed matrix membrane using nanometer-thick zeolite sheets with appropriate pore size and an inorganic matrix can provide the required solution. The concept is similar to the polymer-layered zeolite membranes described in previous section, except for the replacement of polymer matrix by inorganic matrix to enable usage at high temperature and pressure. A

scalable method to make such membranes on appropriate porous support is presented in this thesis.

1.4 Thesis Outline

The remaining part of this dissertation has been divided into 5 chapters with the focus on developing building blocks for mixed matrix membranes. Chapter 2 and 3 describe block copolymer materials which can be useful as a continuous phase of mixed matrix membranes. Chapter 4 and 5 deal with swelling and exfoliation of a zeolite to obtain thin (~2 nm) porous sheets, which can be used as permselective additives in the mixed matrix membranes.

In chapter 2, we discuss the advantages of employing block copolymer as the matrix in composite membranes. After a brief introduction to block copolymers and their phase separated morphologies, a discussion on tuning the matrix gas transport properties using block copolymer has been presented. Finally, we explore the use of polystyrene-polydimethylsiloxane system as the polymer of choice. An experimental study on the synthesis and gas transport properties of this block copolymer has been presented.

Chapter 3 presents an experimental study on the hydrogenation of polystyrene-polydimethylsiloxane block copolymers described in chapter 2. This study was undertaken to examine the feasibility of hydrogenating polystyrene-polydimethylsiloxane block copolymers. Successful hydrogenation prompted us to study the mixing thermodynamics of the constituent blocks in some detail.

Chapter 4 discusses the swelling of layered zeolite MCM-22(P) to increase the interlayer spacing and facilitate the fabrication of mixed matrix nanocomposite membranes with polymer. Special attention has been given to preserve the layered morphology and pore structure of the zeolite during the swelling process. A series of characterization techniques have been employed to validate the structural preservation and results have been compared to previous studies reported in the literature.

Chapter 5 presents a process to exfoliate swollen zeolite precursor (described in chapter 4) into individual nano-thick porous sheets. Potential usage of exfoliated sheets in polymeric and inorganic membranes has been discussed and preliminary results on fabrication of thin supported films using these materials have been presented.

Chapter 6 provides a summary of the progress described in chapters 2-5 and suggests possible future directions to make mixed matrix membranes using these materials.

2. Block Copolymer as Matrix of Composite Membrane

Block copolymers are interesting materials due to their ability to combine chemically distinct, thermodynamically incompatible polymers with different properties. In this chapter, the use of block copolymers as the matrix component of polymer-layered zeolite composite membranes will be explored.

A high permeability matrix consisting of polystyrene (PS) and polydimethylsiloxane (PDMS) blocks, was synthesized. The relative amounts of PS and PDMS were tuned to obtain a lamellar microstructure. Block architecture and molecular weight of the polymer were optimized to obtain a tough material which could be casted into free standing films. The gas transport properties of the resulting polymer were evaluated.

The chapter begins with an introduction to block copolymers and their microphase separated morphologies. The potential advantages of these materials as membrane matrices are discussed. Finally, a detailed experimental study on the synthesis and properties of PS-PDMS block copolymer system is presented.

2.1 Background

Block Copolymers are macromolecules composed of sequences, or blocks, of chemically distinct repeat units.[17] The covalent linkages between the repeat units prevent phase separation on a macroscopic scale. However, the inherent incompatibility of the constituent blocks leads to phase separation and self-assembly on mesoscopic length scales (5-100nm) resulting in various complex nanostructures.[18]

The key to making well-defined block copolymers was the development of the living anionic polymerization method[19], which allowed synthesis of these polymers with narrow weight distributions and compositional uniformity. With further advancements in synthesis chemistry leading to the development of controlled radical polymerizations[20] and ring-opening polymerizations[21] techniques, novel block copolymer systems with complex structures could be realized.

2.1.1 Phase Behavior of Polymer Mixtures

Miscibility of polymer blocks has a controlling influence over the properties of polymer blends and block copolymers. The Flory-Huggins equation provides the criteria to describe the phase behavior of polymer mixtures:

$$\frac{\Delta G_m}{k_B T} = \frac{f_A}{N_A} \ln f_A + \frac{f_B}{N_B} \ln f_B + \chi_{AB} f_A f_B \qquad (2.1)$$

where, ΔG_m is the free energy of mixing of species A and B, k_B is the Boltzmann's constant, T is the absolute temperature, N_A and N_B are the number of repeat units in the polymers A and B, f_A and f_B are the volume fractions of A and B, and χ_{AB} is the Flory-Huggins interaction parameter which is the free energy cost per monomer, of contacts between A and B.[18] A positive value of χ_{AB} indicates repulsion between A and B and results in a positive enthalpy of mixing that favors phase separation. For polymers, N_A and N_B are large, diminishing the effect of first two terms which describe the favorable entropic contribution to mixing. The enthalpy term ($\chi_{AB} f_A f_B$) thus becomes the dominant contribution to the free energy. For most polymer mixtures, this term is

positive, indicating that mixing is unfavorable. As a result, most polymer blends tend to phase separate macroscopically. However, in block copolymers, the covalent bond between two such disliking polymers prevents the macrophase separation. The phase separation is limited to the length scale of the polymer chains (~5-100 nm), resulting in various periodic geometries. The extent of separation and the geometry achieved depends on the interplay of a number of parameters like χ_{AB}, f_A, and N (overall degree of polymerization).

2.1.2 Ordered Morphologies in Block Copolymers

AB diblocks are the simplest of block copolymers consisting of a chain of type A monomers covalently bonded to a chain of type B monomers. As discussed above, microphase separation in block copolymer takes place due to interplay of enthalpic (described by χ_{AB}) and entropic effects (described by N^{-1}). The product $\chi_{AB}N$ thus is the relevant parameter to sum up both effects. Above a minimum value of $\chi_{AB}N$ (>>10), the constituent blocks segregate into a variety of equilibrium morphologies. The identity of the equilibrium morphology depends mainly on f_A and $\chi_{AB}N$.[22,23] A series of quantitative predictive work[22,24-27] has led to a theoretical polymer phase diagram for diblock systems that agrees well with experimental studies[23] (see Fig 2.1). Spherical (Q_{Im3m}), Cylinderical (H), and Lamella (L) are the three most prevalent morphologies identified in the majority of AB diblock copolymer systems. The phase behavior of symmetric ABA triblock copolymers is identical to that of homologous AB diblock copolymers.[28] However, several new fascinating morphologies begin to appear in block copolymers with three or more distinct blocks.[18]

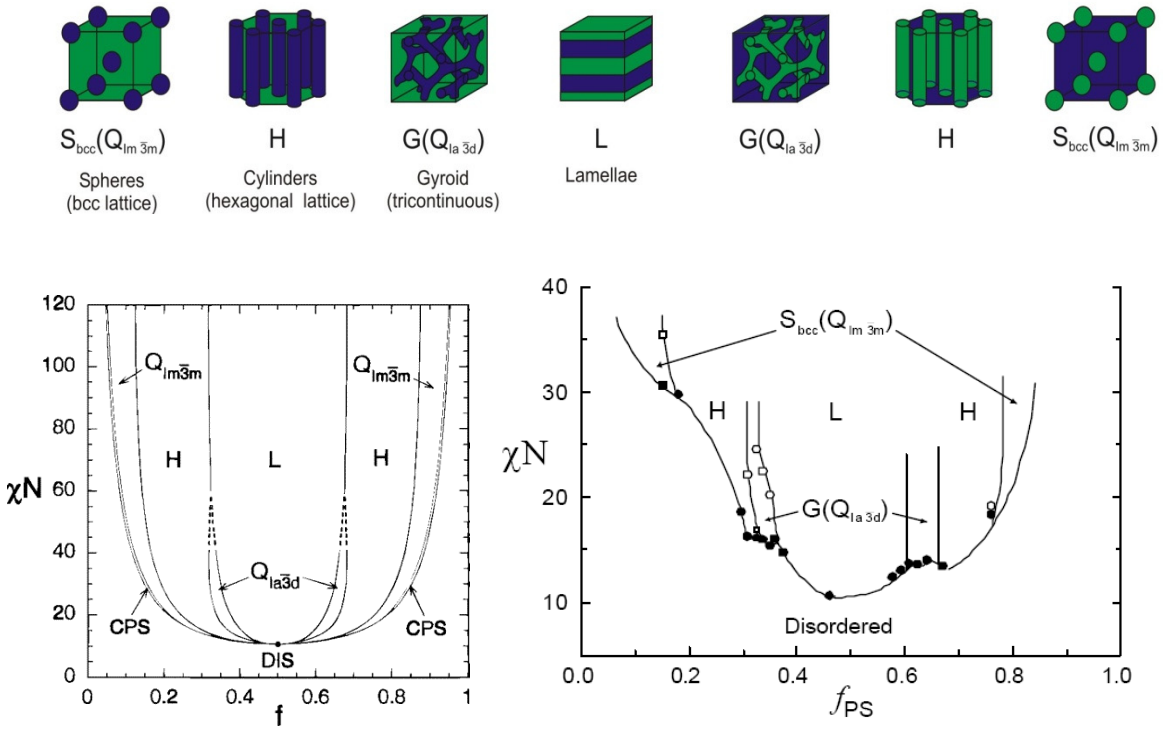

Figure 2.1. Morphologies and phase diagram for AB diblock copolymer. Schematic of various morphologies shown by an AB diblock copolymer are shown on top. Theoretical (left, reproduced from Matsen and Bates[26]) and experimental (right, reproduced from Bailey[29]) phase diagrams are shown on bottom.

2.1.3 Effect of Block Architecture and Molecular Weight on the Mechanical Toughness of Block Copolymers

The mechanical properties of block copolymers depend on a number of factors like molecular weight, block chemistry, asymmetry of end blocks,[30] chain architecture[30-32], microphase-separated morphology[32], etc. Any application of block copolymers requires tuning of one or more of these parameters to yield the material with desired mechanical behavior.

Constituent blocks play an important role in determining the mechanical properties of block copolymer. For example, glassy blocks like polystyrene increase the elastic moduli but introduce brittleness in the material. On the other hand, rubbery blocks

like polyisoprene allow higher strains without brittle failure, but reduce the elastic moduli of the polymer.

Molecular architecture affects the physical properties of block copolymer in a fundamental manner. ABA triblock copolymers (with glassy A and rubbery B blocks) are known to be much tougher than the corresponding AB diblocks due to enhanced interconnectivity of microdomains by means of bridging and looping configurations.[33] For example, the polystyrene-polyisoprene (A-B) diblock copolymers can be brittle solids or liquids depending on relative amount of A and B blocks[34] while the corresponding triblock copolymers (ABA) are much tougher i.e. incorporate high modulus and elasticity, and find applications in footwear, roughing compounds[31], etc. Pentablocks (ABABA) are known to be even tougher than triblocks due to further extensive connectivity among the domains (through bridging and/or knotting).[31,35]

The order of blocks (ABA vs BAB) also plays an important role in ultimate toughness and other mechanical properties. ABA block copolymers with a rubbery B block have higher tensile modulus than BAB block copolymers at the same molecular weight and volume fraction, due to pinning of the rubbery B chains at both ends by the glassy A chains.[36] The existence of trapped entanglements in ABA architectures contributes to the elastic behavior because they have much less mobility than the B blocks in a BAB architecture.[36]

In general, tensile strength and ultimate elongation increase with molecular weight for polymers in general due to increased extent of networking, crosslinking and entanglements.[37-39] Diblock copolymers, which are very brittle at low molecular weight, become tough at sufficiently high molecular weights.[39]

2.2 Block Copolymers for Matrices of Composite Membranes

Block copolymerization provides a facile way to combine two or more chemically distinct polymer blocks with very different properties. Such flexibility can be used to tune the gas transport property of the matrix as per the requirement. For example, a high gas

permeability rubbery polymer and a low permeability glassy polymer can be combined in block copolymer architecture to obtain a material with intermediate gas permeability.

Block copolymerization can provide matrices spanning a wide range of gas permeabilities by using different block combinations. Within a block copolymer system, the gas transport properties can be further tuned by adjusting the relative amount of constituent blocks. Thus, gas permeability of the matrix can be varied in a controlled fashion. Several authors have proposed a need to balance the gas transport properties of matrix with that of zeolite in order to enhance the separation performance of the resulting mixed matrix membranes.[14,40] A systematic variation of matrix properties, made possible by block copolymerization, can help achieving such a balance.

Block copolymer microstructure can also help in orienting the zeolite layers. For optimal performance of polymer-layered zeolite mixed matrix membrane, the zeolite layers should be oriented such that their thinnest dimension lies along the gas flow direction. Such an orientation provides maximum tortuosity for the transport of undesirable gas and also allows constraining the zeolite layers within the thin skin layer of hollow fiber membrane. Block copolymers with lamellar microstructure can help achieving such an orientation if the zeolite layers can be made affine to one of the blocks. Such an affinity would promote the sequestration of layers in that block to minimize the surface energy and will result in desirable orientation. The concept has been illustrated in Figure 2.2

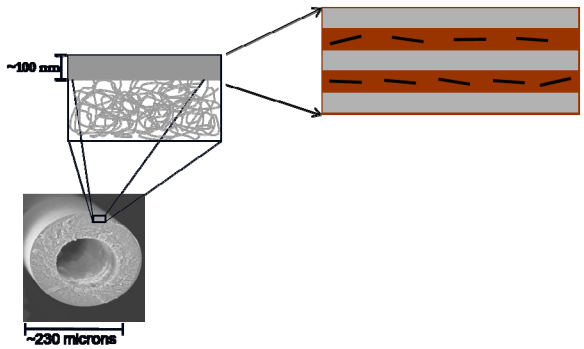

Figure 2.2. Schematic showing preferred orientation of zeolite layers by their sequestration in one of the block of a lamellar forming block copolymer.

2.2.1 Polystyrene-polydimethylsiloxane Block Copolymers as Matrix

For this work, polystyrene (PS) and polydimethylsiloxane (PDMS) were chosen as the constituent blocks for the polymer matrix. PDMS has high gas permeability but low elastic modulus, while PS is a glassy material with high elastic modulus. Combination of PS and PDMS blocks can provide a material with reasonable toughness and permeability. Such a high permeability matrix was anticipated to be attractive for separation applications, because its combination with layered zeolites can provide a composite membrane with high flux and high selectivity. Details on synthesis and characterization of this material are presented below.

2.2.1.1 Experimental Section

Block copolymer synthesis

PS-PDMS diblock copolymers were synthesized by sequential anionic polymerization of styrene and hexamethylcyclotrisiloxane (D_3) monomers, followed by chain termination with chlorotrimethylsilane. For synthesis of PS-PDMS-PS triblock copolymer, the chain termination step was replaced by coupling using dichlorodimethylsilane.

Styrene monomer (Aldrich) was degassed by three freeze-pump-thaw cycles followed by twice stirring with dibutylmagnesium (1 hr each) before finally distilling into a flamed burette. D_3 monomer (Aldrich) was degassed in a similar fashion followed by stirring over calcium hydride (4 hrs) and dibutylmagnesium (1 hr), and final distillation into a flamed burette.[41] D_3 monomer was held at 90 °C in a liquid state during these operations using a silicon oil bath. Cyclohexane was purified by sequential passage through columns of activated alumina and Q5 catalyst (Engelhard). Tetrahydrofuran (THF) was purified by passing through two activated alumina columns.[42] Solvents were collected into sealed flasks under anhydrous conditions using Schlenk techniques.

Anionic polymerization was conducted under an argon atmosphere in a Pyrex reactor fitted with Teflon ferrules and screw caps. Styrene was initiated in cyclohexane at

40 °C using sec-butyllithium; the presence of polystyryl anions was indicated by a deep orange color. Polymerization proceeded for six hours, after which a small aliquot was extracted from the reactor for later analysis. Subsequently, D_3 monomer was added to the reactor, and the contents were stirred for 12 hrs at 25 °C. Prior work suggests complete crossover to siloxyl anions under these conditions.[41] However, polymerization of D_3 is very slow in nonpolar solvents such as cyclohexane[43], and, therefore, polar solvent THF was added to make a 50:50 mixture with the cyclohexane. The solution became colorless immediately after the addition of THF, indicating the onset of D_3 polymerization. The D_3 monomer was polymerized for 1.5 hours (~ 33% conversion), and the growing polymer chains were either terminated by adding tenfold excess of chlorotrimethylsilane to obtain PS-PDMS diblock copolymer, or were coupled by adding a stoichiometric amount of dichlorodimethylsilane to obtain PS-PDMS-PS triblock copolymers. Conversion of D_3 monomer was kept low to prevent side reactions and oligomer formation, which become competitive with the desired polymerization at higher conversions. After stirring for 1.5 hours with chlorotrimethylsilane or dichlorodimethylsilane, the reactor was opened to atmosphere. Note that sequential anionic polymerization cannot be used to add a third PS block to make triblock copolymer, as the siloxyl anions cannot initiate the styrene polymerization.[44] Illustrations of the resulting molecular structures are shown in Figure 2.3. The polymers were recovered by solvent evaporation, re-dissolution in THF, and precipitation into a 50/50 methanol/isopropanol mixture before finally drying to constant mass at 80 °C under vacuum (~10^{-1} torr). Polystyrene homopolymer impurity was detected in all the block copolymer syntheses due to some termination of the first block. This was removed by titrating a 2% polymer solution in dioxane with a 50:50 mixture of methanol/water at room temperature until it turned cloudy.[43,45] The block copolymer formed a floating mass, while the homopolymer remained dissolved in the solution.

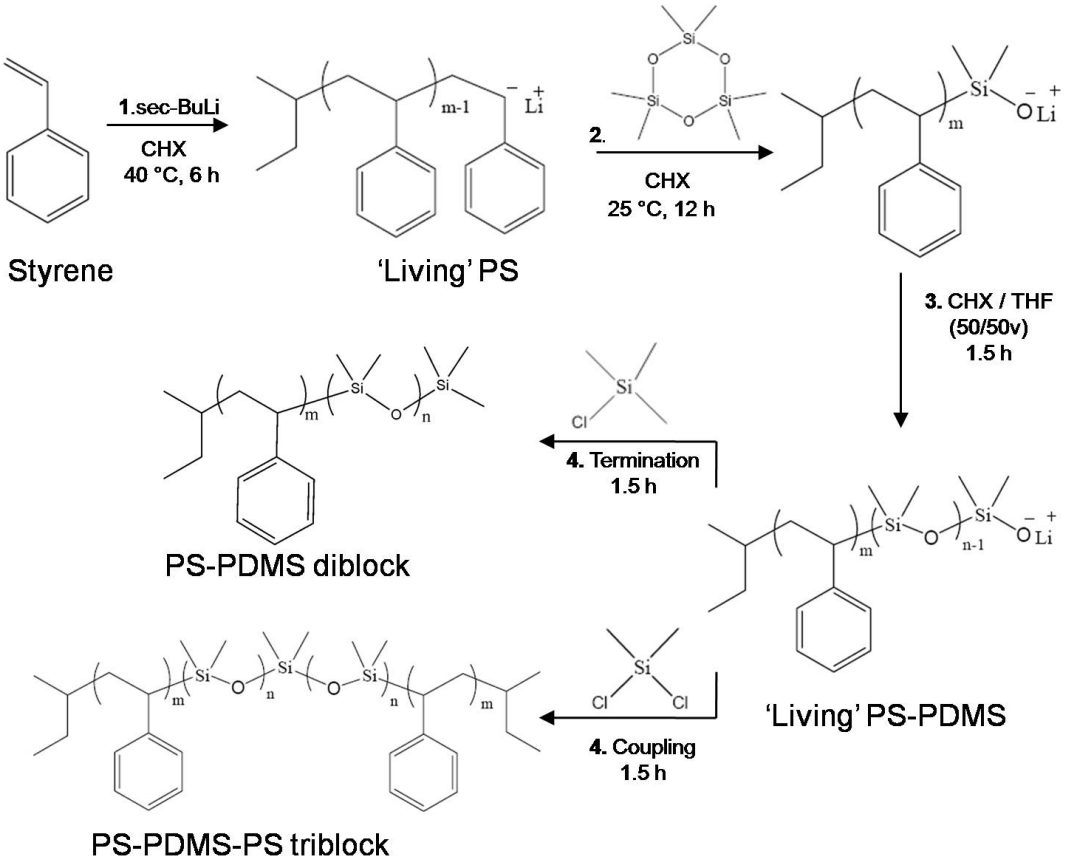

Figure 2.3. Schematic of sequential anionic polymerization for the synthesis of PS-PDMS diblock and PS-PDMS-PS triblock copolymers.

Film Casting

Free standing films of block copolymers were made to test the gas transport properties. A 5wt% solution of polymer in a suitable solvent (typically toluene) was spread on a Teflon surface followed by drying at room temperature. After overnight drying, the films were peeled off the Teflon surface and annealed at 100 ˚C for 24 h in a vacuum oven.

Characterization

The compositions of the block copolymers were determined from ^{1}H NMR spectra collected with a 300 MHz Varian instrument using deuterated chloroform as the

solvent. PS and PDMS volume fractions were calculated using the homopolymer densities at 140 °C.[46]

Number average molecular weights (M_n) of all specimens were calculated using the M_n value for the PS block (extracted during the synthesis), measured using a PS-calibrated SEC trace. Combining the composition (NMR) and M_n for PS block yielded the overall M_n. SEC was also used to determine the polydispersity of the block copolymers.

SAXS experiments were carried out to characterize the morphology of the block copolymers. Experiments were conducted on a home built system[47] using Cu Kα radiation and a Siemens area detector located at a distance of 230 cm from the sample. Samples were shear aligned[48] using a reciprocating shear device[49] and scattering patterns were collected for 30 min at 25 °C. The morphology was deduced from the ratio of primary peak position to higher order peak positions.

TEM was employed for direct visualization of the block copolymer morphologies using a JEOL 1210 microscope operated at an accelerating voltage of 120 kV. Samples were cryo-microtomed to obtain 50-80 nm thick slices using a diamond knife operated between -130 to -145 °C on a Reichert Ultracut S Ultramicrotome.[47] No staining was necessary, as the silicon in the PDMS block provides adequate contrast for imaging.[43]

Gas Permeation

The gas permeation data were obtained by the constant volume/variable pressure method.[50] This method measures the pressure rise as a function of time in a constant downstream volume to calculate the permeability:

$$P = \frac{V_m l V}{A R T \Delta p} \frac{dp}{dt}$$

where, V_m is the molar volume at standard temperature and pressure, l is the membrane thickness, V is the volume of permeation cell, A is the membrane area, R is the universal

gas constant, T is temperature, Δp is pressure difference across membrane and dp/dt is the slope of pressure versus time curve recorded during testing. Samples were masked for gas permeation measurement following the technique of the Moore et. al.[51] Experiments were performed at 35 ˚C with atmospheric feed-side pressure. The permeate-side was evacuated overnight with a dry pump to degas the sample to a pressure $<10^{-2}$ torr.

2.2.1.2 Results and Analysis

Molecular Charcaterization

Two PS-PDMS diblock and three PS-PDMS-PS triblock copolymers containing 40-60 vol% of polystyrene were synthesized. The samples were designed to obtain a lamellar morphology in each case. The molecular characterization data for all the polymers is listed in Table 2.1.

Table 2.1: Polymer Characterization Results

Sample	10^3 M_n (g/mol)[a]	f_{PS}[b]	PDI[c]
SD-1	20.0	0.54	1.08
SD-2	24.9	0.62	1.06
SDS-5	16.7	0.44	1.07
SDS-1	31.0	0.42	1.1
SDS-9	138	0.46	1.08

[a]As calculated from mass fraction and M_n of precursor PS block. [b]Volume fraction of PS calculated from NMR spectroscopy. [c]From SEC based on polystyrene standards.

Representative ^{1}H NMR spectrum for a block copolymer with PS and PDMS blocks is shown in Figure 2.4. The aromatic protons of the benzene ring in styrene resonate at about 7 ppm while the methyl protons appear around 2 ppm. Protons from the

methyl group of siloxane units resonate at 0 ppm. The NMR spectra of diblock and triblock copolymers are identical because the same types of protons are present in both.

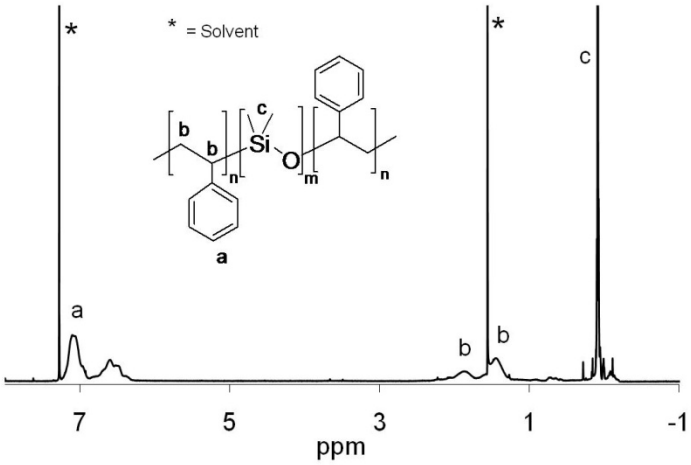

Figure 2.4. Representative ^{1}H NMR spectrum of a block copolymer with polystyrene and polydimethylsiloxane blocks

Representative SEC traces of the PS-PDMS diblock copolymers and of the corresponding PS block (extracted during synthesis) are shown in Figure 2.5. A small secondary peak between 21-22 min elution time in the trace for PS (trace a) is due to an artifact (coupling of PS chains) introduced while extracting the aliquot and is not representative of the PS chains in the reactor. Trace b for the PS-PDMS diblock copolymer shows the presence of a small amount of polystyrene homopolymer impurity (broad shoulder between 23-24 min), due to some termination of the first block. This is removed using the precipitation technique described in previous section. The final PS-PDMS diblock copolymer is free of such impurities and shows a single symmetric peak as depicted by Trace c.

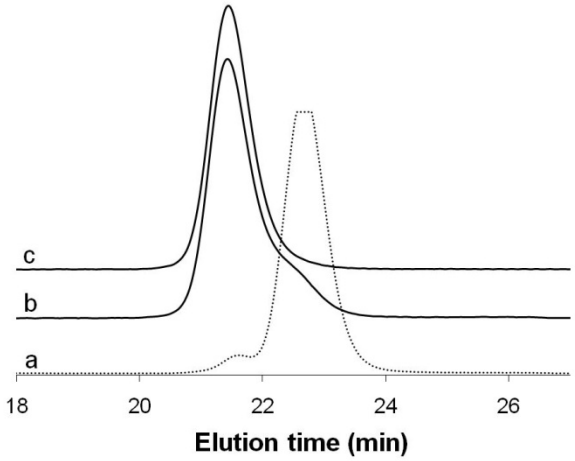

Figure 2.5. Size exclusion chromatograph of a) polystyrene aliquot, b) PS-PDMS diblock copolymer obtained after polymerization and c) PS-PDMS diblock copolymer purified by precipitation using dioxane-methanol/water mixture to remove polystyrene homopolymer impurity. Curves have been shifted vertically for clarity.

SEC traces for the PS-PDMS-PS triblock copolymer sample, SDS-5, is shown in Figure 2.6. The polystyrene homopolymer impurity (visible in Trace b) present in triblock copolymer is removed using the precipitation technique. No diblock impurities were visible in SEC traces, indicating nearly complete coupling of diblock chains by dichlorodimethylsilane. However, the SEC trace for the sample of highest molecular weight (SDS-9) revealed the presence of diblock impurities (~9%) along with polystyrene homopolymer impurities (~5%) (Figure 2.7). At higher molecular weights, the diblock copolymer chains are longer and require greater time to diffuse to positions where they can couple together. The presence of diblock impurity was probably due to insufficient time for this diffusion. The precipitation technique described earlier was ineffective in removing the polystyrene impurities for this sample due to the higher molecular weight of these impurities, which reduced their solubility and caused their precipitation along with block copolymer. No further attempts were made to remove the diblock and homopolymer content, as small amounts of these materials were not expected to significantly influence the morphology or gas transport properties of the triblock copolymer.

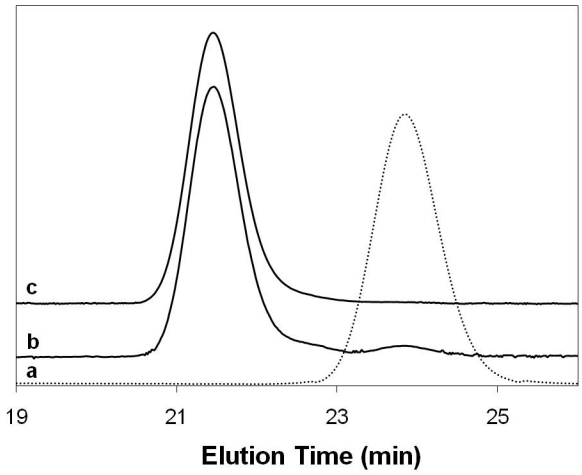

Figure 2.6. Size exclusion chromatograph of a) polystyrene aliquot, b) PS-PDMS-PS triblock copolymer (SDS-5) obtained after polymerization and c) PS-PDMS-PS triblock copolymer purified by precipitation using dioxane-methanol/water mixture to remove polystyrene homopolymer impurity. Curves have been shifted vertically for clarity.

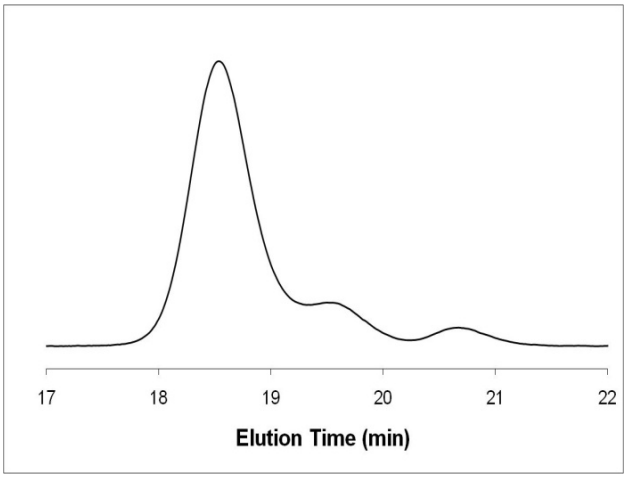

Figure 2.7. Size exclusion chromatograph of triblock copolymer, SDS-9. Two small peaks are due to diblock (19-20min) and homo polystyrene (20-21 min) impurities.

SAXS and TEM

The morphologies of the polymers were characterized using SAXS and TEM. The 2-D SAXS data obtained at 25 °C were integrated azimuthally to yield the intensity (I) as a function of scattering wavevector $q = (4\pi / \lambda)\sin(\theta / 2)$, where θ is the angle between

the incident x-ray and scattering planes and λ is the wavelength of the incident x-ray, as shown in Figure 2.8. Two reflections are clearly evident in the data obtained from all the samples at relative q values 1:2, indicating a lamellar morphology. For the SD-2 sample, three reflections are visible at relative q values 1:2:3, indicating long range alignment of lamellae in this sample. However, for SD-1 and SDS-9, the two reflections are at relative q value of 1:3. This is probably due to the nearly symmetric composition of PS and PDMS blocks in these polymers (see table 2.1), which results in extinction of the middle peak (at $q/q^* = 2$).[52] However, based on the volume fractions of PS, a lamellar morphology is expected for these polymers and the SDS-9 sample was confirmed to be lamellar by direct TEM visualization (Figure 2.9).

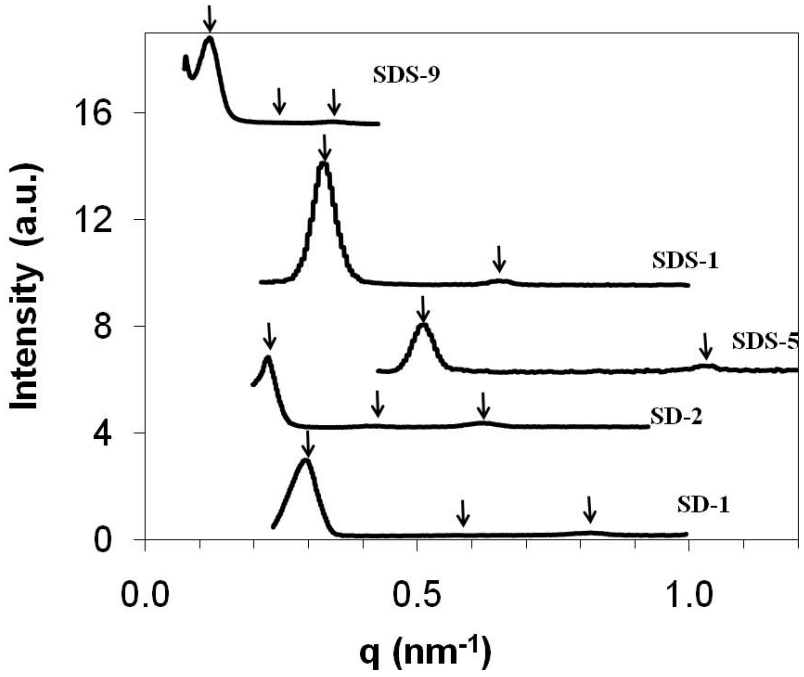

Figure 2.8. 1-D SAXS profiles obtained from shear aligned diblock and triblock copolymers of polystyrene and polydimethylsiloxane at 25 °C. See table 2.1 for nomenclature. The vertical arrows denote peak locations expected for a lamellar microstructure. Curves have been shifted vertically for clarity.

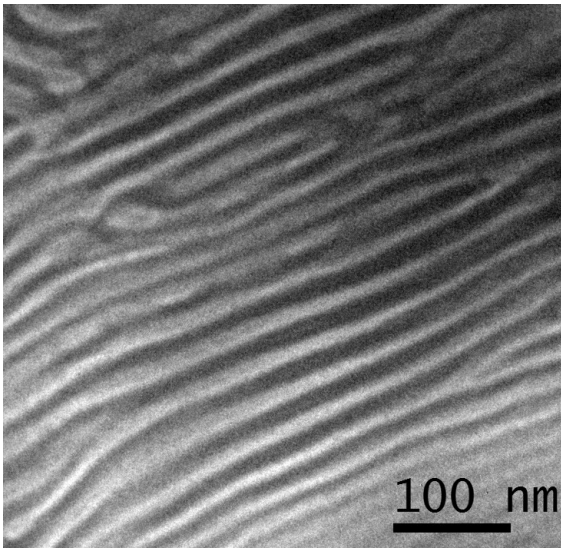

Figure 2.9. TEM image of sample SDS-9 indicating a lamellar morphology of the block copolymer. The dark regions correspond to PDMS domains while bright regions represent PS domains. PDMS appears darker due to elemental contrast (Z-contrast) from silicon atoms.

Film Casting and Gas Permeability

Attempts to make films of diblock copolymer were unsuccessful. The materials were found to be very brittle and cracked severely during solvent evaporation following the casting of the polymer solution. As discussed in section 2.1.3, ABA triblock copolymers with rubbery B block are much tougher than corresponding AB diblock copolymer. Accordingly, PS-PDMS-PS triblock copolymers were expected to have improved mechanical toughness. SDS-5 and SDS-1 triblock copolymer samples with molecular weights comparable to that of SD-1 and SD-2 diblock copolymers were casted into thin films. These films did not show any cracking during solvent evaporation. However, they broke easily upon peeling from the Teflon surface. To improve the toughness further, a triblock copolymer with higher molecular weight was made. High molecular weight polymers are known to be tougher due to increased polymer chain entanglements.[37,38] Sample SDS-9 with a total molecular weight of 140000 was found to be tough enough to make free standing thin films.

Films of sample SDS-9 were tested for gas transport properties. The permeability data is presented in Table 2.2. For reference, permeability data of a commercial gas separation polymer, polysulfone, has also been shown. The permeability of the triblock copolymer is one to two orders of magnitude higher than polysulfone, providing a very high permeability matrix for composite membranes.

Table 2.2. Gas permeability of SDS-9 triblock copolymer and polysulfone

	Permeability (in 10^{-10} Barrer*)	
Gas	**SDS-9**	**Polysulfone**
He	136	12.6
H_2	218	10.3
N_2	61	0.24
O_2	138	1.37
CO_2	643	5.68

*1 Barrer = 10^{-10} (cm^3 STP) cm cm^{-2} s^{-1} $cmHg^{-1}$

The gas permeability of a lamellar forming block copolymer is influenced by the orientation of lamellae in the film. If lamellae orient parallel to the film surface (perpendicular to gas flow direction), a gas molecule has to pass through both high and low permeability blocks. In such a case, the gas transport properties of block copolymer are closer to that of low permeability block as it presents the defining resistance (analogous to resistances in series in an electrical circuit).[53-56] If lamellae arrange perpendicular to the film surface, the overall gas transport behavior of the block copolymer is very close to that of high permeability block as it provides an easy bypass to the gas molecules(analogous to resistances in parallel in an electrical circuit).

The permeability values for SDS block copolymer sample reported in Table 2.2 lie in between the literature permeability values[57] of pure PS and PDMS polymers,

suggesting a random orientation of lamellae with a mixture of parallel and perpendicular oriented domains. This is typical of solvent casted films which often lack long range ordering of microstructure.

2.3 Summary

Diblock and symmetric triblock copolymers of polystyrene and polydimethylsiloxane with lamellar microstructure were made successfully using anionic polymerization. High molecular weight triblock copolymer (M_n ~140000 g/mol) was found to be tough enough to make free standing films, for which the gas transport properties could be tested. The gas permeability of the triblock copolymer was at least an order of magnitude higher than commercially available gas separation polymer. A combination of this triblock copolymer with appropriate layered zeolite can provide a mixed matrix membrane with high permeability and high selectivity.

3. Catalytic Hydrogenation of Poly(styrene-b-dimethylsiloxane-b-styrene) and the Thermodynamic Properties of the Resulting Material

Hydrogenation of polystyrene (PS) to polycyclohexylethylene (PCHE) is a commercially attractive process as it improves the thermal and oxidative stability of the material, as well as its upper use temperature. However, PCHE is very brittle and often needs to be block copolymerized with semi-crystalline and/or rubbery blocks to improve its toughness.

In this chapter, block copolymers containing PCHE and polydimethylsiloxane (PDMS) blocks will be discussed. This work was undertaken to examine the feasibility of hydrogenating the PS-PDMS block copolymers. The PS-PDMS-PS triblock copolymers described in Chapter-2 were hydrogenated using a commercial catalyst to obtain the PCHE-PDMS-PCHE triblock copolymers and the mixing properties of PCHE with PDMS were established.

The chapter begins with an introduction to polyolefins and their mixing thermodynamics. Next, a detailed experimental study describing the hydrogenation of the PS-PDMS-PS triblock copolymers and characterization of the resulting materials is presented. Finally, the Flory-Huggins interaction parameter between the PCHE and PDMS blocks is assessed in the context of current published approaches to treating the thermodynamics of nonpolar block copolymers.

3.1 Introduction

Polyolefins are commercially important polymers that constitute a major share of the plastics industry.[58] With the development of polycyclohexylethylene (PCHE)[59], obtained by the hydrogenation of polystyrene, a new material was added to the existing library of these polymers. PCHE brings a plethora of interesting properties such as high modulus, high application temperature and excellent optical properties.[58,60] A successful method for hydrogenating polystyrene (PS) without degradation, was demonstrated by Gehlsen and Bates more than a decade ago.[59] However, application of that approach requires large amounts of catalyst, making this process uneconomical. At about the same time, Hucul and Hahn[60] developed a significantly more efficient hydrogenation catalyst by depositing platinum and other transition metals (e.g. rhenium) within a macroporous (ca. 300 nm pore diameter) silica substrate. This new catalyst permits nearly complete hydrogenation (>99%) of polystyrene without chain degradation, at overall loadings (metal and support) of about 0.07 g of the catalyst per gram of the polymer. Moreover, this catalyst can be regenerated for repeated use, making polystyrene hydrogenation a commercially viable process. However, PCHE homopolymer is a very brittle material, which further stalled its commercialization. Over the last ten years, various studies have shown that this key limitation can be overcome through block copolymerization of PCHE with rubbery or semicrystalline polymers, including poly(ethylene), poly(ethylenepropylene), poly(ethylethylene) and combinations of these saturated hydrocarbons.[31,35,61,62] This chapter describes the synthesis and preliminary characterization of a new class of PCHE based block copolymers, obtained by catalytically hydrogenating PS-PDMS-PS triblock copolymers. Remarkably, this saturation reaction results in almost no chain degradation, thus permitting us to evaluate the morphology, and mixing thermodynamics of this pair of non-polar polymers.

The thermodynamics of polymer-polymer mixing dictate the morphology of homopolymer blends and the microstructure of block copolymers. Anticipating the mixing behavior of two macromolecules, particularly polyolefins, persists as a theoretical challenge. Polyolefinic block copolymers represent weakly interacting systems and so

other factors like system compressibility, free volume effects and excess entropic contributions can have a decisive influence over the phase behavior of these materials. Over the past few years, a host of experimental and theoretical studies[22,24,28,59,63-78] have enhanced the general understanding of polymer mixing thermodynamics. But, new perplexing phenomena have been reported in last decade or so, which show that phase behavior of block copolymers is far richer than previously thought. Influence of pressure on the phase boundaries have been reported in some of the polyolefins system.[79-82] Interestingly, depending on the particular polyolefin system and operating pressure, the mixing of polymers can be enhanced or reduced by applying pressure. Disorder (mixed state) to order (phase separated) transition (LDOT) upon heating have been reported in some of the weakly interacting block copolymer systems.[83-85] Very recently, close loop behavior has been observed for the weakly interacting system of poly(styrene-pentylmethacrylate) diblock copolymer[86-88], which exhibits both lower disorder-to-order transition (LDOT) at low temperature and upper order-to-disorder transition (UDOT) at high temperature. This behavior is thought to arise from a delicate balance between enthalpic interactions and contributions from free volume effects and directional entropy. Furthermore, this effect might be important in other weakly interacting polymer systems like polyolefins and a carefully chosen system together with experimental tools of varying pressure and selective solvents can bring these transitions in experimentally accessible temperature range. These findings adequately show that our understanding of block copolymer phase behavior is far from complete. It would require quantitative data from a wider range of polymer systems together with advanced theories which can incorporate various entropic and enthalpic factors, in order to establish a unified approach for predicting the phase behavior of polymer mixtures.

The Bates group has studied the mixing behavior of various combinations of saturated hydrocarbon polymers for nearly two decades. PCHE based block copolymers are especially attractive, both from the perspective of industrial application as mechanically stiff yet tough materials,[31,61,89] and as model substrates for exploring basic polymer blend thermodynamics.[66,76,77,90] In this chapter, a block copolymer composed of

PCHE and PDMS blocks has been reported. PDMS has many interesting properties, such as low surface tension, low glass transition temperature and biocompatibility. Adding PCHE can impart stiffness and thermal stability, thereby producing a more robust material with a potentially wider range of applications. A method has been demonstrated to produce PCHE-PDMS-PCHE triblock copolymers by the catalytic hydrogenation of PS-PDMS-PS precursor block copolymers using a Pt/Re-SiO_2 catalyst provided by the Dow Chemical Company. Figure 3.1 illustrates the hydrogenation reaction. The thermodynamic properties of the saturated block copolymers were also investigated using dynamic mechanical spectroscopy (DMS) and small angle x-ray scattering (SAXS) techniques. In addition, the mixing thermodynamics of PCHE and PDMS in the context of solubility parameters and the concept of conformational asymmetry has also been discussed. To the best of our knowledge, this is the first report of the successful preparation of block copolymers containing PCHE and PDMS.

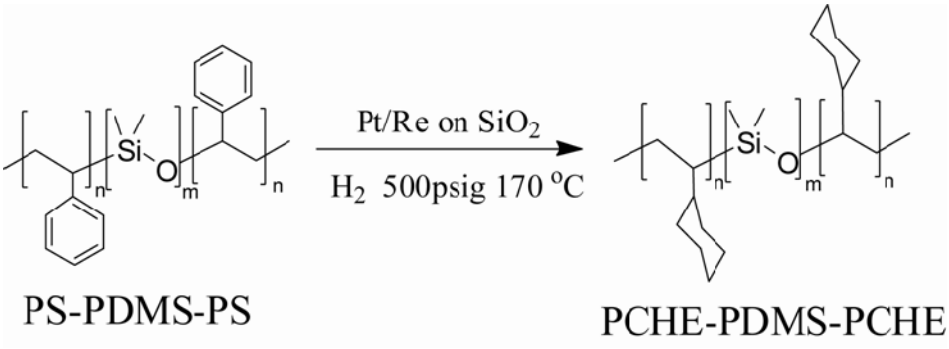

Figure 3.1. Reaction schematic of hydrogenation of PS-PDMS-PS triblock copolymer to make PCHE-PDMS-PCHE triblock copolymer.

3.2 Experimental Section

PS-PDMS-PS Synthesis

PS-PDMS-PS triblock copolymers, precursors to PCHE-PDMS-PCHE triblock copolymers, were synthesized by sequential anionic polymerization of styrene and hexamethylcyclotrisiloxane (D_3) monomers, followed by chain coupling with dichlorodimethylsilane.

Styrene monomer (Aldrich) was degassed by three freeze-pump-thaw cycles followed by twice stirring with dibutylmagnesium (1 hr each) before finally distilling into a flamed burette. D_3 monomer (Aldrich) was degassed in a similar fashion followed by stirring over calcium hydride (4 hrs) and dibutylmagnesium (1 hr), and final distillation into a flamed burette.[41] D_3 monomer was held at 90 °C in a liquid state during these operations using a silicon oil bath. Cyclohexane was purified by sequential passage through columns of activated alumina and Q5 catalyst (Engelhard). Tetrahydrofuran (THF) was purified by passing through two activated alumina columns.[42] Solvents were collected into sealed flasks under anhydrous conditions using Schlenk techniques.

Anionic polymerization of the PS-PDMS-PS triblock copolymers was conducted under an argon atmosphere in a Pyrex reactor fitted with Teflon ferrules and screw caps. A more detailed description of the experimental setup was presented in a previous report.[91] Styrene was initiated in cyclohexane at 40 °C using sec-butyllithium; the presence of polystyryl anions was indicated by a deep orange color. Polymerization proceeded for six hours, after which a small aliquot was extracted from the reactor for later analysis. Subsequently, D_3 monomer was added to the reactor, and the contents were stirred for 12 hrs at 25 °C. Prior work suggests complete crossover to siloxyl anions under these conditions.[41] However, polymerization of D_3 is very slow in nonpolar solvents such as cyclohexane, and, therefore, sufficient THF was added to make a 50:50 mixture with the cyclohexane. The solution became colorless immediately after the addition of THF, indicating the onset of D_3 polymerization. This cyclic monomer was polymerized for 1.5 hours (~ 33% conversion), and the growing polymer chains were coupled by adding a stoichiometric amount of dichlorodimethylsilane. D_3 monomer was not polymerized to high conversions to prevent side reactions and oligomer formation, which become competitive with the polymerization at higher conversions. The polymers were recovered by solvent evaporation, re-dissolution in THF, and precipitation into a 50/50 mixture of methanol/isopropanol before finally drying to constant mass at 80 °C under vacuum (~ 10^{-1} torr). Polystyrene homopolymer (c.a. 3% of the total mass) was detected in all the triblock copolymers due to some termination of the first block. This

was removed by titrating a 2% polymer solution in dioxane with a 50:50 mixture of methanol/water at room temperature until it turned cloudy.[43,45] The block copolymer formed a floating mass, while the homopolymer remained dissolved in the solution.

Catalytic Hydrogenation

PCHE-PDMS-PCHE triblock copolymers were prepared by catalytic hydrogenation of the PS blocks in PS-PDMS-PS triblock copolymers. These reactions were conducted in a stainless steel pressure vessel described elsewhere.[92] The polymer solution (5g polymer in 500 ml cyclohexane) and the catalyst (1g) were poured into the reaction vessel, which was then sealed and purged three times with nitrogen. Reactor contents were subsequently pressurized to 500 psi with hydrogen gas and heated to 170 °C with intense stirring. The reaction was carried out for 5h, after which heating and stirring were stopped and the reactor contents were cooled to room temperature. The catalyst was removed by filtering the polymer solution through a 0.22 micron Durapore® membrane filter (Millipore), and the polymer was recovered by solvent evaporation and drying to constant mass at 80 °C under vacuum (10^{-1} torr).

Characterization

The compositions and the extent of hydrogenation of the block copolymers were determined from ^{1}H NMR spectra collected with a 300 MHz Varian instrument using deuterated chloroform as the solvent. PS and PCHE volume fractions were calculated using the reported homopolymer densities at 140 °C (Table 3.1).[46]

Number average molecular weights (M_n) of all specimens were calculated using the M_n value for the PS block of precursor material (extracted during the synthesis), measured using a PS-calibrated SEC trace. Combining the composition (NMR) and M_n for PS block yielded the overall M_n. SEC was also used to determine the polydispersity of the block copolymers before and after the hydrogenation to establish whether the hydrogenation process led to any broadening of the molecular weight distribution.

Table 3.1. Notations and chemical structure for various blocks

Polymer	Chemical Structure	ρ^a (g/cm^3)	b (Å)^b
PCHE		0.92	4.60
PE	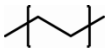	0.78	8.35
PEE	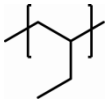	0.81	5.39
PEP	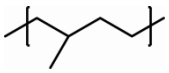	0.79	6.84
PDMS	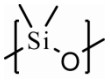	0.89	5.39

[a]Mass density at 140 °C.[46] [b]Statistical segment length with respect to 118 Å^3 reference volume of repeat unit.[46]

SAXS experiments were carried out to characterize the morphology and the order-disorder transition temperature (T_{ODT}'s) of the saturated block copolymers. Experiments were conducted on a home built system[47] using Cu Kα radiation and a Siemens area detector located at a distance of 230 cm from the sample. The morphology was deduced from the ratio of primary peak position to higher order peak positions and the T_{ODT} was identified by the onset of primary peak broadening and a sharp decrease in the intensity of the SAXS pattern. For characterization of morphology, samples were shear aligned[48] using a reciprocating shear device[49] and then exposed to x-rays for 30 min at 25 °C while recording the scattering patterns. Measurements for T_{ODT} identification were performed by systematically heating the samples in small steps of temperature, and holding the sample at each temperature for 8 min before exposing it to the x-ray beam for another 8 min.

TEM was employed for direct visualization of the morphology of the block copolymers using a JEOL 1210 microscope operated at an accelerating voltage of 120 kV. Shear aligned samples were cryo-microtomed to obtain 50-80 nm thick slices using a diamond knife operated between -130 to -145 °C on a Reichert Ultracut S Ultramicrotome.[47] No staining was necessary, as the silicon in the PDMS block provides adequate contrast for imaging.[43]

DMS provided an independent measure of the T_{ODT}'s. Measurements were conducted on a Rheometrics Scientific ARES strain-controlled rheometer fitted with 25mm parallel plates. All samples were compression molded into 25mm × 1mm disks by holding them at 1000 psi and 150 °C for 10 minutes. Sample temperature in the rheometer was controlled (±1 °C) with a thermally regulated nitrogen gas purge. Elastic (G') and loss (G") moduli were recorded at a constant frequency over a selected range of temperatures while heating or cooling the samples. Disordering (ordering) of the block copolymer materials was identified by a discontinuous decrease (increase) in G' and G".[93]

3.3 Results and Analysis

Molecular Charcaterization

Three PS-PDMS-PS triblock copolymers containing 41 to 45% by volume of polystyrene were prepared and hydrogenated to produce PCHE-PDMS-PCHE triblock copolymers. The samples were designed specifically to have accessible ODT temperatures. The molecular characterization data for all three polymers appears in Table 3.2.

Table 3.2. Polymer Characterization Results

Sample	$10^3 M_n$[a] (g/mol)	f[b]	PDI[c]	N[d]	T_{ODT} (°C)[e]
CDC-4	15.2	0.41	1.09	235	103
CDC-5	17.1	0.45	1.07	265	183
CDC-1	31.8	0.41	1.09	494	>250

[a]As calculated from mass fraction and M_n of precursor PS block. [b]Volume fraction of PCHE calculated from NMR and densities reported in Table 3.1. [c]From SEC based on polystyrene standards. [d]Degree of polymerization based on reference volume of 118 Å^3. [e]As determined by the discontinuity in elastic modulus during isochronal temperature ramp.

Representative ^{1}H NMR spectra for the PCHE-PDMS-PCHE triblock copolymer (CDC-5), and the unsaturated precursor PS-PDMS-PS, are shown in Figure 3.2. Complete hydrogenation of polystyrene (>99%) is marked by the disappearance of specific resonances associated with the aromatic protons (6.2-7.2 ppm) in the ^{1}H NMR spectra of the saturated product (Figure 3.2(B)).

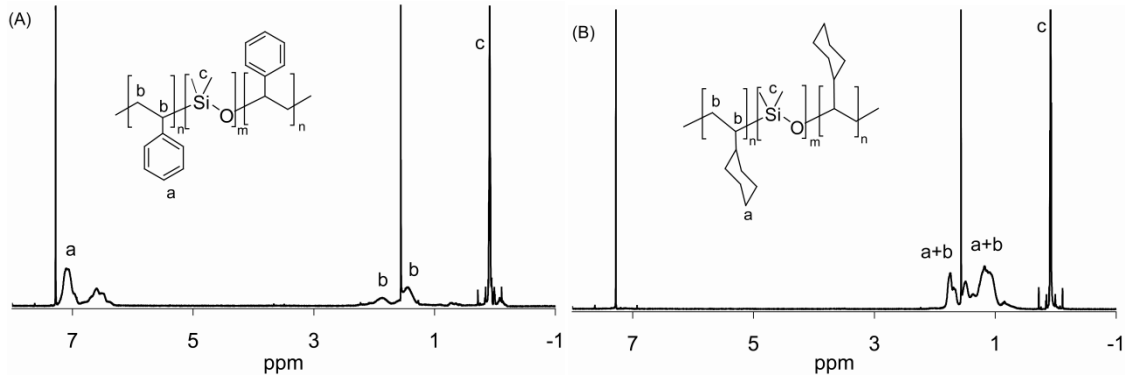

Figure 3.2. ^{1}H NMR spectra of (A) PS-PDMS-PS triblock copolymer and its hydrogenated form (B) PCHE-PDMS-PCHE triblock copolymer. The aromatic resonances (6-7.5ppm) of the PS-PDMS-PS triblock copolymer are converted into the cyclic resonances (1-2 ppm) after hydrogenation. The sharp peaks at 7.3 ppm and 1.5 ppm are due to residual chloroform and water in the solvent.

SEC traces are shown in Figure 3.3. Trace (b) for the PS-PDMS-PS triblock shows the presence of a small amount of polystyrene homopolymer impurity (around an elution time of 24 min), which was removed using the precipitation technique described in the previous section (trace c). Hydrogenation yielded the saturated PCHE-PDMS-PCHE triblock copolymer depicted by the trace (d). Saturation did not noticeably affect the polydispersity of this sample, although, a small amount (ca. 1%) of low molecular weight polymer is barely resolved in the SEC trace of the hydrogenated triblock (trace d, around an elution time of 24 min), perhaps indicating some (PDMS) chain degradation during the hydrogenation reaction. All saturated polymers contained a similar amount of this impurity, with a M_n value close to that of precursor PS block, presumably created by the spurious scission of PDMS. This minor level of degradation is unlikely to significantly impact the properties of the saturated triblock copolymers.

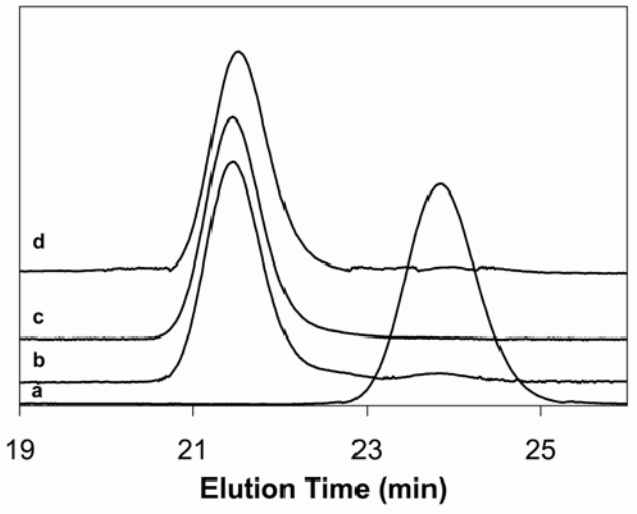

Figure 3.3. Size exclusion chromatograph of (a) Polystyrene aliquot, (b) PS-PDMS-PS triblock copolymer obtained after polymerization, c) PS-PDMS-PS triblock purified by precipitation using dioxane-methanol/water mixture to remove polystyrene homopolymer impurity and d) PCHE-PDMS-PCHE triblock obtained after catalytic hydrogenation. Curves have been shifted vertically for clarity.

Morphology

The morphology of the saturated polymers were characterized using SAXS and TEM. The 2-D SAXS data obtained at 25 °C were integrated azimuthally to yield the intensity (I) as a function of scattering wavevector $q = (4\pi / \lambda)\sin(\theta / 2)$, as shown in Figure 3.4. Two reflections are clearly evident in the data obtained from samples CDC-1 and CDC-5 at relative *q* values 1:2, indicating a lamellar morphology. For CDC-4, only one peak is evident. Also, a reduced overall scattering intensity was obtained with this lower molecular weight specimen. However, based on the similar block volume fractions in both CDC-4 and CDC-1, a lamellar morphology is expected for the former material. Morphologies for all three samples were further confirmed to be lamellar by direct visualization of the cryo-microtomed polymer slices by TEM. Figure 3.5 shows a TEM image of the CDC-5 sample as an example.

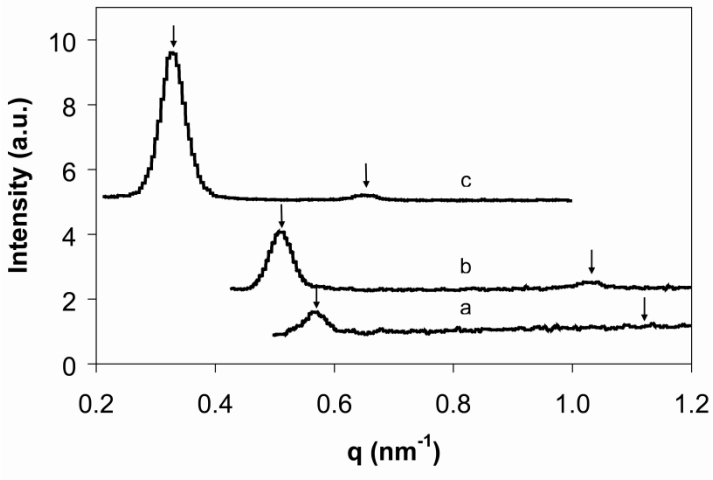

Figure 3.4. 1-D SAXS profiles obtained from shear aligned samples at 25 °C: (a) CDC-4, (b) CDC-5 and (c) CDC-1. The vertical arrows denote peak locations expected for a lamellar microstructure. Curves have been shifted vertically for clarity.

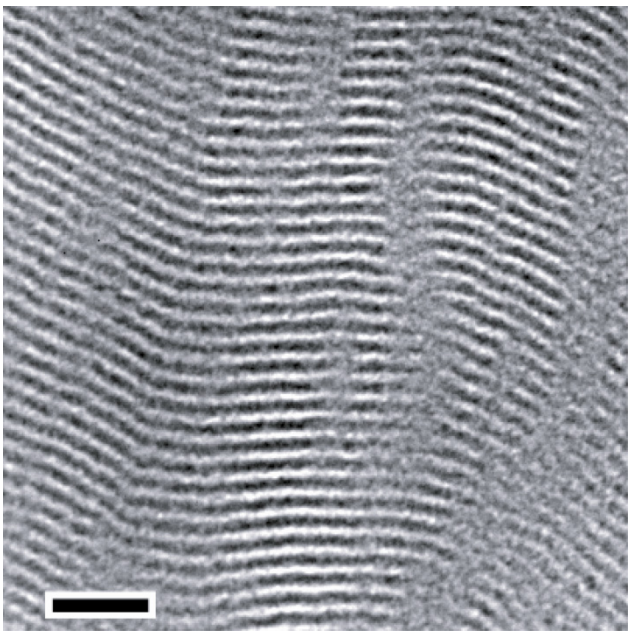

Figure 3.5. TEM image of CDC-5 indicating a lamellar morphology of the block copolymer. The lamellar domains were aligned by applying reciprocating shear, followed by cryo-microtomy to obtain thin slices of polymer for imaging. Dark and light regions correspond to PDMS and PCHE domains. The scale bar represents 50 nm.

Order Disorder Transition

T_{ODT} values were determined for the saturated polymers by SAXS as described earlier. Figure 3.6 shows 1-D SAXS profiles for the three samples at various temperatures. A sharp decrease in the scattering intensity is visible around a temperature of 103 °C for CDC-4 (Figure 3.6(a)) and 181 °C for CDC-5 (Figure 3.6(b)), indicating the ODT. CDC-1 remained ordered up to 200 °C (Figure 3.6(c)), which was the highest temperature accessible on SAXS instrument. All samples were subjected to repeated cycles of increasing and decreasing temperature to check the reproducibility of the scattering profiles. For CDC-4 and CDC-5 samples, we reproducibly obtained the ordered and disordered phases as we crossed the T_{ODT} from either side.

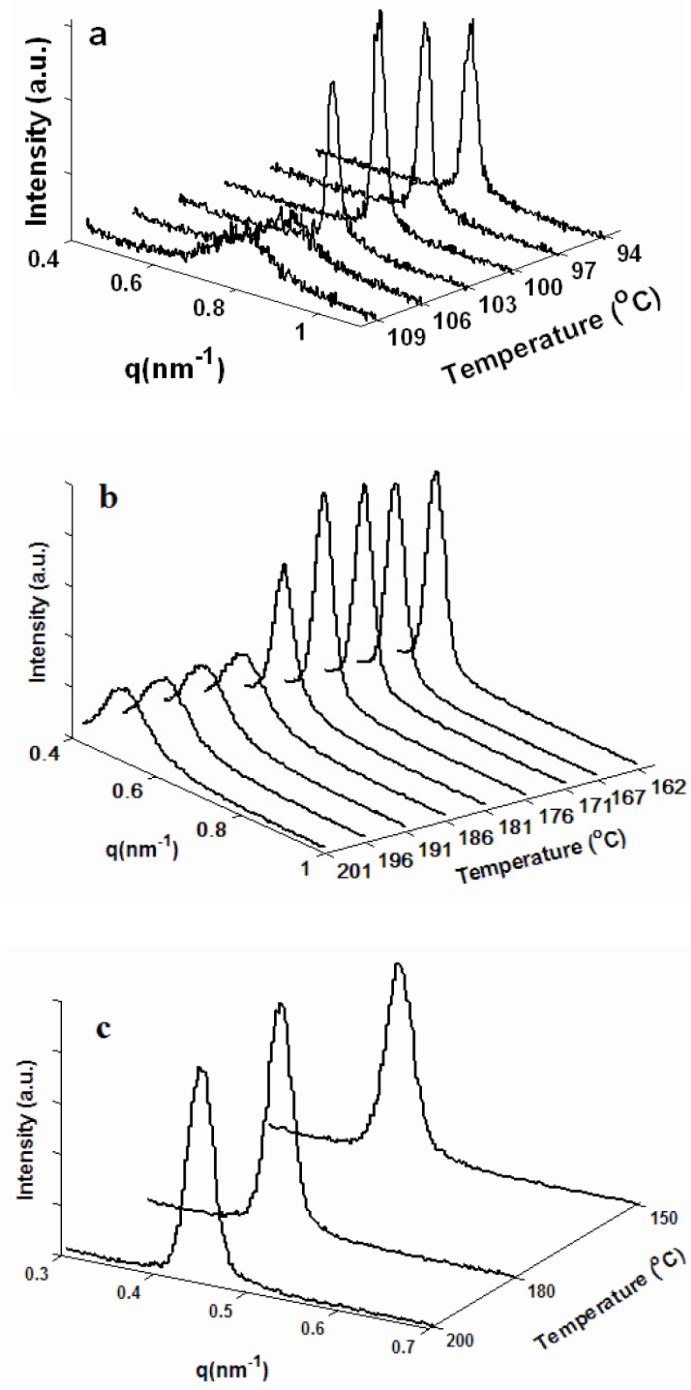

Figure 3.6. 1-D SAXS profiles at various temperatures for: a) CDC-4, b) CDC-5, c) CDC-1. A sharp decrease in the scattering intensity and broadening of peak marks the onset of ODT.

ODT temperatures were independently determined by DMS. CDC-1 was tested at a frequency of 1 rad/s between 100 and 250 °C with a heating/cooling rate of 1 °C/min. CDC-4 was tested at 0.1 rad/s between 95 and 114 °C with a heating/cooling rate of 0.2 °C/min, and CDC-5 was tested at 1 rad/s between 150 and 200 °C with a heating/cooling rate of 2 °C/min. A strain amplitude of 1% was employed for all three samples. Samples were subjected to multiple heating and cooling cycles to check the reproducibility of the ODT temperatures. Figure 3.7 shows the elastic modulus (G') vs. temperature for CDC-4 and CDC-5 during heating and the cooling cycles. ODTs are identified by the precipitous drop in elastic moduli (G') during the heating cycle.[93] Using this technique, T_{ODT} was established to be 103±1 °C for CDC-4 and 183±1 °C for CDC-5 as indicated in Figure 3.7. These values were obtained reproducibly and are within experimental uncertainty of those obtained by the SAXS experiments. CDC-1 did not show any discontinuous decrease in G' up to a temperature of 250 °C (data not shown), indicating an ordered microstructure. Higher temperatures (>250 °C) were not explored in order to avoid degradation of the polymer.

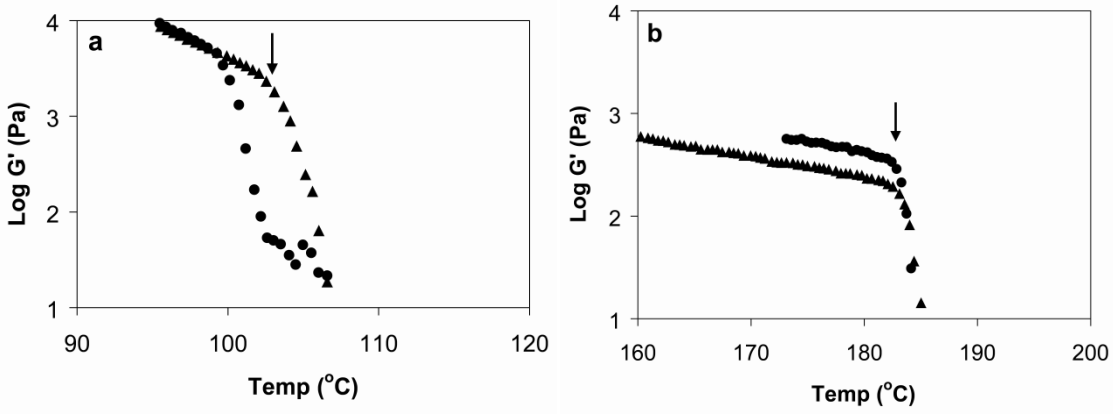

Figure 3.7. Dynamic elastic modulus (G') during the heating (▲) and cooling (●) cycles of an isochronal temperature test for a) CDC-4, b) CDC-5. For CDC-4, the heating/cooling rate was 0.2 °C/min, and the frequency was 0.1 rad/s. For CDC-5, the heating/cooling rate was 2 °C/min and the frequency was 1 rad/s. The ODT is marked by a sharp decrease in G', as indicated by the arrows in the figures.

3.4 Thermodynamic Behavior

Polymer-polymer phase behavior can be deceptively complex. Local (segment scale) interactions are governed by both enthalpic and entropic factors. Polyolefins present a particularly challenging set of materials since the enthalpic driving force for demixing is quite weak, thus amplifying non ideal contributions to the overall mixing free energy. A widely accepted approach to treating polymer mixtures is to employ a mean field theory, in which the phase behavior of block copolymers is assumed to be governed by a simple binary segment-segment interaction parameter, captured by the Flory-Huggins interaction parameter χ, which is often written in the form:

$$\chi = \frac{A}{T} + B \qquad (3.1)$$

Eq 3.1 lumps the enthalpy of mixing and various excess free energy contributions into the parameter A and B, respectively.[90] Sometimes, A and B in Eq 3.1 are assumed to be composition or molecular weight dependent in order to accommodate specific interactions like hydrogen bonding and various equation-of-state effects such as volume changes on mixing, thermal expansion differences, and component compressibilities.[94,95] However, in this report we focus on determining χ(T) by considering a single composition and pressure, and neglecting other dependencies.

To this end, χ(T) can be extracted experimentally from a set of block copolymers by applying mean field theory, either with or without a fluctuation correction.[24] For diblock copolymers, Maurer et al.[68] have shown that combining the mean field result[22] $(\chi N)_{ODT} = 10.5$ for $f = 0.5$ with the ODT measurements, gives the closest approximation to the χ(T) expression obtained from homopolymer blends. (Here N is the overall degree of polymerization and f is the volume fraction of the first block). Matsen et al.[28] and Mayes et al.[67] have extended mean field theory calculations from diblock copolymers to symmetric ABA triblock copolymers, yielding,

$$\chi(T_{ODT}) = 19/N \quad (\text{for } f=0.45) \qquad (3.2a)$$

and $\chi(T_{ODT}) = 20/N$ (for f=0.41) (3.2b)

where, f is the total volume fraction of block A and N is the overall degree of polymerization normalized to a chosen reference volume. For our analysis, we have chosen a reference volume of 71.1 cm^3/mol (118 $Å^3$ per repeat unit), which is approximately the molar volume of most four-carbon polyolefin segments. This choice of reference volume is consistent with previous reports[76,90] and facilitates comparison of χ parameters between different pairs of polyolefins. Parameters A and B are obtained by least square fit to the χ vs. T data obtained for samples with different values of N. It should be noted that fluctuation effects are not accounted for in this approach, so there may be a slight error in the χ values report here; nevertheless, the qualitative features of this analysis should still be useful.

Based on T_{ODT} and N (Table 3.2) for samples CDC-4 and CDC-5, the expression for χ(T) between PCHE and PDMS was determined to be:

$$\chi = \frac{28.1}{T} + 1.0\times10^{-2} \qquad (3.3)$$

Here, it should be noted that the A and B values extracted from χ vs. T data are sensitive to uncertainties in molecular weights of the samples. An error of about ±5% in molecular weight (associated with uncertainties in SEC and NMR measurements) can change the above expression from $\chi = 37.8/T - 1.1\times10^{-2}$ to $\chi = 19.8/T + 31.9\times10^{-2}$, although the overall χ values are still within a range of ±5%. Thus, it is safer to draw quantitative conclusions regarding the magnitude of the χ values.

For saturated hydrocarbons, χ is often estimated using the difference in solubility parameters based on the Hildebrand equation[96],

$$\chi_{AB} = \frac{v}{k_B T}(\delta_A - \delta_B)^2 \qquad (3.4)$$

where v is the reference volume (118 $Å^3$) and δ_A and δ_B represent the pure component solubility parameters for the constituent polymers. This approach neglects the excess free

energy terms (accounted for by the parameter B in Eq 3.1) and considers only the dispersive interactions. Polyolefins are often assumed to be the most likely candidates to conform to Eq 3.4, as they are governed primarily by dispersive van der Waals forces. Graessley and co-workers[63,70,71,97-99] have correlated the experimentally measured χ values for numerous polyolefins with a self-consistent set of δ_i's for 75% of the blends studied. Cochran and Bates[76] extended this approach to diblock copolymers containing PCHE and other polyolefins and were able to rationalize the χ values with a self consistent set of δ_i's. Almdal et al.[90] have applied this approach to block copolymers containing various polyolefins with PDMS and also were able to correlate the χ values with a set of self-consistent δ_i's. This work adds PCHE-PDMS to this matrix of data. All relevant parameters are listed in Table 3.3. χ values for all polymer pairs are compared at 456 K. This temperature was chosen on the basis of experimentally obtained T_{ODT} for sample CDC-5. A different choice of the temperature, however, does not affect our general conclusions.

3.5 Discussion

Various approaches have been utilized in the past to rationalize the thermodynamic behavior of polyolefin block copolymers and blends of polyolefin homopolymers. As mentioned in the previous section, self consistent set of solubility parameters explains the phase behavior of a host of polymer blends, but fails for about 25% of the blends investigated by Graessley and co-workers.[63,70,71,97-99] Another approach based on segment length mismatch, suggested by Bates et al.[77], provides a rationale for the observed phase behavior in many polymer systems but fails to make the quantitative predictions. Some more sophisticated theories have been put forward by several workers, which incorporate factors such as polymer compressibility[65,73,100,101], conformational asymmetry[74,75,78,102] and segment architecture[73,103-106], that were not accounted by traditional Flory-Huggins theory. Fredrickson and coworkers[78,102] have suggested an excess entropy contribution to free energy arising from the structural asymmetry of polymer chains. Dudowicz and Freed[73,103] have developed a lattice cluster theory for compressible diblock copolymers, which considers polymer segment architectures in

great detail. Schweizer and co-workers[65,74,75] have developed an off-lattice method that relies on the polymer reference interactive site model (PRISM), which addresses local and non-local aspects of polymer-polymer mixing. These theories attempt to address the thermodynamic behavior of actual polymer blends and block copolymer systems. Figure 3.8 plots the χ(T) data extracted from the PCHE-PDMS-PCHE triblock copolymer (Eq 3.3) along with other olefinic block copolymers reported in previous publications.[66,76,90,93] *A* and *B* parameters and estimated solubility parameter differences $|\Delta\delta|$ are listed in Table 3.3.

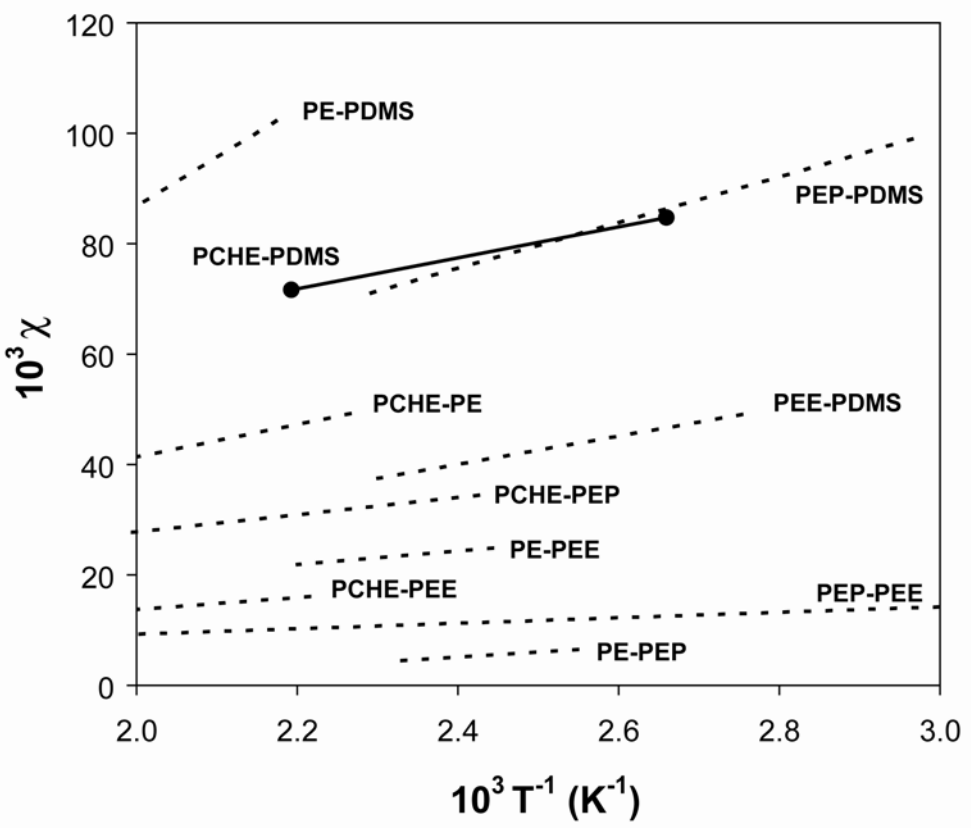

Figure 3.8. Temperature dependence of χ_{AB} (T_{ODT}) for various olefinic block copolymers. Data points (●) correspond to PCHE-PDMS-PCHE triblock copolymers characterized in Table 3.2, and solid line is to evaluate parameters *A* and *B* of Eq 3.1. Dashed lines are correlations for various block copolymers taken from previously published data.[66,76,90]

Table 3.3. Fitted Parameters in $\chi = A/T + B$ and solubility parameter differences $|\Delta\delta|$ calculated from Eq 3.4

polymer pair	A(K)	$B\times10^3$	$\chi\times10^3$ (456 K)	$\lvert\Delta\delta\rvert$ $(MPa)^{1/2}$	Ref.
PE-PDMS	90.7	-94.6	104	2.36	[90]
PEP-PDMS	41.4	-23.7	67.1	1.89	[90]
PEE-PDMS	25.4	-20.9	34.8	1.36	[90]
PCHE-PE	29.4	-17.4	47.1	1.58	[76]
PCHE-PEE	11.2	-8.70	15.9	0.92	[76]
PCHE-PEP	15.7	-3.60	30.8	1.28	[76]
PE-PEP	8.87	-16.0	3.47	0.43	[90]
PEP-PEE	3.66	1.37	9.40	0.71	[90]
PE-PEE	12.1	-4.90	21.6	1.07	[90]
PCHE-PDMS	28.1	10.0	71.6	1.95	this work

Graessley and coworkers have established the following order of solubility parameters based on deuterium labeling experiments[98,99]

$$\delta_{PEE} < \delta_{PEP} < \delta_{PE}$$ (see Table 3.1 for block notations)

Cochran and Bates[76] added PCHE to this sequence (see Table 3.3). Self consistency of the solubility parameters suggests the following order:

$$\delta_{PCHE} < \delta_{PEE} < \delta_{PEP} < \delta_{PE}$$

Almdal et al.[90] obtained the following order for various PDMS-polyolefin block copolymer:

$$\Delta\delta_{PEE-PDMS} < \Delta\delta_{PEP-PDMS} < \Delta\delta_{PE-PDMS}$$

Self-consistency amongst these three sets of results necessitates the following order:

$$\delta_{PDMS} < \delta_{PCHE} < \delta_{PEE} < \delta_{PEP} < \delta_{PE}$$

In terms of the solubility parameter differences, this implies that $\Delta\delta_{PCHE-PDMS}$ should be smaller than $\Delta\delta_{PEP-PDMS}$ and $\Delta\delta_{PEE-PDMS}$. However, the solubility parameter difference calculated from the ODT data for PCHE-PDMS-PCHE triblock copolymer, listed in Table 3.3, leads to $\Delta\delta_{PCHE-PDMS} \approx \Delta\delta_{PEP-PDMS}$ and $\Delta\delta_{PCHE-PDMS} > \Delta\delta_{PEE-PDMS}$. Thus, PCHE-PDMS challenges the self consistency between the solubility parameters reported previously.

Bates et al.[77] have suggested an alternative approach to explain the experimentally determined χ values in polyolefin block copolymers. They argue that the differences in statistical segment lengths of the constituent blocks in polyolefin block copolymers are strongly correlated with the measured χ values. Holding all other factors constant, χ is expected to increase with increasing mismatch of the statistical segment lengths of the constituent blocks. This change in χ is attributed to entropic penalties associated with the conformational adjustments required to mix chains of different statistical segment lengths. This effect becomes particularly important with polyolefin mixtures, since the enthalpy of mixing is relatively small. In principle, the effects of excess entropy can play a dominant role in determining the phase behavior of these systems. Scaling of the χ parameter with segment length mismatch has been noted for PDMS containing polyolefin block copolymers[90] and many other polymer systems[71,72], and theoretical explanations have also been provided for the same.[78,102]

Table 3.4 lists the χ parameter values for various PDMS containing polyolefin block copolymers studied previously and in this work. Segment length mismatch is defined by the ratio $\Delta b/\bar{b}$, as suggested by Bates et al.[77]:

$$\frac{\Delta b}{\bar{b}} = \frac{b_A - b_B}{f b_A + (1-f) b_B} \qquad (3.5)$$

where b represents statistical segment length and f is the volume fraction of block A. Segment length mismatch argument anticipates a higher χ value for PEP-PDMS than for PCHE-PDMS, which is inconsistent with the experimental results of this work (compare $\Delta b/\bar{b}$ and χ values in Table 3.4).

Table 3.4. Various parameters for PDMS containing polyolefin block copolymers

polymer pair	$\Delta b/\bar{b}$ [a]	$\sum\beta^2$ [b] ($Å^{-1}$)	ε [c]	$\left[\frac{1-\varepsilon}{f+(1-f)\varepsilon}\right]^2$ [d]	γ [e]	$\chi \times 10^3$ (at 456 K)	$\chi_\varepsilon \times 10^3$ [f]	Λ_b^{-1} [g] (Å)
PEE-PDMS	≈0	0.082	1.00	≈0	1.00	34.8	0	-
PCHE-PDMS	0.16	0.071	0.73	0.10	0.85	71.6	36.8	1.10
PEP-PDMS	0.24	0.107	1.61	0.22	1.27	67.1	32.3	1.50
PE-PDMS	0.43	0.140	2.40	0.68	1.55	104	69.2	1.69

[a]Segment length mismatch parameter defined in Eq 3.5.[77] [b]z-effect parameter defined in Eq 3.6.[90] [c]Conformational asymmetry parameter calculated from Eq 3.9[78] using statistical segment lengths listed in Table 3.1. [d]Asymmetry factor in Eq 3.8. [e]Asymmetry parameter in PRISM theory as defined in Eq 3.10[74,75] [f]Excess entropy contributions to χ parameter assuming a zero excess contribution for PEE-PDMS[78,102] calculated by assuming zero excess entropy contribution for PEE-PDMS pair. [g]Cutoff length that separates local and non local conformational regimes (Eq 3.8).[78,102]

A third argument to explain the experimentally observed χ parameter values, given by Almdal et al.[90], is based on the so called 'z effect' which is associated with the parameter $\sum\beta^2$:

$$\sum \beta^2 = \beta_A^2 + \beta_B^2 \qquad (3.6)$$

with,

$$\beta^2 = \frac{b^2}{6v} \qquad (3.7)$$

where v is the reference volume (118 Å^3). The authors suggested that polymers with larger β^2 value offer more contacts with neighboring chains leading to a higher effective chain-chain coordination number, z, than those with smaller β^2 values. Higher z, in turn, enhances the total enthalpic contribution to the χ parameter. Based on the values of the parameter $\sum\beta^2$ for polyolefin-PDMS block copolymers (listed in Table 3.4), the z effect argument anticipates that both $\chi_{PEP-PDMS}$ and $\chi_{PEE-PDMS}$ will be greater than $\chi_{PCHE-PDMS}$, while experimental results obtained in this work indicate that $\chi_{PEP-PDMS} \approx \chi_{PCHE-PDMS}$ and $\chi_{PEE-PDMS}$ is about half the value of $\chi_{PCHE-PDMS}$.

The above three factors (solubility parameter, excess entropy and excess enthalpy) can add up or cancel the effect of each other and it will be the net effect of these factors taken together, that will decide the ordering of χ parameter. However, even all three factors taken together, cannot explain PEP-PDMS and PCHE-PDMS having approximately equal χ values ($\chi_{PEP-PDMS} \approx \chi_{PCHE-PDMS}$). This suggests the limited applicability of these simplistic approaches for polyolefin–PDMS block copolymers and a more comprehensive theory is needed to explain the observed ordering of χ parameters.

Fredrickson et al.[78,102] have developed a theory for athermal, conformationally asymmetric, polymer alloys using incompressible field theoretic methods. They argued that the lack of conformational symmetry in athermal block copolymers and polymer blends produces excess entropy of mixing which results in an additional contribution to the χ parameter. This excess contribution χ_ε to overall effective χ parameter is given by the equation:

$$\chi_\varepsilon = \frac{\Lambda_b^3 v}{24\pi^2}\left[\frac{1-\varepsilon}{f+(1-f)\varepsilon}\right]^2 \qquad (3.8)$$

where $\Lambda_b^{-1} > b$ is some cutoff length that separates the local and non local conformational regimes and ε is the conformational asymmetry parameter given by:

$$\varepsilon = \frac{\beta_A^2}{\beta_B^2} \qquad (3.9)$$

Block copolymers of PDMS with various polyolefins cannot be treated as strictly athermal since the enthalpic interactions between PDMS and polyolefin segments are likely to differ from PDMS-PDMS and polyolefin-polyolefin segment interactions. However, within the context of this theory, the enthalpic interactions should not vary from one polyolefin-PDMS block copolymer to another. Thus, it would be reasonable to expect that the differences in χ parameter values observed for various polyolefin-PDMS block copolymers are due to entropically based conformational asymmetry effects between the constituent blocks.

The form of Eq 3.8 requires the excess entropy contributions to vanish for conformationally matched polymers (ε = 1) and to be positive for conformationally mismatched pairs ($\varepsilon < 1$ or $\varepsilon > 1$). Thus, for PEE-PDMS pair, $\chi_\varepsilon = 0$, and χ_ε for the other pairs can be estimated by subtracting $\chi_{PEE-PDMS}$ from experimentally obtained χ values for other block copolymers. This procedure results in positive χ_ε values for the conformationally mismatched polymers listed in Table 3.4. Relatively good agreement with experimental data can be obtained by adjusting the cutoff length Λ_b^{-1} in Eq 3.8. Also, one would expect the cutoff length to increase from PCHE-PDMS to PE-PDMS based on increasing statistical segment length in this direction (and hence influence of local liquid structure on a larger scale). This is indeed the trend obtained (see Λ_b^{-1} values in Table 3.4). However, the values of the cutoff lengths obtained are unreasonably low (i.e. $\Lambda_b^{-1} <$ *b*), which represents a limitation of this theory and suggests that certain important factors

are not accounted for. Also it is somewhat unclear, how to assign a precise value to cutoff length once we know the constituent blocks, rather than treating it as a fitting parameter.

Dudowicz and Freed have constructed a comprehensive lattice cluster theory (LCT) for polymer blends[106] and block copolymers[73,103] which accounts for detailed variations in local chain structure. This theory has provided a rationale for understanding various extensions of Flory-Huggins theory (for e.g., presence of an entropic contribution to χ, concentration dependence of χ, equation of state effects, etc.). The authors have also addressed the issue of conformational asymmetry in some detail for polyolefin blends. However, the theory is very system specific and does not anticipate trends for block-copolymer thermodynamics. A comparison with the experimental data obtained in this work would require a detailed evaluation of this theory for polyolefin-PDMS block copolymers, incorporating finer details of monomer structure and interaction parameters, which is beyond the scope of this work.

A comprehensive theoretical approach to polymer blend thermodynamics based on polymer reference interactive site model (PRISM) has been developed by Schweizer and coworkers.[65,74,75,100,101] This approach accounts for local chain packing and polymer architecture, volume change upon mixing, thermally induced changes in chain dimensions and various other non Flory-Huggins effects which are neglected in the mean field approach. The main advantage of this theory lies in its off-lattice method which allows making general predictions on polymer thermodynamics by using a coarse grain description of polymer chains. Moreover, it has the capability to make precise quantitative predictions, based on more sophisticated models to describe polymer chains.

By using a coarse-grained model to describe polymer chains, the authors have made some general predictions regarding the influence of conformational asymmetry and local packing on the thermodynamic properties of block copolymers.[74,75] They argue that mixtures of polyolefins cannot be treated as athermal despite the fact that the real attractive interactions may nearly cancel in a mean sense. The microphase separation observed in these polymer mixtures arises from the local enthalpic interactions due to

conformational asymmetry induced packing differences, while the excess entropy contributions are very small in comparison and do not play a major role. This argument is in contrast with the incompressible field theoretical approach of Fredrickson et al.[78,102] discussed earlier, wherein a spatially nonlocal excess entropic contribution to the effective χ parameter was suggested to be responsible for the structure dependent phase stabilities, with energetic effects being treated as a small additive empirical correction.

David and Schweizer[74,75] have explicitly studied the effect of varying the conformational asymmetry in polyolefin diblock copolymers keeping one of the blocks the same, consistent with this work, where we have different polymers with varying conformational asymmetry and a common PDMS block. The authors report the apparent spinodal temperatures, $T_{s,app}$, as an indicator of the proximity to the true microphase separation transition occurring at T_{ODT}, for polymers with varying degree of chain stiffness. Conformational symmetry was defined by the parameter γ, which was simply the ratio of statistical segment lengths:

$$\gamma = \frac{b_B}{b_A} \qquad (3.10)$$

It should be pointed out here that actual values of various statistical segment lengths used by David and Schweizer[74] arise from the mapping of real branched polymers to unbranched effective homopolymer chains, which will be different than those described in this work based on a common reference volume (Table 3.1.). However, qualitative comparisons can still be made between their model predictions and the experimental data obtained in this work. The γ values for various polyolefin-PDMS block copolymers are listed in Table 3.4. The PRISM calculations predict that deviation from conformational symmetry (γ=1) results in increased value of $T_{s,app}$, which correlates with the increment in the χ parameter values in polyolefin-PDMS block copolymers upon increase in asymmetry. Also, the model predicts that block-copolymers with γ=0.85 and γ=1.25 will have approximately equal value of $T_{s,app}$. These γ values roughly correspond to PCHE-PDMS and PEP-PDMS, which indeed show approximately

equal χ values. Thus PRISM theory calculations with a coarse-grained polymer model for diblock copolymer melts, seems to capture the trend in χ parameter values obtained experimentally. A quantitative comparison will require mapping of polyolefin-PDMS block copolymer chain onto a suitable model and taking into account the energetic asymmetry between polyolefin-polyolefin, PDMS-PDMS and polyolefin-PDMS segments.

The results presented in this study indicate that the simplistic approaches based on the solubility parameter self consistency, conformational asymmetry and the z effect are not adequate to account for the mixing thermodynamics of PDMS with various polyolefins in the form of block copolymers. More sophisticated treatment such as the PRISM theory is more likely to capture the phase behavior of these polymers.

3.6 Summary

PS-PDMS-PS triblock copolymers were successfully hydrogenated to form PCHE-PDMS-PCHE triblock copolymers by heterogeneous catalytic hydrogenation. The hydrogenation process resulted in the complete saturation of PS blocks with negligible chain scission. Triblock copolymers with PCHE volume fractions ranging from 0.41-0.45 segregate into a lamellar morphology. The thermodynamic properties of this new material were established using small angle x-ray scattering and dynamical mechanical spectroscopy. PCHE and PDMS have strong segregation strength reflected by a rather high T_{ODT} of 180 °C for a relatively small PCHE-PDMS-PCHE triblock copolymer with M_n = 17000. In addition, the χ parameter value for the PCHE-PDMS polymer pair was found to be higher than PEE-PDMS and very close to that for PEP-PDMS, which cannot be rationalized by the solubility parameter approach or the simple arguments based on the conformational asymmetry. A more elaborate theoretical treatment, possibly PRISM theory based is needed to account for the non-ideal mixing of non-polar polymers.

4. Structural Preservation during Swelling, Pillaring and Exfoliation of zeolite precursor MCM-22(P)

As discussed in Chapter-1, nanometer-thick porous sheets derived from the exfoliation of layered zeolite materials have several advantages over isotropic zeolite crystals for mixed matrix membrane applications. Extremely small thickness (~1-2 nm) of these sheets can allow their integration into thin skins of hollow fiber membranes and high aspect ratio can provide separation enhancements even at very low overall loadings. Typically, layered materials are first swollen by intercalation of organic molecules to increase the spacing between the sheets and reduce the inter layer forces. The swollen material can be subsequently processed with polymer to make composite membranes, where polymer chains penetrate between the sheets and exfoliate them apart. In other cases, swollen crystal can be exfoliated by physical process such as ultrasonication to obtain individual sheets dispersed in a suitable solvent. However, such swelling and exfoliation processes often result in severe destruction of morphology and pore-structure of the zeolite sheets, often rendering them unsuitable for separation applications.

This chapter describes our efforts to swell and exfoliate a layered zeolite precursor, MCM-22(P). The pore structure of this material is appropriate for hydrogen separation. Previously reported swelling procedures for this material result in significant degradation of crystal morphology along with partial loss of crystallinity and dissolution of the crystalline phase. By carefully choosing the swelling conditions, such destruction was prevented in this work. A variety of characterization techniques like X-Ray

diffraction, electron microscopy and NMR confirmed the structural integrity of the swollen material. Motivated by the prefect swelling, a high surface area pillared material was also derived from the swollen crystals which could be useful for catalytic applications.

The chapter starts with an introduction to various layered materials which are potentially useful for separation applications, with a discussion on swelling and exfoliation of these materials. Next, a discussion on the morphology, pore structure and gas separation potential of zeolite MCM-22(P) has been provided. Finally, a detailed experimental study on swelling, pillaring and exfoliation of MCM-22(P) has been presented with special emphasis on its structural preservation, and results have been compared to previous swelling methods described in the literature.

4.1 Background

Layered materials are a group of inorganic crystalline materials having two-dimensional framework connectivity. These material are made of stacks of ultra thin layers/sheets (~1-2 nm) separated by the so-called gallery space which can be occupied by water molecules, ions (e.g. sodium, potassium) or organic molecules. Layered silicates, or clays are well known example of such layered materials which consists of stacks of silicate layers formed by covalent bonding of silica tetrahedral in a two dimensional fashion.[107,108] Besides clays, there are a variety of materials like aluminum phosphates (AlPOs)[109], layered double hydroxides (LDH)[110], layered zeolite precursors[111,112], metal titanates[113], etc. which have similar layered morphology.

The most interesting aspect of the layered materials is their ion-exchange ability which allows insertion of a range of foreign species into the inter-layer gallery space via soft chemical processes (a process often known as swelling), yielding a diverse range of materials with peculiar chemical and physical properties. The swollen materials can be further exfoliated to obtain individual nano-thick sheets. Due to this flexibility of structural modification, layered materials have been used in various applications such as catalysis[108,114,115], adsorption, polymer nanocomposites[116], etc. We are interested in layered materials with porous layers, which can separate one gas molecule from other. Some of these materials have been described in this section.

4.1.1 Porous layered materials

Porous layered materials have the potential to provide very thin, high aspect ratio layers with molecular sieving ability. Zeolites, aluminum phosphates and certain silicates have such porous structure. However, only a few of such materials crystallize as two dimensional layers. The choice of layered material depends on the appropriate pore size which can perform the particular gas separation. However, other practical issues such as the stability of material and exfoliation of material without structural destruction often influence the material selection.

Zeolites are crystalline aluminosilicate materials (made of SiO_4 and/or AlO_4 tetrahedra) well known for their molecular sieving ability. These materials provide a range of pore sizes (~3-10 Å) which are ideally suited for separation of gas molecules. Apart from the molecular sieving ability, these materials have high thermal and chemical stability which is useful for high temperature separation applications. Although most of the zeolites exist as 3-D framework material, certain zeolite precursors with layered morphology have been identified[112,117-123], which can provide ultrathin porous layers upon swelling and exfoliation. However, such processes often result in structural destruction (viz. destruction of layer morphology and pore structure) due to very harsh chemical conditions required to overcome the strong interlayer forces.[124-127] Thus, utilization of these materials for membrane applications requires the development of efficient swelling and exfoliation procedures which preserve the structure of these materials.

Aluminophosphates (AlPOs) is another class of materials with molecular sieving properties. These materials are structurally similar to zeolites, but are built from AlO_4 and PO_4 tetrahedra units.[109] Unlike layered zeolites which are few in number, a variety of layered AlPOs with a wide range of pore sizes have been reported.[109,128] However, swelling and exfoliation of these materials poses a challenge due to extremely large crystal sizes (few 100 microns) and limited stability of these materials. Some of these materials have been recently reported to be successfully swollen and exfoliated.[129,130] Further investigation, directed towards reducing the crystal sizes and improving the stability of layers, can make these materials promising for membrane applications.

As evident from the above discussion, formation of ultrathin porous layers from layered materials requires developing efficient swelling and exfoliation procedures which do not result in structural destruction. One such example is provided in next few sections where a zeolite precursor, MCM-22(P) is swollen and exfoliated while preserving its layered morphology and pore structure.

4.2 MCM-22 and MCM-22(P) as selective phase of mixed matrix membranes

MCM-22(P) is a layered zeolite precursor synthesized by Mobil group.[112] This material is composed of 2.5 nm thick porous sheets stacked in registry along the [001] direction, with an organic amine (hexamethyleneimine, HMI) occupying the gallery space between the layers (see Figure 4.1A). Each sheet/layer consists of a bidimensional 10-member ring (MR) sinusoidal channel pore system (as seen occupied by HMI molecules in Figure 4.1A) and a hexagonal array of 'hourglass pockets' or 'cups' on the (001) plane having 12MR apertures on both sides of the layers (shown by grey color in Figure 4.1).[131] These large cups are connected to each other through double 6-MR necks (shown by pink color in Figure 4.1). Upon calcinations of MCM-22(P), the layers condense together to form a 3-D framework structure, MCM-22 with the elimination of HMI molecules (Figure 4.1C).

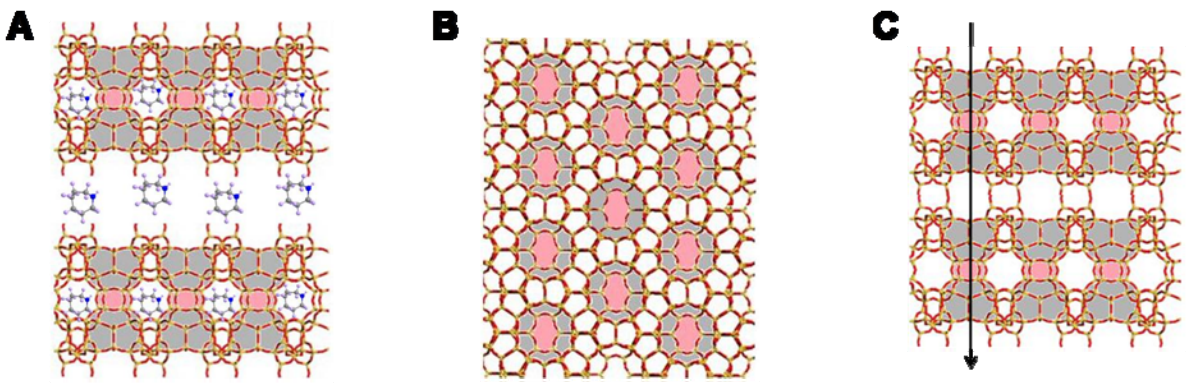

Figure 4.1. A: Schematic of MCM-22(P) viewed in a direction parallel to the microporous layers (lamellae). Organic amine, HMI occupies positions within the layers and in the gallery space (between lamellae). 12-member ring (12MR) hourglass pores are highlighted in grey while the transport limiting 6MRs are highlighted in pink. B. Schematic of a microporous lamella viewed along its thin dimension. The 6MRs are again highlighted in pink while the 12MR hourglass pores leading to the 6MR transport limiting pores are highlighted in grey. C. Upon calcination, the layers condense together to form MCM-22 as shown in rightmost image. The arrow marks a transport path of a molecule travelling along the c-axis perpendicular to the layers.

MCM-22(P) or MCM-22 can act as hydrogen selective materials as the gas molecules larger than hydrogen cannot penetrate along the c-axis (see Figure 4.1C), due to the small 6MR necks. A proof of hydrogen selectivity of 6MR has been shown previously in Tsapatsis group, where mixed matrix membranes of MCM-22 crystals with mesoporous silica matrix showed improved selectivity for H_2 over CO_2 and H_2 over N_2.[132,133] The MCM-22 crystals used for making these films were plate-like particles which were about 100 nm in thickness and ~1000 nm in diameter. Each of these crystals consists of approximately 40 individuals sheets condensed together. Conceptually, any one of these sheets should be sufficient to carry out the separation of hydrogen because the 6MR ring will completely inhibit the transport of gases larger than hydrogen. Thus, replacing the MCM-22 crystals with single 2.5 nm layers, obtained by exfoliation of MCM-22(P), can increase the hydrogen permeance by an order of magnitude without reducing the selectivity.

Fabrication of polymer nanocomposites with MCM-22(P) requires intercalation of polymer chains in between the layers. To facilitate the intercalation, the material needs to be swollen with organic surfactant to increase the inter-layer spacing. The increased inter-layer spacing allows intercalation of polymer chains resulting in nanocomposites with intercalated or exfoliated morphology.[116,134]

Kresge and co-workers[135-137] have demonstrated a method to swell MCM-22(P) layers by treatment with a base, tetrapropylammonium hydroxide (TPAOH), and a long chain surfactant, cetyl trimethyl ammonium bromide (CTAB) under high pH and elevated temperature conditions. The swollen material can subsequently be pillared to produce a catalytically active material, MCM-36, with a very high surface area. Corma and co-workers[114,138] used ultrasonication to exfoliate the swollen material to produce a delaminated zeolite material, ITQ-2, with further improvements in the catalytic activity. ITQ-2 contains exfoliated single crystalline layers with the pore structure of MCM-22(P) layers.

Given that the swelling and exfoliation methods for MCM-22(P) are already well established.[114,137] a mixed matrix composite with exfoliated MCM-22 layers would seem straightforward. However, it has been recognized[125,126,131] that swelling of MCM-22(P) by treatment with TPAOH and CTAB at elevated temperature and high pH results in layer fragmentation along with partial dissolution of the framework silica. Schenkel et. al.[125] have reported a significant reduction in Si/Al ratio as a result of swelling and exfoliation procedures due to dissolution of silica. Apparently, partial MCM-22(P) dissolution during high temperature swelling does not prohibit catalytic uses as demonstrated by successful applications of ITQ-2[114,139] and MCM-36.[139-141] However, it can significantly compromise the performance of nanocomposite membranes as a reduction in the aspect ratio of the layers can impair the separation capabilities of the membrane. Moreover, the amorphous silica produced by the dissolution of crystals may have an undesirable influence over the transport and separation properties of the membrane and may also cause processing problems during nanocomposite fabrication (e.g., due to aggregation).

Here, an approach to swell MCM-22(P) without disruption of the layered structure has been described. Relatively mild conditions are used as compared to the high-temperature basic conditions employed in the reported swelling procedures.[114,135-138] The resulting swollen material is compared with one swollen at elevated temperature to highlight the structural differences in the two materials. Reversibility of the swelling process is demonstrated, which represents a major difference from high temperature methods that yield irreversibly swollen products. In addition to providing a modified approach to swell MCM-22(P) layers, this work enhances our understanding of the swelling of MCM-22(P) and presents a possible mechanism for reversible swelling. The swollen material has been successfully pillared to produce an MCM-36 analogue. Also, nanocomposites of swollen MCM-22(P) with polystyrene exhibiting partially exfoliated morphology of layers are demonstrated.

4.3 Experimental Section

Synthesis of MCM-22(P)

MCM-22(P) was synthesized using the method described by Corma et al.[114,138] Typically, 0.72 g of sodium aluminate (MP biomedicals, USA) and 2.48 g of sodium hydroxide (97+ %, Fisher) were dissolved in 311 g of distilled water. Subsequently, 19.1 g of hexamethyleneimine (HMI) (Aldrich) and 23.6 g of fumed silica (Cab-o-sil M5) were added to the mixture. The mixture was allowed to stir for 5 h at room temperature, followed by 11 days in rotating teflon-lined steel autoclaves at 408 K. The crystalline product obtained after 11 days was collected by centrifugation and repeatedly washed with distilled water to reduce the pH to 9. A portion of the crystalline product was calcined at 540 °C under air for 12 h to produce MCM-22.

Swelling and Pillaring of MCM-22(P)

MCM-22(P) was swollen with CTAB at room temperature under high pH conditions. The composition of the swelling mixture was the same as reported by Kresge[137] and Corma.[114,138] Typically 9.0 g of aqueous slurry of MCM-22(P) (20 wt% solids) was mixed with 35.0 g of an aqueous solution of 29 wt% CTAB (Aldrich) and 11.0 g of an aqueous solution of 40 wt% TPAOH (Alfa Aesar). The pH of the resulting mixture was typically 13.80. The mixture was allowed to stir for 16 h at room temperature, after which, the particles were recovered by repeated cycles of centrifugation and water washing (10 min centrifugation at 10000 rpm, and redispersion in fresh water). The number of (centrifugation/water washing) cycles was systematically varied from 10 to 40 to study its effect on the recorded XRD patterns. A portion of the mixture, recovered after 16 h of swelling, was subjected to ultrasonication for 2 h using a Branson 5510 ultrasonic cleaner, to attempt exfoliation of the layers,[114] and subsequently acidified to pH<2 to collect the particles. For comparison, a portion of MCM-22(P) was also swollen at elevated temperature (80 °C) following the procedure reported by Corma et al.[114,138]

Pillaring of the swollen material was performed according to the procedure reported by Barth et al.[142] Typically, 1.0 g of swollen MCM-22(P) powder was mixed with 5.0 g of TEOS (tetraethoxysilane, Fluka), stirred for 25 h at 351 K under an argon atmosphere, then filtered and dried at room temperature. The dried solid (0.5 g) was hydrolyzed with water (5.0 g, pH ~ 8, controlled with NaOH) for 6 h at 313 K, and then filtered, dried at 300 K and calcined at 723 K under N_2 flow (140 ml min^{-1}) for 6 h and finally at 823 K under air for 12 h (temperature ramp rate of 2 K/min).

Polystyrene-swollen MCM-22(P) nanocomposite fabrication

a) Nanocomposite from solution casting techniques: Nanocomposites of room temperature swollen MCM-22(P) and polystyrene were prepared using solvent blending techniques. A 2 wt% dispersion of swollen MCM-22(P) was prepared in toluene. To assist homogeneous dispersion, the mixture was subjected to ten cycles of sonication and refluxing (6 h sonication, 6 h refluxing). The resulting dispersion (1.0 g) was mixed with 1.0 g of 2 wt% polystyrene (M_n = 5400) solution in toluene and stirred for 5 days. Subsequently, the mixture was heated for 2 h at 110 ˚C, followed by addition of 5.0 g of 20 wt% solution of polystyrene (M_n = 45000), further heating (2 h, 110 ˚C), sonication (1 h) and finally casting on a Teflon plate. The solvent was evaporated slowly over a period of 5 days and the composite was peeled off the surface.

b) Nanocomposite from melt compounding techniques: Nanocomposites were prepared by melt blending in a DACA Mini Compounder vertical, co-rotating twin screw extruder with a re-circulation channel. Polystyrene (3.8 g, M_n = 45000) and room temperature swollen MCM-22(P) (0.16 g) were mixed manually and loaded into the compounder preheated to 120 ˚C. The mixture was blended at a screw speed of 350 rpm for 15 min under nitrogen and subsequently extruded out. A circular disc (25 mm × 1 mm) was prepared by compressing the extrudate at 1000 psi and 150 ˚C for 10 min.

Characterization Methods

The silicon and aluminum contents of MCM-22(P), and of the swollen materials, were determined using Inductive Couple Plasma Mass Spectroscopy (ICP-MS) analysis conducted at Galbraith Laboratories, USA.

Powder X-ray diffraction (XRD) patterns were collected on a Bruker AXS D5005 diffractometer using Cu-Kα radiation to characterize the swelling and pillaring of MCM-22(P). Data were collected in the 2θ range from 0.65° to 30° with a step size of 0.04° and a step time of 3 s.

Thermogravimetric analysis (TGA) was performed to estimate the amount of organic contents in MCM-22(P) and swollen materials. Experiments were carried out under air in the temperature range of 110-800 °C (heating rate 10 °C/min) on a Perkin-ElmerTGA-7 analyzer attached to a PC via a TAV7/DX thermal controller.

All NMR spectra were recorded at a field of 9.4 T (BRUKER Avance 400). ^{29}Si MAS NMR spectra were recorded at 79.49 MHz using 7 mm rotors at a spinning speed of 4 kHz, a dwell time of 5μs, a π/2 pulse of 3.0 μs and a recycle delay of 60 s. All spectra were referenced with respect to tetramethylsilane (0 ppm). ^{27}Al MAS NMR spectra were recorded at 104.26 MHz using 4 mm rotors at 12 kHz spinning speed, a dwell time of 2.5 μs, a selective π/6 pulse of 0.6 μs and a recycle delay of 1 s. An aqueous solution of aluminum sulfate (0.1 M) was used as the reference (0 ppm). ^{29}Si(^{1}H) CPMAS NMR spectra were acquired using 7 mm rotors at a spinning speed of 4 kHz, a dwell time of 5 μs, a ^{1}H π/2 pulse of 4.5 μs, high power ^{1}H decoupling, and a recycle delay of 10 s. The Hartmann-Hahn matching conditions were determined using a sample of tetrakis(trimethylsilyl)silane ($Si[Si(CH_3)_3]_4$).

The crystal morphologies of various materials were examined by scanning electron microscopy (SEM, JEOL 6500) operating at an accelerating voltage of 5 kV. Samples were coated with platinum (50 Å thickness) before imaging.

A FEI Tecnai G2 F30 transmission electron microscope (TEM) equipped with a charge couple device (CCD) and operated at 300 kV was used for direct imaging of various samples. Samples were prepared by sprinkling the powders onto a carbon coated copper grid. For imaging swollen MCM-22(P) from toluene dispersions, a few droplets were placed on a copper grid and allowed to air dry. For polymer nanocomposites, a JEOL 1210 microscope operating at 120kV was used for visualization. A Reichert Ultracut S Ultramicrotome equipped with a diamond knife was used for TEM sample preparation to obtain 50-80 nm thick slices of nanocomposite.

Nitrogen adsorption–desorption measurements were carried out at -196 °C on a Autosorb-1 analyzer (Quantachrome Instruments). Prior to measurement, samples were evacuated overnight at 350 °C and 1 mmHg.

4.4 Results and Discussion

XRD and TGA

MCM-22(P) has been swollen by CTAB into a highly ordered material and the swelling can be reversed by acidification of the sample. The XRD patterns of MCM-22(P) before and after swelling and repeated centrifuging/washing are reported in Figure 4.2. The XRD pattern for MCM-22(P) (Figure 4.2 trace a) is in agreement with those reported in the literature.[114] Room temperature swollen MCM-22(P) (MCM-22(PS-RT)), shows a shift of the 001 peak to lower angles (Figure 4.2A traces b-e) indicating an increase in layer spacing from 27 Å to about 42 Å. Peaks 220 and 310 are not affected by swelling, indicating preservation of the crystal structure within the layer. The hkl peaks along the c-axis (perpendicular to layers) either disappeared or became broader due to the changes in the crystal structure. The 101 and 102 reflections merge together to form a broader peak, as reported previously.[143]

Traces b-e in Figure 4.2 show the evolution of the swollen structure as a result of repeated washing/centrifuging. The swollen material after 10 cycles of washing (Trace b) shows a new peak around a 2θ value of 5.5°. The origin of this peak is not known. Roth and Vartuli[143] report a similar response in swollen MCM-22(P). Further washings

resulted in disappearance of this peak and emergence of two new peaks around 2θ angles of 4.5° and 6.5°. Also, the 001 peak shifts towards slightly higher angles. The two new peaks can be indexed as 002 and 003 based on the position of the 001 peak. These peaks are not present in MCM-22(P) swollen at elevated temperature (MCM-22(PS-80)) (Figure 4.2, trace g). Also, the peaks are much broader in MCM-22(PS-80), indicating a greater degree of disorder. The room temperature swelling procedure results in an expanded material with less broadening of peaks as compared to what results when MCM-22(P) is swollen at high temperature. In addition, we obtained 002 and 003 reflections, indicating long range order of layers in the swollen material. To the best of our knowledge, these reflections have never been reported before in the swollen material and support our claim of a higher degree of ordering as compared to MCM-22(P) swollen at higher temperature.

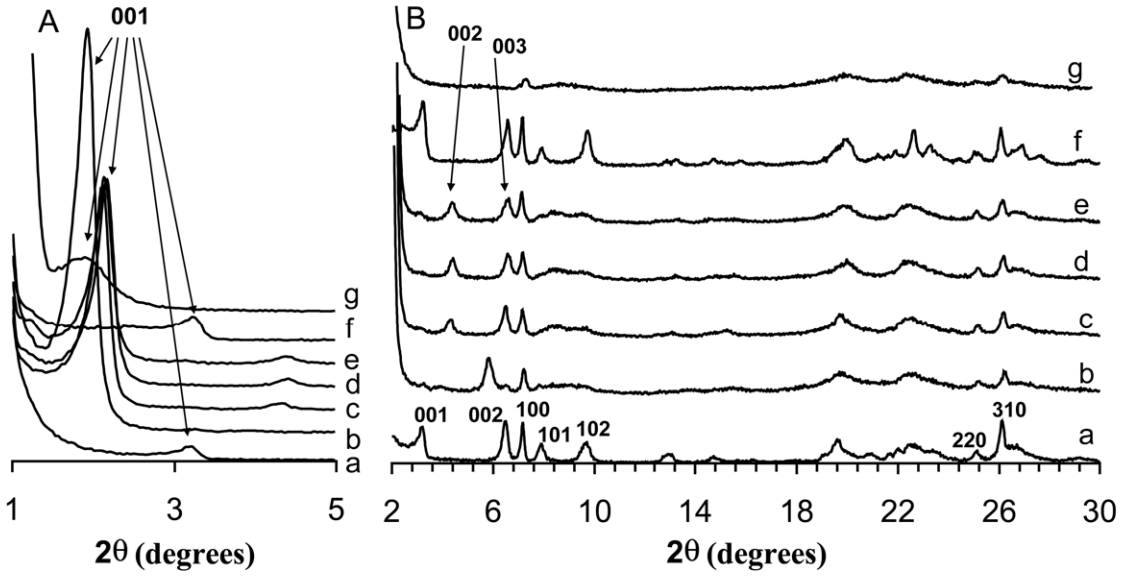

Figure 4.2. XRD patterns of a) MCM-22(P); MCM-22(PS-RT) after b) 10 washes, c) 20 washes, d) 30 washes, e) 40 washes; f) deswollen material obtained after acidification of MCM-22(PS-RT), g) MCM-22(PS-80). Figure 4.2 has been divided into A and B for better visualization of the 001 peak, and traces have been shifted vertically for the sake of clarity.

The TGA curves (Figure 4.3, (2)-(4)) reveal that repeated washings result in a decrease in the organic content in MCM-22(PS-RT), presumably due to removal of

CTAB. It seems reasonable to assume that partial removal of CTAB, which might be loosely held in between the layers, results in a more ordered lamellar structure (as evidenced by the emergence of 002 and 003 peaks). This assumption is supported by the slight shift of the 001 peak to larger angles (and hence a decrease in layer spacing as a result of CTAB removal) and the observed reduction in organic content of MCM-22(PS-RT) as a result of repeated washings. We do not completely understand the evolution of structure, viz. the origin and disappearance of the 2θ = 5.5° reflection. However, the XRD pattern of the final swollen structure is well defined.

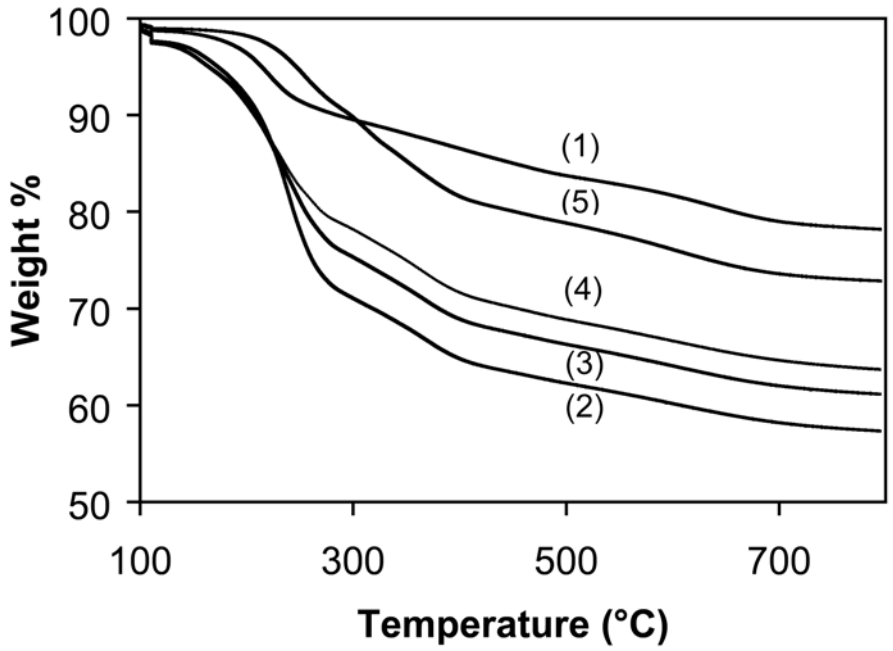

Figure 4.3. TGA curves for (1) MCM-22(P); MCM-22(PS-RT) after (2) 10 washes, (3) 20 washes and, (4) 40 washes; (5) deswollen material obtained by acidification of MCM-22(PS-RT).

Si/Al Ratio

The pH at the end of the room temperature swelling procedure was found to be approximately equal to the starting pH of 13.80. On the other hand, the swelling procedures at 80 °C resulted in a significantly lower pH of 12.99. These observations can be explained by comparing the Si/Al ratio of the respective materials. MCM-22(P) had a

Si/Al ratio of 46.7 as compared to 43.2 for MCM-22(PS-RT) and 11.8 for MCM-22(PS-80). The decrease in Si/Al ratio as a result of swelling indicates some dissolution of framework silica. The dissolved silica forms mono silicic acid and other oligomeric silicates in the solution, which on deprotonation, decrease the pH of the solution. Greater dissolution occurs at elevated temperature. Schenkel et al.[125] also report a large reduction in Si/Al ratio, from 33.3 to 20.1, as a result of swelling MCM-22(P) starting with an initial pH of 13.5.

Reversible Swelling

A remarkable feature of the room temperature swelling procedure is that the process can be reversed by acidification. Figure 4.2B (trace f) shows the XRD pattern of the material obtained by acidification of MCM-22(PS-RT), which appears to be same as that of MCM-22(P). The TGA curve for this material (Figure 4.3, trace (5)) shows considerably lower organic content than MCM-22(PS-RT), which suggests the removal of CTAB as a result of acidification. The XRD pattern and the TGA analysis suggest that the acidification results in exchange of CTAB for protons and the layers reassemble to form the MCM-22(P) structure with a characteristic layer spacing of 2.7 nm. The sequence is depicted in Figure 4.4. In fact, MCM-22(PS-RT) samples at any stage of washing can be reversed back to MCM-22(P) structure by suspending them in aqueous solution with pH<2. Reversibility of the swelling suggests that HMI, initially present in MCM-22(P), most likely remains in between the layers after swelling and directs the reassembly of the layers to the original MCM-22(P) structure upon CTAB removal. However, further investigations are needed to test this hypothesis. Such reversibility does not occur with MCM-22(PS-80), possibly because the layers are broken due to partial dissolution of framework silica. Thus, the resulting material likely has disordered layers that are completely out of registry, which cannot be deswollen back to the MCM-22(P) structure. Instead, ITQ-2 is obtained upon acidification.[114] Further, our preliminary results on swelling MCM-22(P) at various temperatures, ranging from room temperature to 80 ºC, suggest that the swelling reversibility behavior changes at a temperature of about 55 ºC. At lower temperatures, the swollen material can be restored back to MCM-

22(P) while above this temperature, reversibility is lost. This result is in agreement with our argument that swelling at high temperatures results in partial dissolution of framework silica and destruction of layered structure which prevents reversibility of the swelling process.

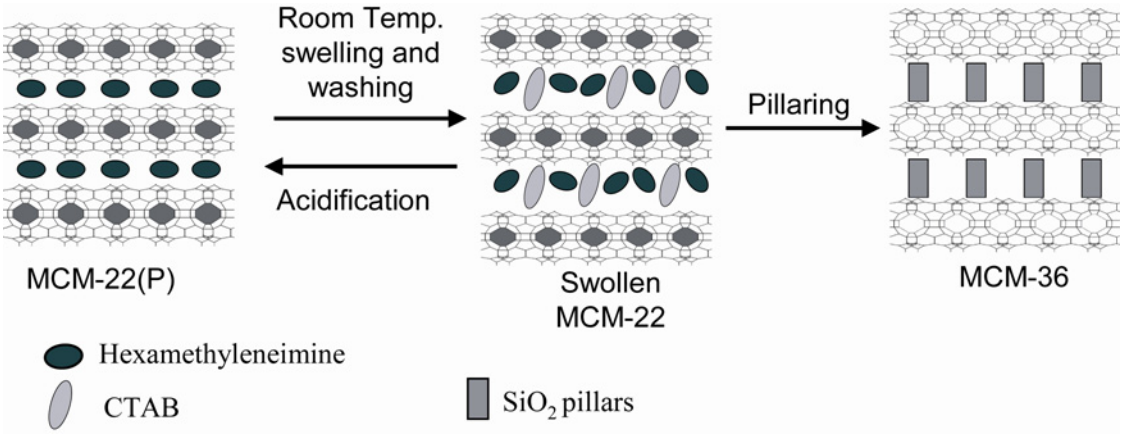

Figure 4.4. Illustration showing the reversible swelling of MCM-22(P) and pillaring of the swollen material. The swollen material can be deswollen back to MCM-22(P) by acidification, suggesting exchange of CTAB surfactant with protons.

Multinuclear Solid-state NMR Investigation

Solid-state ^{27}Al and ^{29}Si MAS NMR and ^{29}Si CPMAS NMR were employed to investigate the structural differences and coordination environment in precursor, swollen and deswollen MCM-22(P) materials. Figure 4.5, trace (a), shows a typical ^{29}Si MAS spectrum of MCM-22(P). The main resonances are from silicon atoms coordinated with four silicon atoms (Q^4) due to the low aluminum content of the precursor (Q^n stands for $X_{4-n}Si[OSi]_n$, X = OH or O^- and the expected $Si(1Al)/Q^4$ ratio ~1:10). Three well-resolved lines, appearing at -104 ppm, -110 ppm and -114 ppm, together with two less resolved shoulders at -116.8 ppm and -119 ppm, are attributed to crystallographically nonequivalent framework Q^4 tetrahedral sites (T-sites). These resonances have been tentatively assigned to distinct T-sites by comparing experimental spectra with simulated ^{29}Si MAS NMR spectra of MCM-22 using the Si-O-Si bond angles of the proposed MCM-22 structure.[144-148] The ambiguity in assignment arises due to two possible space

groups (P6/mmm and Cmmm) that have been proposed for MCM-22 based on XRD[112] with each space group having a different number of distinct T-sites. However, the P6/mmm space group has been found to more satisfactorily explain both the ^{29}Si NMR[144,145,147,149] and ^{27}Al NMR[147,150] spectra and the electron diffraction data.[151]

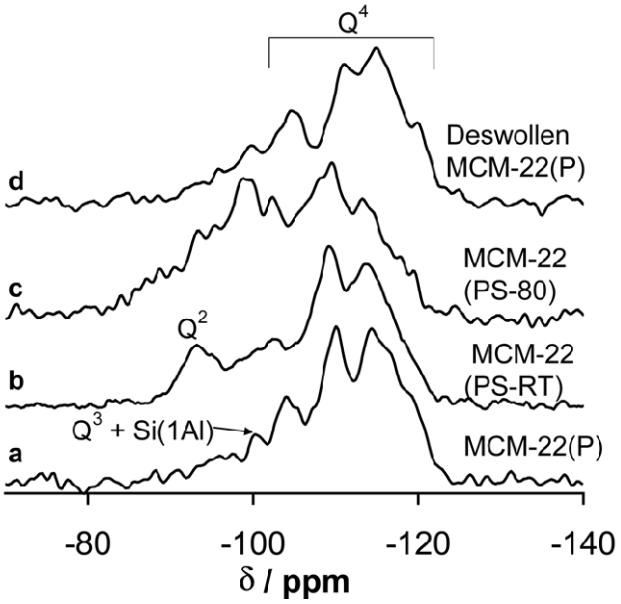

Figure 4.5. ^{29}Si MAS NMR spectra of a) MCM-22(P), b) MCM-22(PS-RT), c) MCM-22(PS-80) and, d) deswollen MCM-22(P) obtained by acidification of MCM-22(PS-RT).

Based on the P6/mmm symmetry, the observed resonances in the ^{29}Si MAS NMR spectra are consistent with the following T-sites (see Figure 4.6): -104ppm (T_2), -110ppm (T_3+T_5+T_4), -114ppm (T_8), -116.8 ppm (T_7) and -119 ppm (T_6).[144,145] The line at -100 ppm is due to both Q^3 configuration and the Si(1Al) groups, which appear at the same chemical shift.[152-154] The Q^3 resonances come from the T_1 sites (4 per unit cell) along with certain structural defects which lack connectivity between two Si atoms. Given the high Si/Al ratio of this sample, the Q^3 peak will dominate over the Si(1Al) peak (assuming Q^3 contributions only from the T_1 sites, the expected Si(1Al)/Q^3 ratio will be 1:2.6).

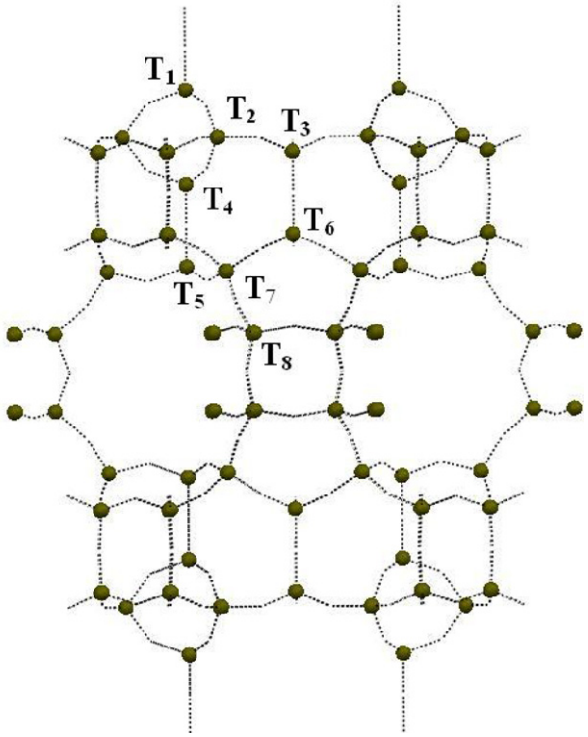

Figure 4.6. Projection of the MCM-22(P) unit cell indicating the eight crystallographically unequivalent tetrahedral sites.

Figure 4.5, trace b shows the ^{29}Si MAS NMR spectrum for MCM-22(PS-RT). The spectrum is qualitatively very similar to that of MCM-22(P). There is a slight low-field shift of the Q^4 peaks, possibly indicating relaxation of the structure by a reduction of the Si-O-Si bond angles. The primary differences between the two samples are the appearance of a more significant resonance at -93 ppm and the reduction in the intensity of the -116.8 and -119 ppm resonances in the MCM-22(PS-RT) spectra. The -93ppm peak is assigned to Q^2 groups[139,144,145], and likely arises as a result of breaking some of the Si-O-Si connectivity during swelling. The reduction in the intensity of the -116.8 and -119 ppm resonances suggests there may be some structural changes around T_6 and T_7 sites, which could either be simply a reduction in the Si-O-Si angle, making them indistinguishable from other T-sites, or might be due to bond breaking around T_6 and T_7 sites. However, given that the T_6 and T_7 sites lie well protected inside the layer structure (see Figure 4.6), these are unlikely to undergo bond breakage during swelling (which is

more likely to occur around the T_1, T_2 and T_3 sites, which are near the layer surface). Despite these differences, the overall similarity between the MCM-22(P) and MCM-22(PS-RT) spectra shows that the precursor has been swollen with minimal change in the local environment of the framework structure. In contrast, MCM-22(PS-80) has a very different spectrum (Figure 4.5, Trace c). There is a significant increase in the spectral intensity between -95 and -105 ppm and a substantial broadening of all resonances suggesting the creation of Q^3 and Q^2 defect sites by breaking Si-O-Si bonds. A decrease in the Si/Al ratio (Si/Al~12) implies that Si(1Al) peaks, which appear downfield to the corresponding Q^4 peaks, will also have a significant contribution to the spectra, thereby increasing the overall intensity in this chemical shift range. The overall spectrum of this material suggests an increased dispersion in the local bonding environments.

Figure 4.5, trace d shows the ^{29}Si MAS NMR spectrum for deswollen MCM-22(P) obtained by acidification of MCM-22(PS-RT). The spectra shows re-emergence of -104 and -119 ppm resonances which were present in MCM-22(P) but decreased in intensity after room temperature swelling (Figure 4.5, trace b). The spectrum is qualitatively very similar to that of MCM-22(P), and supports the reversibility of the room temperature swelling procedure as already seen in the XRD patterns of these materials.

The ^{29}Si CPMAS NMR spectra were acquired for all samples to gain further insight into the structural aspects and to distinguish between the Q^3 and Si(1Al) peaks. Two different contact times of 1 ms and 7 ms were employed. The spectra are shown in Figure 4.7. For both MCM-22(P) and MCM-22(PS-RT) an increase in the contact time results in a relative increase in the Q^4 resonances due to the increased magnetization transfer (i.e. spin diffusion) observed at longer cross-polarization times, leading to an apparent decrease in the Q^3 and Q^2signals (compare Figure 4.7a to 4.7b and 4.7c to 4.7d). At a short contact time (1 ms), the Q^3 and Q^2 species are more rapidly polarized than the Q^4 species because they are in closer proximity to the organic protons and/or silanols.[155] At the longer contact times, the magnetization transfer is more diffuse in that enhancement of all silicon species is observed. Thus, the (apparent) decrease in the -100

ppm peak intensity in MCM-22(P) and MCM-22(PS-RT) reflects the Q^3 contribution to this peak as suggested earlier. In addition, the spectrum of MCM-22(P) shows a resonance around -94 ppm that was not visible in the corresponding ^{29}Si MAS NMR spectrum (Figure 4.5, trace a). This resonance is probably due to the presence of small amount of Q^2 defects in the MCM-22(P) structure, which becomes visible only in cross polarization (CP) mode. MCM-22(PS-80) shows a large contribution from a very broad peak centered around -100ppm (Figures 4.7e and 4.7f). This contribution is expected for two reasons: Q^3 species created as a result of swelling and, increased dominance of the Si(1Al) peak as a result of a decreased Si/Al ratio. The ^{29}Si CPMAS NMR of deswollen MCM-22(P) with a 1 ms contact time (Figure 4.7g) shows a substantial enhancement of the resonances between -90 to -100 ppm, indicating selective magnetization transfer. This is much more pronounced in the deswollen sample as compared to the MCM-22(PS-RT) or MCM-22(P). A likely explanation for this could be that at the high pH (13.8) used for swelling, many of the silanol groups become deprotonated, and that upon acidification they become reprotonated.

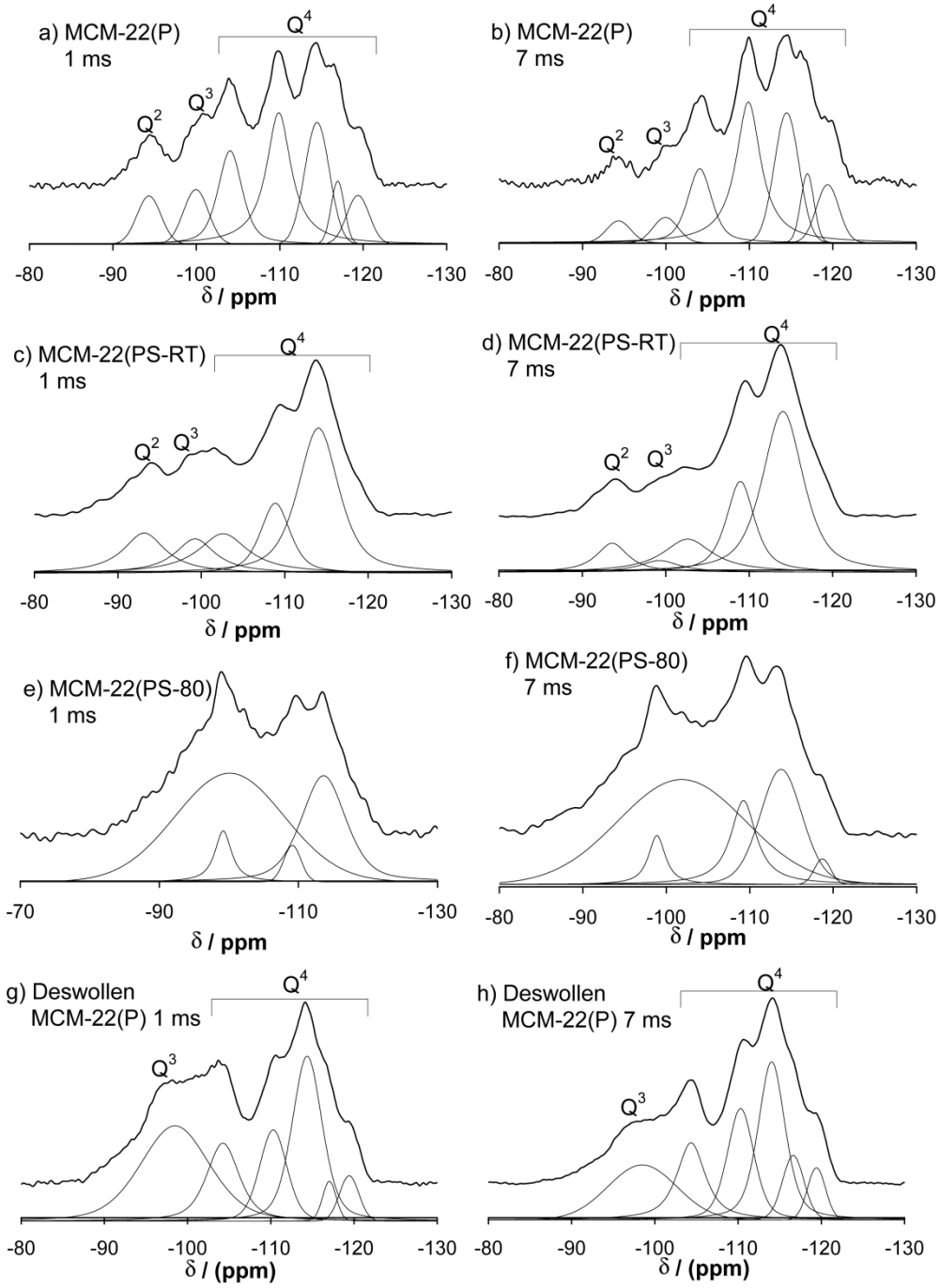

Figure 4.7. ^{29}Si CPMAS NMR spectra of MCM-22(P) a) contact time 1 ms, b) contact time 7 ms; MCM-22(PS-RT) c) contact time 1 ms d) contact time 7 ms; MCM-22(PS-80) e) contact time 1 ms f) contact time 7 ms and, deswollen MCM-22(P) g) contact time 1 ms h) contact time 7 ms. In each figure, the top curve represents the spectra obtained experimentally and bottom curves represent the deconvolution into individual peaks.

The ^{27}Al NMR spectra for various materials are shown in Figure 4.8. All four materials show two peaks around 50 and 56 ppm, consistent with previous reports.[147,150,152,153] These peaks have been assigned to two different sets of T-sites, differentiated by location in the framework.[150,153] Kennedy et al.[150] used the Si-O-Al bond angles obtained from the structure of MCM-22 to calculate the chemical shifts of various T-sites. By comparing calculated chemical shifts to experimentally observed shifts, the T_6 and T_7 sites were assigned to the 50 ppm resonance and all the other T-sites to the 56 ppm resonance. Swelling MCM-22(P) results in the reduction of the 50 ppm peak intensity (Figure 4.8, traces b and c), which suggests some structural changes around the T_6 and T_7 sites. This observation is in agreement with the ^{29}Si MAS NMR results, which also indicated structural changes around these T-sites. Overall, the NMR spectrum of MCM-22(PS-RT) more closely resembles the one obtained from MCM-22(P) as opposed to the one derived from MCM-22(PS-80). Deswollen MCM-22(P) (Figure 4.8, trace d) has a spectrum similar to those obtained from MCM-22(PS-RT) and MCM-22(P) materials, indicating a close structural relationship between the three materials.

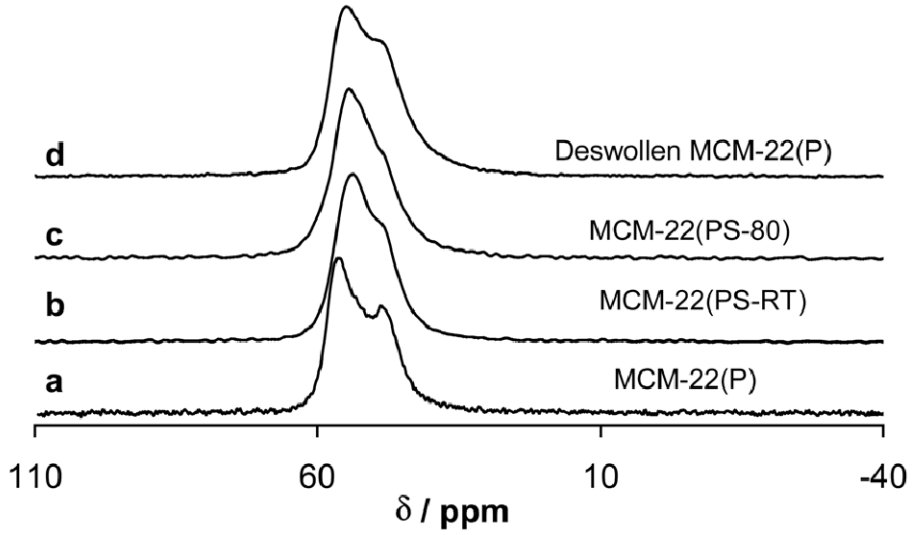

Figure 4.8. ^{27}Al MAS NMR spectra of a) MCM-22(P), b) MCM22 (PS-RT), c) MCM-22(PS-80) and, d) Deswollen MCM-22(P) obtained by acidification of MCM-22(PS-RT).

Based on the ^{29}Si MAS NMR and the ^{27}Al NMR results, we conclude that swelling MCM-22(P) at room temperature largely preserves the layer structure, in contrast to the significant structural disruptions that occur at 80 ˚C. Room temperature swelling does lead to certain specific structural differences, around T_6 and T_7 sites, which may reflect a reduction in the average Si-O-Si bond angle at these sites.

Electron Microscopy

SEM images obtained from the precursor and swollen materials are shown in Figure 4.9. The MCM-22(P) crystals (Figure 4.9a) are thin rounded flakes, less than a micron in diameter. Swelling at room temperature, and 10 and 40 subsequent washes, does not result in any significant changes in the crystal morphology as evidenced by comparing Figures 4.9a, 4.9b and 4.9c; recall, however, differences in the XRD patterns (Figure 4.2, trace b and trace e) noted earlier. Swelling at an elevated temperature does produce significant morphological changes as shown in Figure 4.9d. The crystals no longer have sharp edges and appear to be highly curled and broken. This is likely due to the dissolution of framework silica.

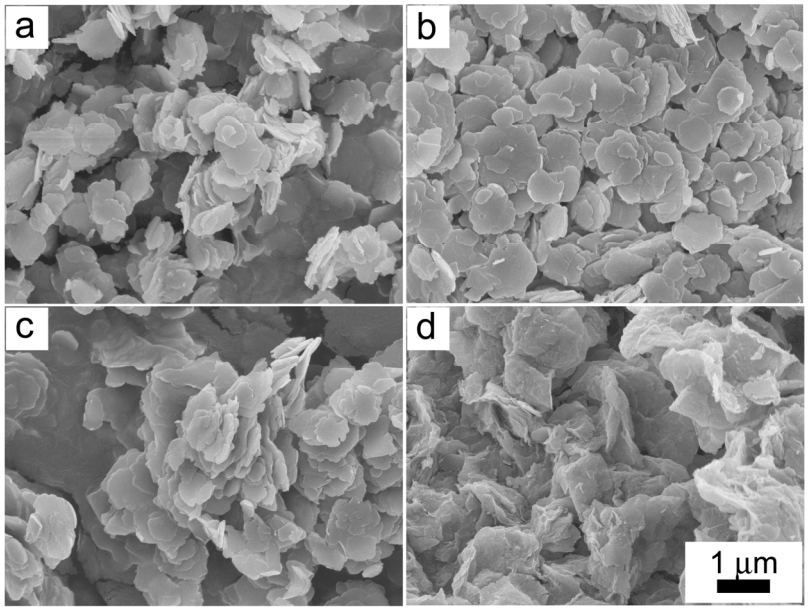

Figure 4.9. SEM images of a) MCM-22(P), MCM-22(PS-RT) after b) 10 washes, c) 40 washes, d) MCM-22(PS-80).

Figure 4.10 shows low magnification TEM images of various samples. MCM-22(P) has a thin flake-like morphology (Figure 4.10a) with layers stacked over each other in a lamellar arrangement (Figure 4.10b). Swelling at room temperature does not lead to any major changes in the particle morphology, as already seen by SEM and further shown by a TEM micrograph in Figure 4.10c. In contrast, Figure 4.10d, which shows the morphology of the material swollen at 80 ˚C, clearly shows the loss of lamellar morphology and crystal facets. Layers appear to be curled, partially delaminated and out of registry.

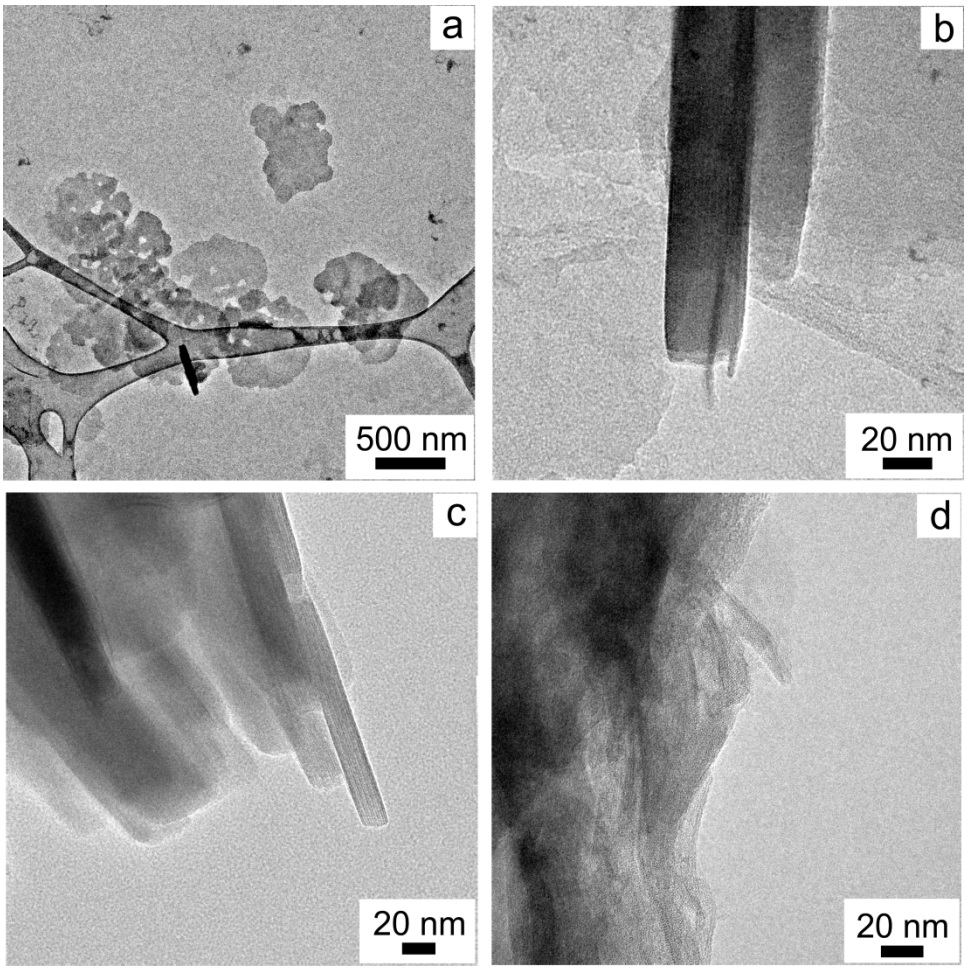

Figure 4.10. TEM images of (a) MCM-22(P) perpendicular to layer thickness, (b) MCM-22(P) edge-on view, (c) MCM-22(PS-RT), and (d) MCM-22(PS-80).

High-resolution TEM (HRTEM) was used to examine the structure of individual layers and the associated gallery spacing. Figure 4.11 shows TEM micrographs for various specimens. Structural schematics of MCM-22(P) have been overlaid on the TEM micrographs in order to guide visualization. MCM-22(P) (Figure 4.11a) shows ~2.5 nm thick layers. Each layer appears as two dark bands separated by a bright band. The bright band is attributed to the 10-MR pore system within the layer, while the dark bands appear due to the higher silica density in the remaining parts of the layer (top and bottom). The gallery space between the two layers also appears as a bright band. MCM-22(PS-RT) (Figure 4.11b) displays well ordered layers with an expanded interlayer distance relative to MCM-22(P). Shown in Figure 4.11c is a TEM image of the material obtained by acidification of MCM-22(PS-RT). This image shows the layer spacing and structure corresponding to MCM-22(P) and is consistent with Figure 4.11a. This provides another piece of evidence, in addition to XRD, for the reversible swelling of MCM-22(P) at room temperature. TEM images of MCM-22(PS-80) are shown in Figures 4.11d-f. MCM-22(PS-80) shows a different morphology than MCM-22(PS-RT). Here, crystals appear to be much more fragmented, with curled layers and amorphous regions. As evidenced by Figures 4.11d and 4.11e, the layers generally lack the long range ordered stacking obtained for MCM-22(PS-RT). Figure 4.11e shows a swollen particle with a part containing well resolved layers and another part that looks amorphous. Although some ordered layers with increased inter layer spacing were observed (Figure 4.11f), such regions make up a minor fraction of the specimen examined. We conclude that the hot basic conditions used for swelling the sample partly degrade the structure and dissolve the framework silica in some regions.

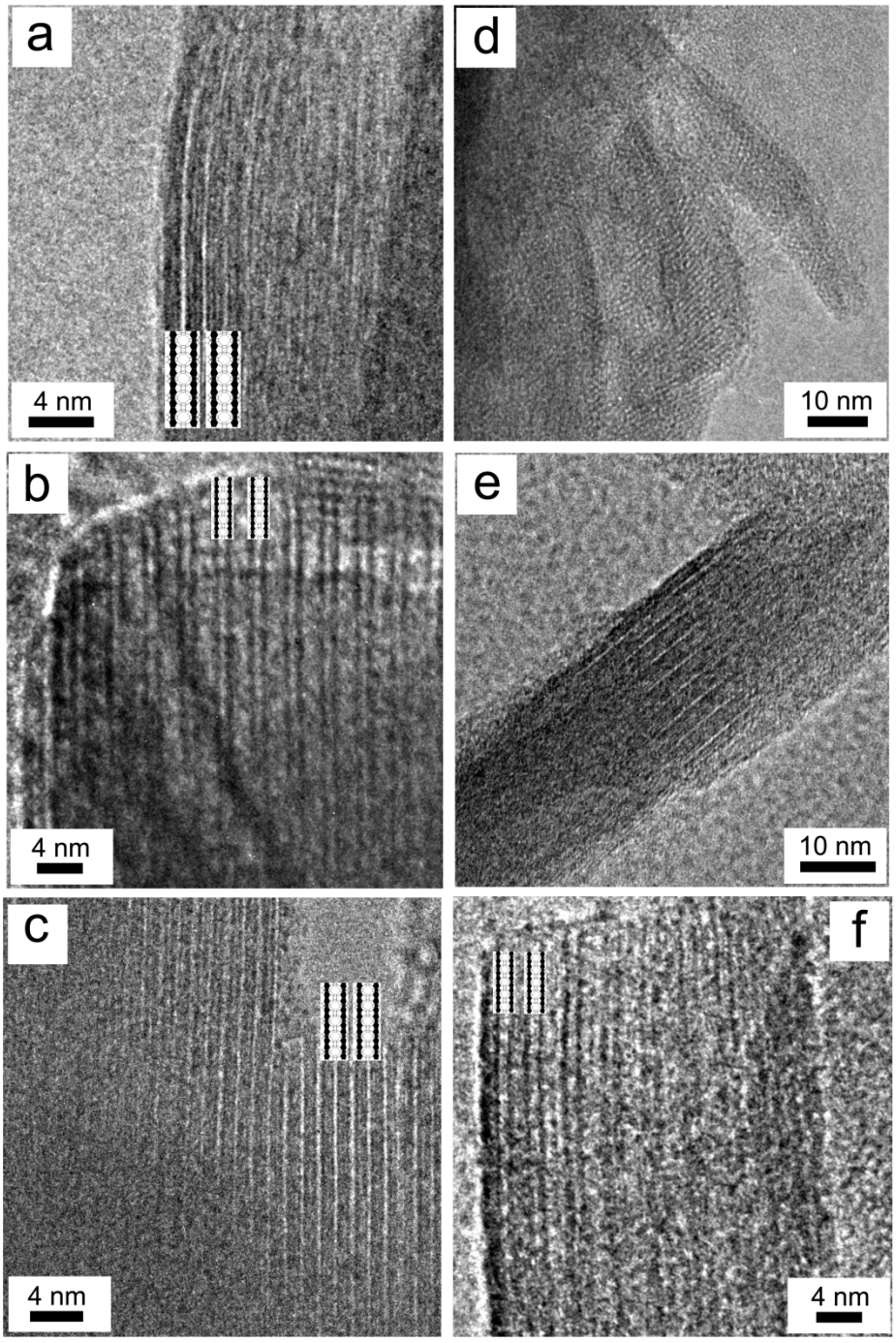

Figure 4.11. HRTEM images of a) MCM-22(P), b) MCM-22(PS-RT), c) deswollen MCM-22(P) obtained by acidification of MCM-22(PS-RT), and (d), (e), (f) MCM-22(PS-80). Schematics of single MCM-22(P) layer have been overlapped on some of the images to facilitate identification of layers.

Pillaring of swollen materials

The swollen zeolite materials can be pillared to make MCM-36 (see Figure 4.4). Figure 4.12a illustrates on XRD pattern obtained after pillaring MCM-22(PS-RT). This pattern is characteristic of a MCM-36 material with an intense low angle 001 peak at the 2θ value of 2°.[137,156,157] Remarkably, the 002 and 003 reflections are plainly visible, features that have never been reported for MCM-36 to the best of our knowledge. The presence of these reflections indicates that the material retains long range order even after pillaring. Figure 4.12b shows the pillared material obtained from MCM-22(PS-80). The XRD pattern is grossly similar to the MCM-36 analogue obtained from MCM-22(PS-RT), except that the peaks are broader and the 002 and 003 reflections are not visible indicating the absence of long range order.

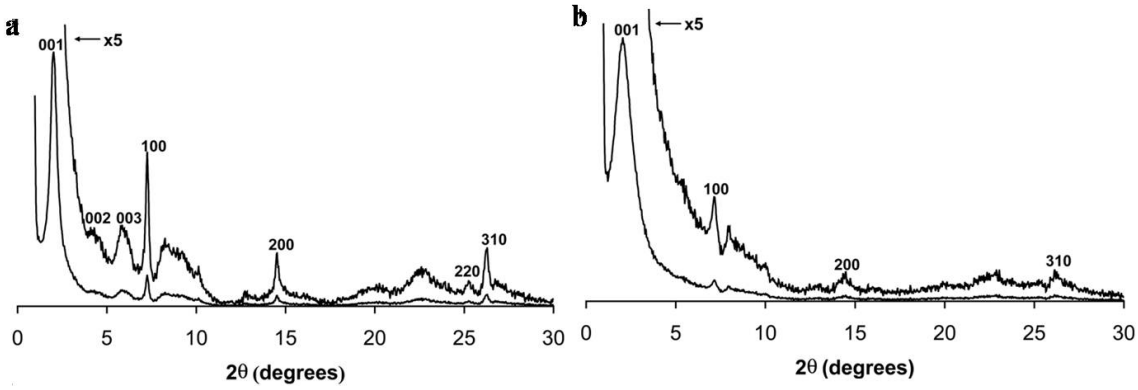

Figure 4.12. XRD pattern of MCM-36 obtained by pillaring a) MCM-22(PS-RT) and b) MCM-22(PS-80). Second curve in each figure is a 5 times magnification of lower curve for better visualization of peaks.

Figure 4.13 shows a TEM image of the MCM-36 analogue obtained by pillaring MCM-22(PS-RT). This material shows regularly spaced layers (dark lines) with an interlayer distance of l_{TEM} = 42 Å, which agrees well with the XRD value, l_{XRD} = 44 Å.

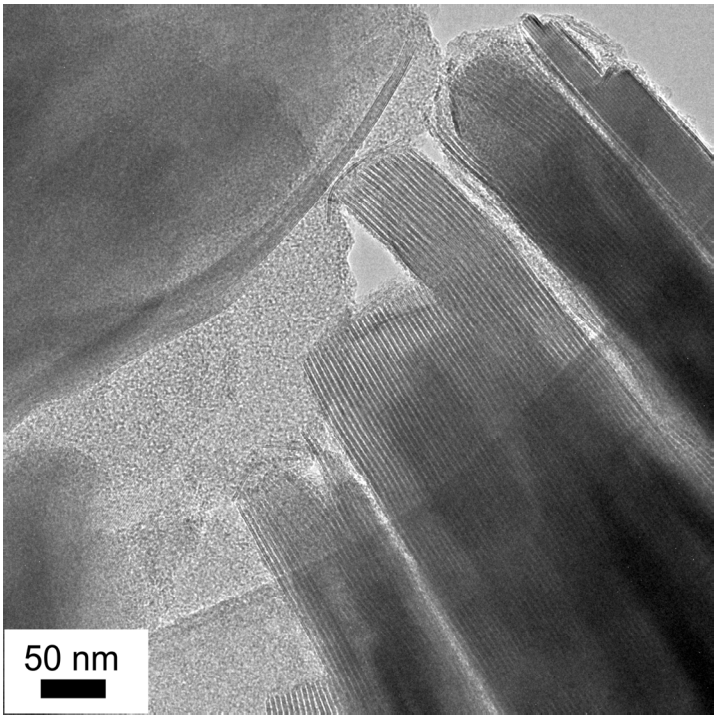

Figure 4.13. TEM micrograph showing MCM-36 analogue obtained by pillaring MCM-22(PS-RT).

Nitrogen adsorption experiments further confirm successful pillaring. Figure 4.14 shows the nitrogen adsorption/desorption curves for MCM-22 and the MCM-36 analogue obtained from MCM-22(PS-RT). For MCM-36 analogue, the increase in adsorption up to a relative pressure (P/P_0) of 0.4 clearly indicates the presence of mesoporosity created by pillaring. MCM-22, on other hand, saturates at a relative pressure of 0.1. The BET surface area of the pillared material was found to be 934 m^2/g, which is significantly higher than the value of 560 m^2/g obtained for MCM-22. These surface area values compare well with those reported in the literature[139,156] (400-500 m^2/g for MCM-22 and 800-950 m^2/g for MCM-36). The BJH pore size distribution (Figure 4.14 inset) also shows a substantial increase in mesopore volume (15-35 Å) as a result of pillaring. Successful preparation of the pillared MCM-36 material independently corroborates our conclusion regarding swelling at room temperature drawn from XRD and TEM.

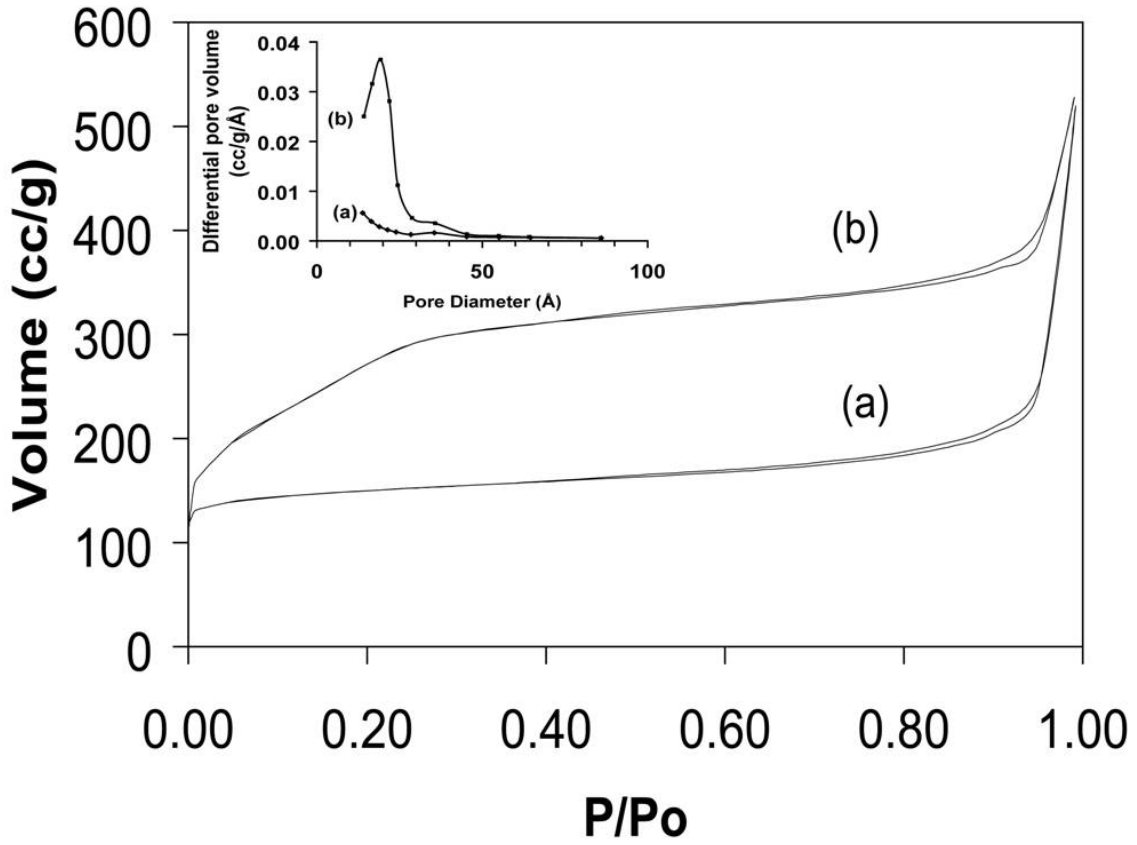

Figure 4.14. N_2 adsorption/desorption isotherm and BJH pore size distribution (Inset) of a) MCM-22 and b) MCM-36 analogue obtained by pillaring MCM-22(PS-RT).

Unlike the high temperature swollen MCM-22(P), the room temperature swollen material cannot be exfoliated simply by ultrasonication in water to produce ITQ-2.[114] This suggests that the high temperature swelling of MCM-22(P) and subsequent ultrasonication to produce ITQ-2, is essentially a fragmentation process resulting in exfoliated and other fragments. Room temperature swelling, on the other hand, results in highly ordered material, without fragmentation. The inter layer forces are still strong enough to prevent exfoliation by ultrasonication.

Polystyrene - Swollen MCM-22 Nanocomposites

Polystyrene-MCM-22(PS-RT) nanocomposites were prepared by solvent casting and melt blending techniques. For solvent casting, toluene was found to be a suitable solvent to disperse the swollen material based on the optical clarity of the dispersion. Figure 4.15 shows a TEM image obtained by drying a few drops of the toluene dispersion. A few exfoliated single layers (indicated by white arrows) are visible. The area marked by the white box on the image shows a crystal in process of exfoliation (as seen by the curving and detachment of layers). The feature from the carbon on the microscope grid has been indicated by a black arrow to distinguish it from the sample. XRD data (not shown here) indicates that solvent intercalation results in further expansion of interlayer distances and that subsequent ultrasonication results in partial exfoliation.

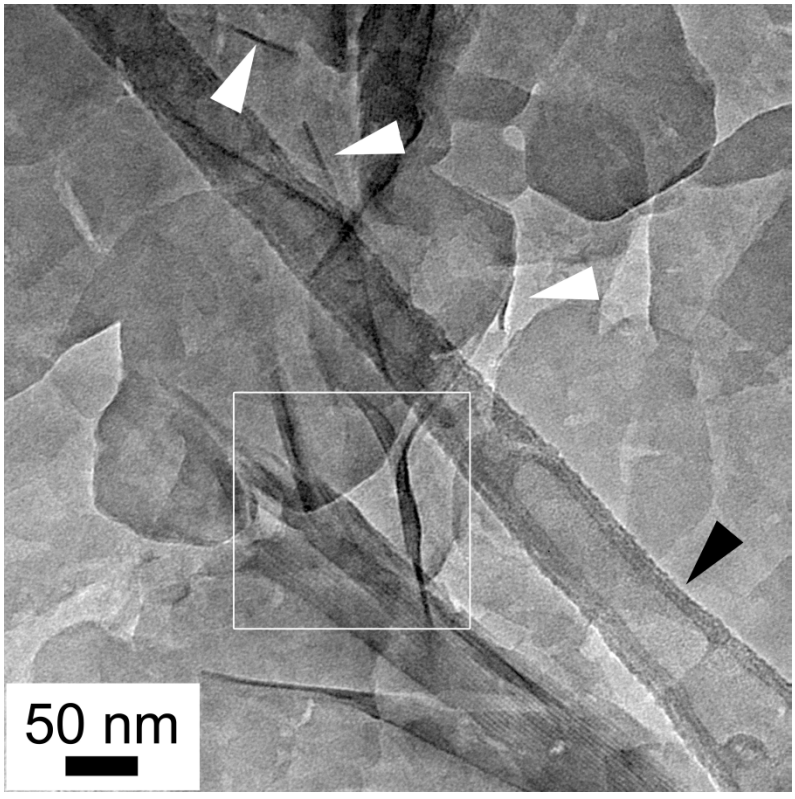

Figure 4.15. TEM image of the dispersion of MCM-22(PS-RT) in toluene. Sample was prepared by drying a few drops of dispersion onto a microscope grid.

Figure 4.16a shows a TEM micrograph of polystyrene-MCM-22(PS-RT) nanocomposite prepared from solvent casting. Many single exfoliated layers (some indicated by white arrows) can be seen along with fewer partially exfoliated and intercalated layered structures (some indicated by black arrows). Figure 4.16b shows a TEM micrograph of the nanocomposite prepared by the melt compounding technique. It shows a lot of individual exfoliated layers (some indicated by white arrows) along with a polymer-intercalated stack-of-layers (indicated by a black arrow). Apparently, the shear stress generated during the melt compounding causes the slipping of layers and eventually forces them apart.[158] These images clearly demonstrate the feasibility of the concept of polymer-exfoliated-MCM-22 nanocomposites. Further work to increase the extent of exfoliation is described in the next chapter.

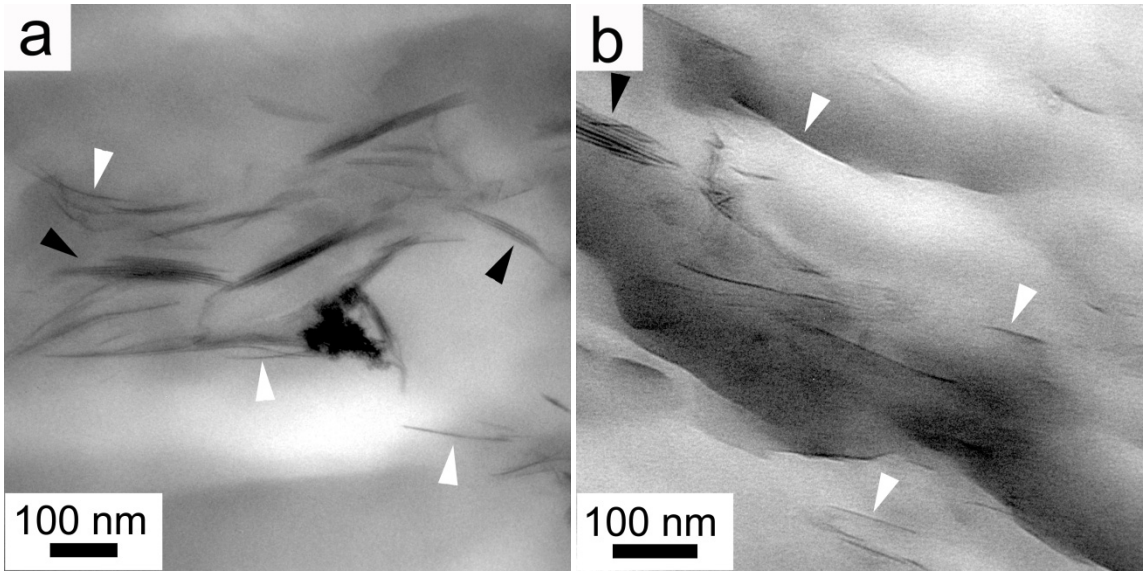

Figure 4.16. TEM micrographs of polystyrene-MCM-22(PS-RT) nanocomposite prepared by a) solvent casting and, b) melt compounding.

4.5 Summary

A procedure has been demonstrated for swelling MCM-22(P) layers without degradation of the in-plane layer morphology. MCM-22(P) can be swollen under high pH conditions at room temperature. The resulting material evolves to a highly ordered structure with increased layer spacing on repeated washings with water. The swollen

material can be successfully pillared to produce an MCM-36 analogue which retains layers with composition and structure closer to the one present in MCM-22(P). An interesting feature of the swollen material is that it can be reversibly deswollen back to MCM-22(P) by acidification. This is in contrast to the material produced by high temperature swelling process that upon acidification leads to ITQ-2 and, is attributed to the preservation of the layer structure. This swelling procedure is well suited for polymer nanocomposite and thin coating fabrication, which requires swelling of MCM-22(P) layers with retention of crystal structure to maintain the high aspect ratio of the layers. The preliminary work on polymer nanocomposites using the swollen material reveals partially exfoliated morphology of MCM-22 layers in a polymer matrix.

5. Highly Crystalline Nano-thick Porous Sheets from Exfoliation of MCM-22(P)

* To be submitted

A major problem of structural destruction during the swelling of layered zeolite precursors was subverted by judicious choice of swelling conditions, as described in Chapter-4. A melt compounding process to make polymer nanocomposite containing exfoliated MCM-22(P) sheets in polystyrene, was also mentioned briefly. Conceptually, such a process can be extended to various polymer matrices producing a variety of mixed matrix materials. However, in practice, it was realized that polymers with higher melt processing temperature (>200 ˚C) could not be used due to limited thermal stability of the surfactant used for the swelling of MCM-22(P). A large number of polymer candidates which are of interest for gas separation membranes (eg. polysulfone, polyimide, styrene-PDMS block copolymers) have higher melt processing temperature (250-300 ˚C). Melt compounding with these polymers resulted in collapse of swollen structure due to burning of surfactant (at high melt compounding temperature), preventing polymer intercalation between the layers and the exfoliation into individual sheets. This scenario has been depicted schematically in Figure 5.1. Moreover, melt compounding produces exfoliated sheets bound in polymer. Preparation of composite membranes with inorganic matrices requires exfoliated MCM-22(P) sheets free of any polymer.

In an attempt to address the above mentioned challenges, here we describe a way to obtain highly crystalline exfoliated sheets of MCM-22(P) in powder form. Swollen MCM-22(P) was exfoliated into 2.5 nm thick sheets by melt compounding with polystyrene, followed by removal of polystyrene using depolymerization step. Melt compounding parameters (viz. time and temperature) were optimized to increase the extent of exfoliation. X-ray diffraction and TEM revealed high crystallinity and plate like morphology of zeolite sheets, which is in sharp contrast to previously reported exfoliated

material, ITQ-2. The powder of exfoliated sheets can be mixed with a variety of polymer or inorganic matrices via solvent blending techniques to make mixed matrix membranes. Besides membrane applications, exfoliated sheets of MCM-22(P) can act as the building blocks for making thin oriented coatings for a variety of applications. Preliminary results on fabrication of crack-free coatings of this material on glass substrate have also been described.

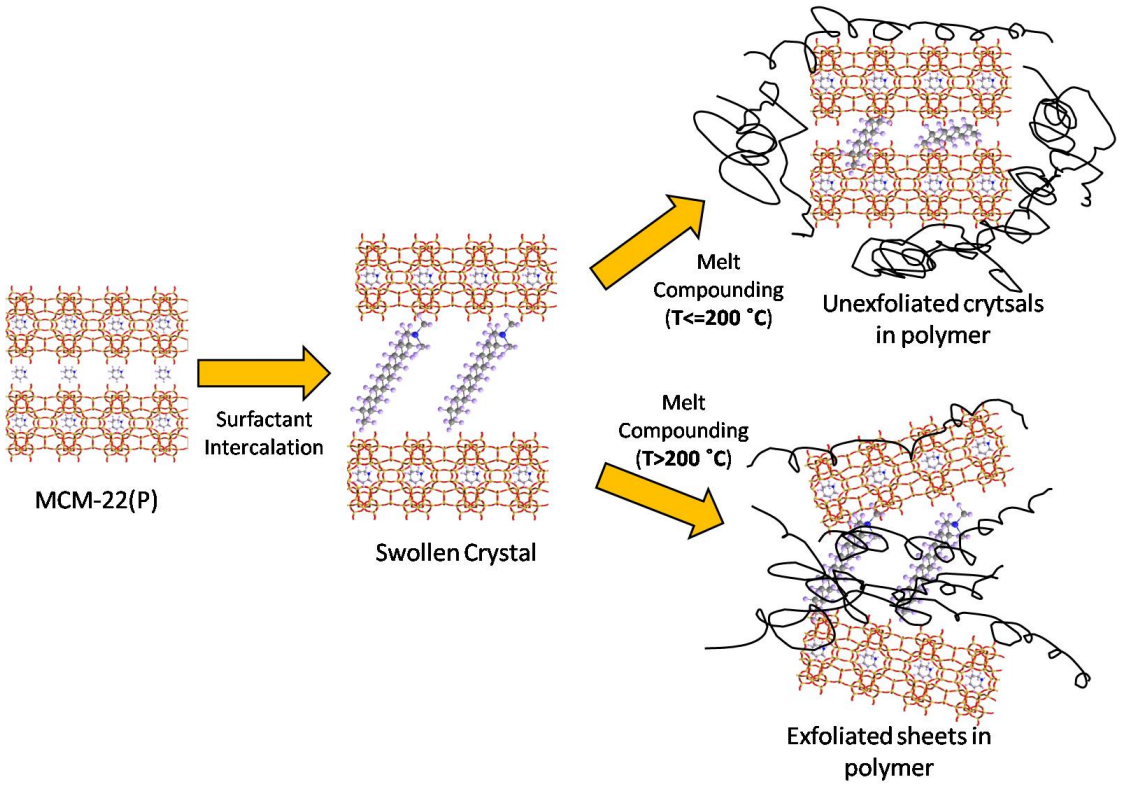

Figure 5.1. Schematic depicting the two scenarios possible on melt compounding of swollen MCM-22(P) with polymer. Melt compounding at temperature greater than 200 ˚C results in burning of surfactant and collapse of swollen structure, preventing polymer intercalation between the layers and no exfoliation. Polymers which can be melt-processed below 200 ˚C intercalate in gallery spaces and exfoliate the sheets apart.

5.1 Introduction

Nano-thick zeolite sheets derived from the exfoliation of their lamellar precursor are attractive material due to their unique functional and structural properties. These materials are often called as 'nanosheets' to represent the two-dimensional anisotropy of individual layers, typically hundreds of nanometers in lateral dimensions but only one or two nanometers in the thickness. These materials have been used as highly active catalysts[114] and additives to make polymer nanocomposites.[124] Nanosheets have the advantage over other nanomaterials due to their high aspect ratio. As such, they are currently of great interest as building blocks for the fabrication of oriented thin films for a variety of applications such as inorganic membranes for separations[132], low dielectric coatings[159], corrosion protection[160], chemical sensors[161], membrane reactors[162], etc.

MCM-22(P) is one of the several zeolite precursors which crystallizes in lamellar structure consisting of 2.5 nm thick nanosheets stacked on top of each other.[112] These nanosheets fuse together on heating to form a 3D zeolite framework, MCM-22.[112] The transport of molecules across the thickness of these nanosheets is governed by very small pores (6Member Ring, ~0.24 nm). Only hydrogen, helium and water molecules can pass through these pores.[163] As such, thin films or composites of these nanosheets can be useful for gas separation applications (e.g. H_2/CO_2). Previous attempts to exfoliate MCM-22(P) into nanosheets have resulted in significant destruction of layer structure and partial amorphitization of crystals.[114,125,126] The resultant material, designated as ITQ-2, has reduced crystallinity with partially destroyed pore structure and consists of amorphous silica impurities.[164] Although ITQ-2 is still a very active catalyst, it is not suitable for the fabrication of thin films for separation applications due to severe structural destruction during exfoliation. Preservation of structure during exfoliation remains a great challenge in several other zeolite precursors. Unlike a lot of layered silicates (e.g. clays)[165] and inorganic layered materials[166,167] which have been shown to exfoliate into thin crystalline sheets under mild chemical treatment, exfoliation of zeolite lamella often requires very harsh chemical environment (high pH, high temp, etc) which results in partial

amorphitization of crystals along with destruction of layered morphology and its pore structure.[124,127]

In this chapter, a different approach has been described to exfoliate MCM-22(P) into individual nanosheets without any structural destruction. We use melt extrusion to exfoliate MCM-22(P) in polymer followed by depolymerization of polymer to obtain highly crystalline nanosheets of MCM-22(P), as shown schematically in Figure 5.2. Further, a facile way to make films of these nanosheets on a variety of substrates has been demonstrated. To the best of our knowledge, this is one of the few instances of producing crystalline zeolite nanosheets by exfoliating a lamellar precursor without any noticeable destruction to the layer morphology and its pore structure. Some of the aspects of the procedure described here can be applied to exfoliate other layered materials.

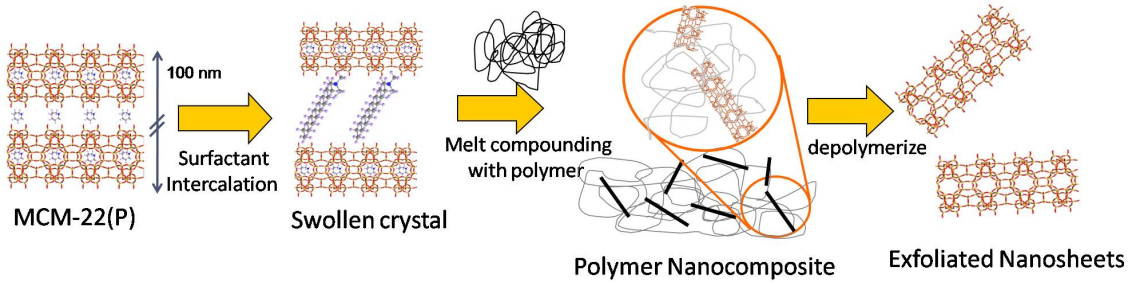

Figure 5.2. Schematic showing exfoliation process of MCM-22(P) into nanosheets as described in this work. First MCM-22(P) is swollen by surfactant intercalation to create open spaces between the layers. Then it is melt compounded with polymer to exfoliate and disperse nanosheets in polymer matrix and finally the polymer is removed by depolymerization to obtain thin zeolite nanosheets in powder form.

5.2 Experimental Section

Synthesis of MCM-22(P)

Zeolite precursor MCM-22(P) was synthesized according to procedure reported by Corma et. al.[114] Typically, 0.72 g of sodium aluminate (MP biomedicals, USA) and 2.48 g of sodium hydroxide (97+ %, Fisher) were dissolved in 311 g of distilled water.

Subsequently, 19.1 g of hexamethyleneimine (HMI) (Aldrich) and 23.6 g of fumed silica (Cab-o-sil M5) were added to the mixture. The mixture was allowed to stir for 5 h at room temperature, followed by 11 days in rotating Teflon-lined steel autoclaves at 408 K. The crystalline product obtained after 11 days was collected by centrifugation and repeatedly washed with distilled water to reduce the pH to 9. A part of the product was converted to MCM-22 by heating it to 540 ˚C for 5 hours resulting in fusion of layers to form a 3D framework.

Swelling of MCM-22(P)

Next step involved swelling of MCM-22(P) by intercalation of cetyltrimethyl ammonium bromide (CTAB) in presence of tetrapropyl ammonium hydroxide (TPAOH), according to the procedure reported in our previous publication.[164] Briefly, 9.0 g of aqueous slurry of MCM-22-(P) (20 wt % solids) was mixed with 35.0 g of an aqueous solution of 29 wt % CTAB (Aldrich) and 11.0 g of an aqueous solution of 40 wt% TPAOH (Alfa Aesar). The mixture was allowed to stir for 16 h at room temperature, after which the particles were recovered by repeated cycles of centrifugation (10 min centrifugation at 10000 rpm, and redispersion in fresh water). As discussed in chapter-4, swelling at room temperature was the key to avoid structural destruction of MCM-22(P) during this procedure.

Exfoliation of swollen MCM-22(P) via melt compounding

Swollen MCM-22(P) was exfoliated into nanosheets by melt compounding with polymer (polystyrene, Mw = 45000, Aldrich). Melt compounding was done using a DACA Mini Compounder vertical, co-rotating twin screw extruder with a recirculation channel. For melt compounding, 0.16 g of swollen MCM-22(P) and 3.84 g of polymer were fed to melt compounder and mixed together at desired set of temperatures for certain amount of time. After completion of mixing, the composite material was extruded out through a cylindrical die.

Extraction of zeolite sheets from polymer

Exfoliated nanosheets were extracted out of composite by depolymerization of polymer followed by calcination. The material obtained after melt compounding was heated to 350 ˚C to depolymerize polystyrene into styrene, which boils off. After complete removal of styrene, the residue was heated to 540 ˚C for 5 hrs to burn off the remaining organic matter, leaving behind zeolite nanosheets in powder form.

Coatings of zeolite sheets

Coatings of nanosheets on glass slides were made using a convective assembly apparatus as described elsewhere.[168] The apparatus was designed to withdraw substrate from a static coating sol at a controlled rate and under a prescribed flow of dry nitrogen. The coating sol was prepared by adding zeolite nanosheets in water (0.5 wt%), sonicating the mixture for 1 h, followed by leaving the mixture undisturbed for 16 h to allow big agglomerates to settle down. The supernatant dispersion was used for making coatings. The substrate was withdrawn at a desired rate and nitrogen flowrate was kept constant at 3 SCFH.

Characterization Methods

Powder X-ray diffraction (XRD) patterns were collected on a Bruker AXS D5005 diffractometer using Cu-Kα radiation. Data were collected in the 2θ range from 1° to 30° with a step size of 0.04° and a step time of 3 s.

All NMR spectra were recorded at a field of 11.7 T (BRUKER Avance 500). ^{29}Si MAS NMR spectra were recorded at 99.37 MHz using 4 mm rotors at a spinning speed of 8 kHz, a dwell time of 16.65 μs, a π/2 pulse of 4.0 μs and a recycle delay of 60 s. All spectra were referenced with respect to tetramethylsilane (0 ppm). ^{27}Al MAS NMR spectra were recorded at 130.34 MHz using 4 mm rotors at 14 kHz spinning speed, a dwell time of 0.5 μs, a selective π/18 pulse of 0.3 μs and a recycle delay of 0.1 s. An aqueous solution of aluminum sulfate (0.1 M) was used as the reference (0 ppm).

A FEI Tecnai G2 F30 transmission electron microscope (TEM) equipped with a charge couple device (CCD) and operated at 300 kV was used for direct imaging of various samples. For imaging of zeolite powders, samples were prepared by dispersing powders in water and placing a few drops of dispersion onto a carbon coated copper grid followed by air drying to evaporate off water. For imaging of zeolite nanosheets dispersed in polymer nanocomposite, 50-80 nm thick slices of composite material were obtained using a Reichert Ultracut S Ultramicrotome equipped with a diamond knife.

The coatings of zeolite nanosheets on glass substrates were examined by scanning electron microscopy (SEM, JEOL 6500) operating at an accelerating voltage of 5 kV. Samples were sputtered with platinum (50 Å thickness) before imaging.

5.3 Results and Discussion

Preservation of crystallinity and layered morphology during exfoliation requires a careful choice of chemical environment and processing conditions. Corma et. al.[114] exfoliated MCM-22(P) to make ITQ-2 by first swelling the crystals via surfactant intercalation at high pH and high temperature followed by sonication to force apart the layers. It has been shown in several subsequent works[125,126,143] including ours[164] that significant destruction happens both at swelling as well as sonication step. The silica content of the material reduces considerably due to partial dissolution of precursor under high pH + high temperature conditions during swelling. Thus, the resulting ITQ-2 material consists of a mixture of amorphous silica with some crystalline fragmented nanosheets of MCM-22(P).

In chapter-4, a way to prevent crystal destruction during swelling process by reducing the temperature of swelling was demonstrated. The resulting swollen material retained the overall morphology of precursor material and had highly ordered stacking of nanosheets. However, subsequent sonication did not result in exfoliation of swollen crystal, probably due to ordered stacking which resulted in strong interlayer forces and kept the nanosheets together.

Melt compounding with polystyrene was used to exfoliate the swollen material into individual nanosheets. The combined effect of shear forces generated by rotating screws and diffusion of polymer chains in the interlayer spaces between nanosheets, results in exfoliation of swollen crystal.[158] Temperature and time of mixing are the two key parameters which influence the extent of exfoliation for a given polymer.[169] Screening experiments (not shown) with various temperatures and time of mixing were conducted to figure out the optimal conditions for exfoliation. Quantification of exfoliation was made by counting the exfoliated nanosheets and unexfoliated crystals in TEM images of melt compounded samples. Screening experiments led to selection of following condition for melt compounding: 120 ˚C (20 min) +170 ˚C (20 min) +150 ˚C (20 min) + 200 ˚C (20 min). The rationale behind going up and down in temperature was to access both high shear force regime (at low temp) and high polymer diffusion regime (at high temperature). About 70% of the crystals were completely exfoliated under these conditions. A TEM micrograph of melt compounded sample is shown in Figure 5.3. The exfoliated nanosheets are oriented along their edges and appear as black lines (indicated by black arrows) dispersed in gray polystyrene matrix. Some unexfoliated crystals (appear as closely spaced dark lines, indicated by white arrow) are also visible in the micrograph. Neverthless, a majority of crystals are exfoliated and the unexfoliated crystals are only 3-4 layers thick.

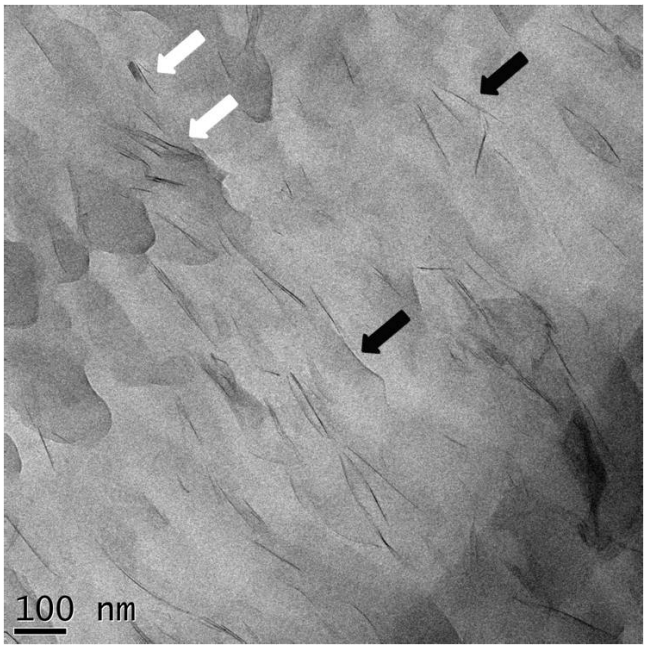

Figure 5.3. TEM image of polystyrene-MCM-22(P) nanocomposite obtained by melt compounding. A majority of crystals are exfoliated to single nanosheets (some indicated by black arrows). However, some unexfoliated crystals are also visible (indicated by white arrow).

Usage of these nanosheets as building blocks for making inorganic membranes, low dielectic coatings, etc, requires obtaining them free of polymer. Polystyrene has a ceiling temperature of 310 ˚C[57], above which it is thermodynamically unstable and spontaneously depolymerizes to styrene. Polystyrene/nanosheets composite material was heated to 350 ˚C under vacuum to initiate depolymerization. Vapors of styrene can be seen evolving during this process. Vacuum is necessary to prevent spurious oxidation of polystyrene. After complete removal of polystyrene (as inferred from no further evolution of styrene vapors), the remaining organic residue were burned off by heating the contents to 540 ˚C under an air flow (150 cc/min) to obtain nanosheets of MCM-22(P) in powder form. Figure 5.4a shows a low magnification TEM image of nanosheets obtained after this process. A lot of plate-like particles (lying flat on TEM grid) are clearly visible. Low contrast in TEM image is suggestive of very thin plates. Due to their high aspect ratio, the edges of these nanosheets often curl up and appear as thin dark line in TEM images. Some of the nanosheets aggregate during the depolymerization process (as indicated by

white arrow in Figure 5.4a). Figure 5.4b shows a high resolution TEM image of nanosheets. The highly crystalline nature of nanosheets is plainly visible as seen by the presence of lattice fringes. The dark lines in this image are edges of nanosheets which curl up and reveal the pore structure within the layer. Each of these edges is 2.5 nm in thickness, which confirms single exfoliated nanosheet. To the best of our knowledge, such thin and highly crystalline sheets of a zeolitic material have never been reported before.

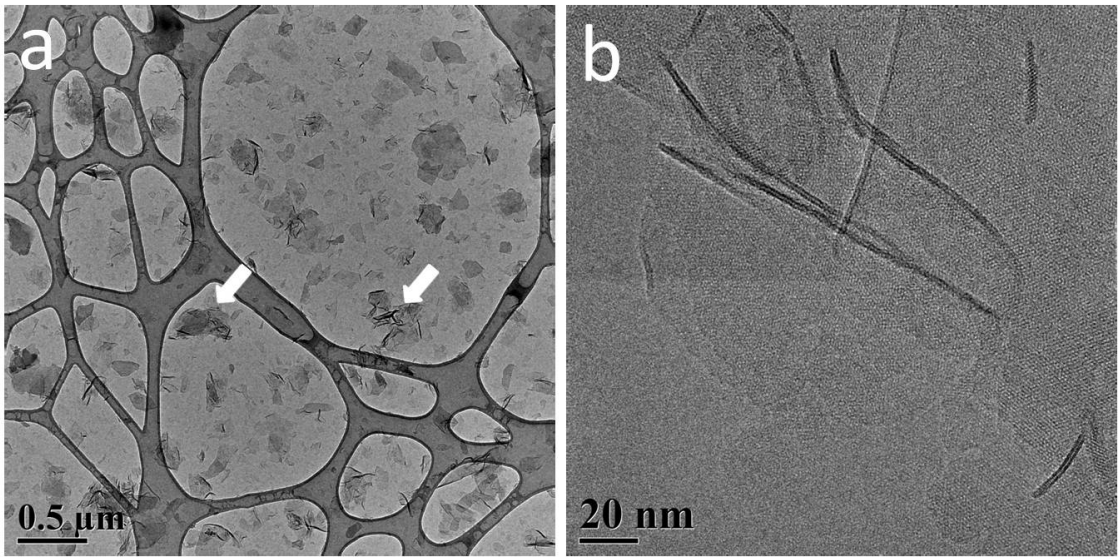

Figure 5.4. TEM micrographs of nanosheets of MCM-22(P) obtained by removal of polymer via depolymerization at a) low magnification and b) high resolution.

Comparative images of ITQ-2, shown in Figure 5.5, reveal the structural destruction and partial amorphitization of material. As clearly visible in Figure 5.5a, the layered morphology of the material is significantly destroyed. It consists of big amorphous looking agglomerates of irregular shape. ITQ-2 does consist of a few exfoliated nanosheets, as indicated by white arrows in Figure 5.5b. However, a majority of material surrounding these nanosheets appears to be amorphous, highly fragmented and partially destroyed. The amorphitization of material is further evidenced in Figure 5.5c, where a part of the material (outlined by white square) shows weak lattice fringes indicative of crystallinity in the sample, but the rest of it looks amorphous in TEM.

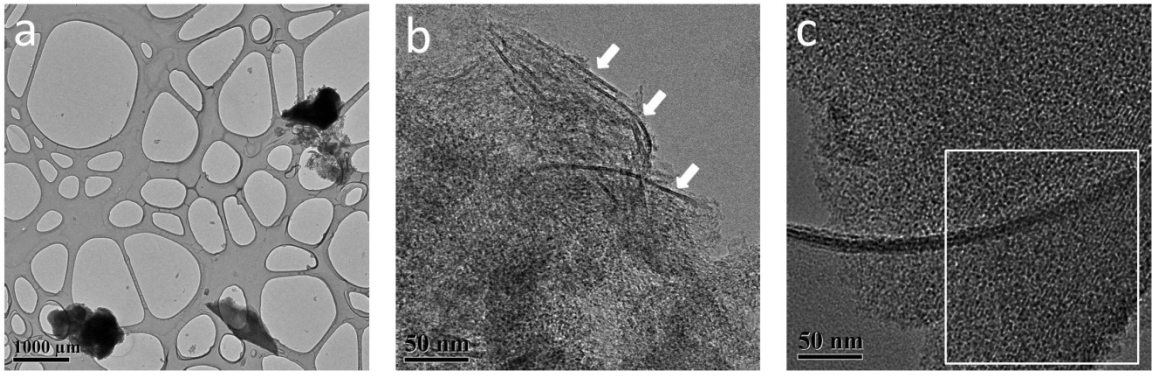

Figure 5.5. TEM micrographs of ITQ-2 at a) low magnification and b), c) high resolution.

Thus, it is clear from TEM micrographs than nanosheets produced in this work are significantly different than ITQ-2 in terms of morphology and crystallinity and should be treated as a different material.

Figure 5.6 shows the XRD pattern of MCM-22, crystalline nanosheets obtained by melt compounding and ITQ-2. The diffraction pattern of MCM-22 consists of sharp well resolved peaks indicative of a 3D crystalline material and is in agreement with the literature.[112] The XRD pattern of nanosheets shows broader and less intense peaks in general, which is a direct consequence of exfoliation. The 001 reflection (around $2\theta = 3^{\circ}$) disappears on going from MCM-22 to nanosheets, indicating loss of periodicity in c-direction. The c-axis is along the stacking direction of nanosheets. Exfoliation results in individual nanosheets which are out of registry with each other, thereby resulting in loss of periodicity and disappearance of 001 reflection. A complete disappearance of 001 peak suggests predominantly exfoliated material. ITQ-2, on the other hand, shows almost a featureless diffraction pattern with very broad and barely resolved reflections. This is indicative of severe destruction and fragmentation during the swelling and sonication process used to make this material and corroborates well with the TEM images shown in Figure 5.5.

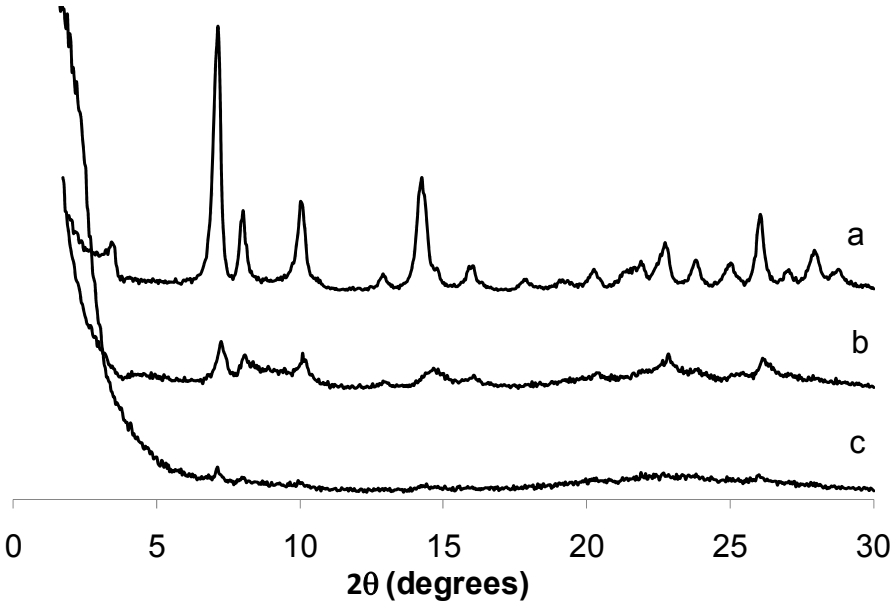

Figure 5.6. XRD patterns of a) MCM-22, b) Exfoliated nanosheets, c) ITQ-2. The patterns have been shifted vertically for the sake of clarity.

Solid-state ^{29}Si NMR was employed to investigate the structural changes and coordination environment as a result of exfoliation of MCM-22(P) into nanosheets. Figure 5.7 and 5.8 show the ^{29}Si MAS NMR and ^{29}Si CPMAS NMR spectra respectively of exfoliated nanosheets and ITQ-2. The resonances in the region of -104ppm to -120ppm are associated with Q^4 species[144,145], while -100 ppm resonance is associated with Q^3 or Si(1Al) species[153] (Q_n stands for $X_{4-n}Si[OSi]_n$, X = OH or O^-). Q^2 species resonate around -90 ppm. For both the materials, the intensity of -100ppm peak increases considerably as we go into cross polarization (CP) mode. Q^3 and Q^2 species are more rapidly polarized than Q^4 species in CP mode due to their close proximity to silanol groups.[155] Thus, an enhancement of -100ppm peak in CP mode is indicative of the fact that major contribution to this resonance is due to Q^3 species (and not Si(1Al) species). Based on the structure of MCM-22 unit-cell and the Si/Al ratio of the starting MCM-22(P) material, the ratio of Q^3/Q^4 should be ~1:16 in both nanosheets as well as ITQ-2. Thus, the ^{29}Si NMR spectra for these materials should be dominated by Q^4 resonances and Q^3 resonance should be of very low intensity. However, as clearly visible in Figure 6, an ITQ-2 spectrum shows a very intense Q^3 resonance around -100ppm, indicating much

greater amount of Q^3 species than predicted. These extra Q^3 species were probably created by breaking of bonds during production of ITQ-2 (each bond breaking around Q^4 results in two new Q^3 species) and provide credibility to our hypothesis that significant structural destruction accompanies ITQ-2 production. On the other hand, nanosheets produced by our method do not show a strong Q^3 signal in the ^{29}Si NMR spectra. The Q^3 species become visible only in the CP mode as shown in Figure 7. Thus, our exfoliation method preserves the local bonding environment in a much better fashion as compared to the one used for ITQ-2 production.

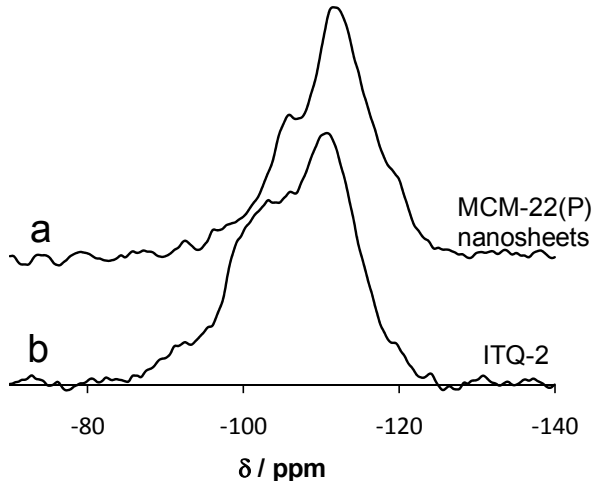

Figure 5.7. ^{29}Si MAS NMR of a) exfoliated nanosheets and b) ITQ-2.

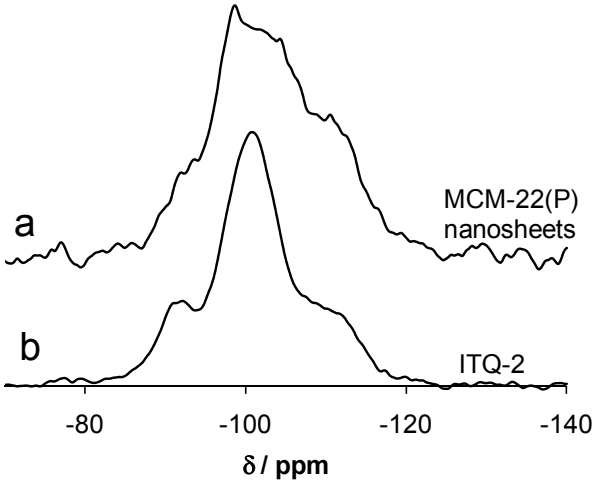

Figure 5.8. ^{29}Si CPMAS NMR of a) exfoliated nanosheets and b) ITQ-2.

The crystalline zeolitic nanosheets produced in this work can be useful for a variety of applications, such as polymer nanocomposites, inorganic films for gas separations, low dielectric coatings, etc. To realize some of these applications, it is required to make thin films of these materials on a suitable support. In order to demonstrate the feasibility of film fabrication, a convective assembly coating technique was used to make thin films of these nanosheets on a glass substrate. The substrate was withdrawn from a dispersion of nanosheets in water. The thin film of water formed on moving glass substrate was dried by a laminar flow of nitrogen gas to yield supported zeolite films. Care was taken to avoid agglomerates and unexfoliated MCM-22(P) crystals by allowing them to settle down and using the supernatant dispersion for fabrication of films. A substrate withdrawal rate of 2 cm/hr was found to yield thin, continuous defect free film. SEM images of these films are shown in Figure 5.9. The low magnification SEM image of the top view of the film (Figure 5.9a) shows defect free coating across several hundred microns. The high magnification image (Figure 5.9b) shows that nanosheets tend to oriented themselves with their flat face against the substrate. The films have a thickness of about 700 nm as seen in cross-section SEM image in Figure 5.9c. Preferred orientation of nanosheets is also apparent in cross-section image, where edges of individual nanosheets are visible. Such an orientation is very important for separation applications. With this orientation, the transport of gases across the film is limited by 6MR pores within the nanosheets. Only small molecules like hydrogen and helium can pass through these pores. As such, replication of these films on a porous support can provide a high-temperature hydrogen separation membrane.

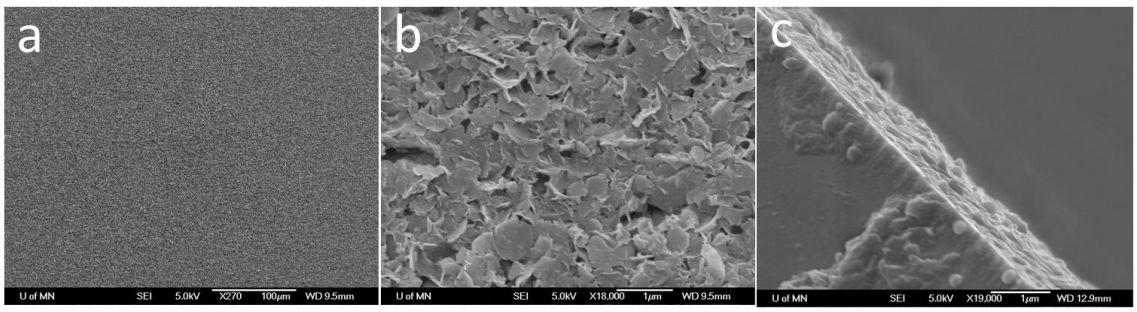

Figure 5.9. SEM images of coatings of nanosheets on a glass substrate at a) low magnification, b) high magnification and c) cross-section of coating.

5.4 Summary

Highly crystalline nanosheets of zeolite precursor MCM-22(P) with high aspect ratio were produced by exfoliating the precursor with the aid of polymer melt compounding and subsequently removing the polymer by depolymerization. For the first time, a zeolite precursor has been exfoliated without any significant destruction to its pore structure and layered morphology. The XRD indicated successful exfoliation as seen by absence of 001 peak. TEM images indicate that a majority of sample consists of very thin nanosheets with very high crystallinity. ^{29}Si NMR indicates that exfoliation proceeds with minimal structural changes to local Si-O-Si coordination. The problem of structural destruction and amorphitization of crystals during exfoliation process, as observed in ITQ-2 production have been avoided by judicious choice of processing conditions. Thin films of nanosheets with preferred orientation have been prepared on glass substrates. We believe that these nanosheets will be useful for fabrication of high-temperature hydrogen separation membranes and may show some interesting catalytic properties due to better structural preservation as compared to ITQ-2.

6. Conclusions and Future Directions

Despite the numerous efforts in the last decade to develop mixed matrix membranes with improved performance, their success remains limited. One of the important limiting factor is the use of the molecular sieves with large crystal sizes (~ few micron), which prevents their integration into existing membrane technology. Also, relatively few polymeric candidates have been explored as continuous phase of mixed matrix membranes. The literature lacks systematic investigation to identify the right matrix candidate to optimize the overall membrane performance. The research presented in this thesis addresses these material challenges and aims to provide polymeric and molecular sieve materials that can advance the development of mixed matrix membranes for gas separation applications. The advances made in this work can be broadly divided into two categories. First part involved developing block copolymers for matrix of polymer-zeolite composite membranes. Second part involved developing thin zeolite layers which can be used as selective phase in both organic (polymeric) as well as inorganic membranes.

6.1 Block copolymers for matrix of composite membranes

In this thesis, block copolymers of polystyrene (PS) and polydimethylsiloxane (PDMS) were synthesized which can be useful as the matrix phase of polymer-zeolite composite membranes. These block copolymers are attractive as they combine the high permeability of PDMS with the high elastic modulus of PS to provide a high permeability matrix with reasonable strength. PS-PDMS diblock copolymers and PS-PDMS-PS triblock copolymers with lamellar microstructure were made using anionic polymerization route. The diblock copolymers were found to be very brittle but triblock copolymers with M_n ~140000 were suitably tough to be casted into free standing films. Permeability of solvent casted films of triblock copolymers for various gases was found to be at least an order of magnitude higher than commercial membrane polymers (for e.g. polysulfone). This material has never been used for membrane applications and its

combination with selective zeolite layers can provide a composite membrane with high selectivity and high permeability.

The PS-PDMS-PS triblock copolymers were catalytically hydrogenated for the first time to PCHE-PDMS-PCHE polymers (PCHE stands for polycyclohexylethylene). The hydrogenation reaction proceeded without polymer chain degradation, which allowed us to study the mixing thermodynamics of PCHE and PDMS. This material showed interesting properties (viz. strong segregation strength between PCHE and PDMS), which were contrary to previous understanding. Both PCHE and PDMS have good thermal, oxidative and radiation stability due to the absence of the double bonds. Thus, block copolymers of PCHE and PDMS may find some interesting applications in the future, including as a matrix of composite membrane.

6.2 Thin sheets of MCM-22(P) as selective phase of composite membranes

Zeolite MCM-22(P) was exfoliated into 2.5 nm thick individual nanosheets by a three step process. First the MCM-22(P) crystal was swollen by intercalation of surfactant in between the layers. This was followed by exfoliation of swollen crystals in polymer via melt compounding techniques and finally the removal of polymer to obtain thin sheets in powder form. One of the major advances was remarkable preservation of layered morphology and pore structure of zeolite during the swelling and the exfoliation process. The resulting material consist of high aspect ratio (>40) thin crystalline sheets of zeolite, which can act as building blocks to fabricate the composite membranes for hydrogen separation.

A series of characterization methods like X-ray diffraction, NMR and electron microscopy were employed to compare the swollen and exfoliated MCM-22(P) produced in this work to the ones in literature. It was found that our method not only preserves the overall morphology and pore structure of the zeolite layers, but also the local bonding environment of silicon tetrahedral in a much better fashion than previously published procedures.

A polymer nanocomposite consisting of the exfoliated MCM-22(P) layers dispersed in a polystyrene matrix was prepared by the melt compounding techniques. Although, polystyrene is not attractive for membrane applications but an extension of this approach to other polymer matrices can provide a facile process to make polymer-layered zeolite composite membranes. Moreover, the melt compounding process is very attractive from an industrial perspective as it is scalable, continuous, efficient and environmental friendly as compared to the solvent blending approaches.

6.3 Future directions

6.3.1 Systematic permeability variation to identify the right polymer matrix

It was briefly discussed in chapter 1 and chapter 2 that optimization of the gas separation properties of mixed matrix membranes requires a balance between the gas permeability of the matrix and that of the selective zeolite phase.[14,40] Gas permeability values of zeolites are difficult to obtain accurately as the formation of defect-free pure zeolite film poses a great challenge. A more convenient way to approach this problem is by investigating the gas separation performance of mixed matrix membranes made by combining a zeolite candidate with different polymer matrices with systematically varying gas permeability values. This was the motivation to develop block copolymers for matrix phase in this work. Block copolymers can allow permeability variation over several orders of magnitude by choosing suitable blocks. Within a block copolymer system, fine tuning can be done by varying the relative composition of constituent blocks. This path could not be pursued in present work due to lack of procedures to produce nanometer-thin zeolite layers at the start of this work. However, a way to produce thin sheets of MCM-22(P) has been demonstrate in this work. A study using these zeolite layers with block copolymers is feasible in the future. PS-PDMS-PS or PCHE-PDMS-PCHE triblock copolymers may prove a good starting material for such a study.

6.3.2 Polymer-exfoliated zeolite mixed matrix membranes by melt compounding

In chapter 3 and 4, we demonstrated a polymer nanocomposite with exfoliated MCM-22(P) layers dispersed in polystyrene matrix, prepared via melt compounding

process. Melt compounding is a very simple yet efficient procedure to make polymer nanocomposites with exfoliated layered materials. It has been used successfully for a variety of layered materials in various polymer matrices.[169-173] Melt compounding of swollen MCM-22(P) with other polymer matrices can provide a convenient one-step procedure to prepare mixed matrix material with exfoliated zeolite layers. Such a procedure can eliminate the depolymerization step to obtain zeolite sheets in powder form, which result in some re-aggregation. However, the polymers should be processable below 200 ˚C due to limited thermal stability of surfactant used for MCM-22(P) swelling. Reducing the processing temperature of polymers by means of suitable additives (high boiling point solvents, supercritical CO_2[174], plasticizers) can serve the trick. For example, small amounts of high boiling solvents can swell the polymer and reduce its processing temperature. After processing these solvent impregnated polymers with swollen MCM-22(P) to exfoliate and disperse zeolite layers, the solvent can be evaporated off from the nanocomposite. This approach appears promising and may provide a quick one-step method to produce mixed matrix materials.

6.3.3 Polymer-exfoliated zeolite mixed matrix membranes via solvent casting

Solvent casting is the most popular way to make mixed matrix membranes. Polymer solution and zeolite dispersions in a suitable solvent are mixed together, followed by casting and solvent evaporation to obtain mixed-matrix membranes. Suitable methods such as sonication and polymer priming are often used to uniformly disperse the zeolite materials.[9,175] Choice of solvent play an important role as its interaction with zeolite and polymer as well as its volatility influences the final microstructure of mixed matrix membrane.[9,176]

Mixed matrix membranes can be prepared by combining exfoliated MCM-22(P) sheets described in chapter 5 with a variety of polymer candidates via solvent casting techniques. Polymers which are not melt-processable can be easily dissolved in suitable solvent and mixed with a dispersion of exfoliated MCM-22(P) sheets. Some of the agglomerates produced by reaggregation of zeolite sheets during depolymerization can be

broken down by sonication step. Remaining agglomerates can be avoided by allowing the zeolite dispersion to settle for some time and using only the supernatant dispersion.

6.3.4 Temperature-pH-time study of MCM-22(P) swelling

Corma et. al.[114] swelled and exfoliated MCM-22(P) at a pH~13.8 and a temperature of 80 ˚C. However, the resultant materials had severe structural destruction, mainly due to the dissolution of framework silica at high pH + high temperature combination. In chapter 4, we demonstrated that by simply reducing the temperature, this structural destruction could be avoided. However, unlike the previous studies, swollen material could not be exfoliated by sonication and required melt processing to exfoliate it. This is presumably due to the highly ordered nature and strong interlayer forces of our swollen material. Keeping the pH constant, we explored the temperature range from room temperature to 80 ˚C. It was found that the samples swollen above 55˚C can be exfoliated by sonication but the samples swollen below 55˚C cannot be exfoliated. No detailed investigations were carried out to characterize the structural integrity of the sample swollen at 55 ˚C, but it is expected to have structural destruction intermediate between the materials swollen at 80 ˚C and room temperature. Temperature is only one of the variables which determine the extent of structural destruction. pH and time of swelling are the other two important parameters. A reduction in pH and time of swelling should also reduce the structural destruction in swollen MCM-22(P). However, too low pH and/or less time may result in incomplete or no swelling. A careful investigation with various combinations of pH, time and temperature can provide a window for swelling MCM-22(P). Within this window, it may be possible to identify the set of conditions under which MCM-22(P) can be swollen and exfoliated via sonication with minimal structural destruction. This will eliminate the time consuming process of melt compounding + depolymerization to obtain exfoliated nanosheets of MCM-22(P). A recent publication[177] presents such investigation to a limited extent but no microscopy data was presented to assess the structural destruction in various samples swollen and exfoliated under different conditions.

6.3.5 High-temperature, high-pressure inorganic membranes for hydrogen separation

Environmental concerns linked to increasing levels of green house gases, has lead to demands for cleaner technologies to produce electricity from coal without the release of CO_2 to the atmosphere. An important part of such technologies will be the pre-combustion capture of CO_2 from turbine fuel feed (mainly H_2 and CO_2) of coal based gasification plants. A membrane which can carry out H_2/CO_2 separation at high temperature (~400 ˚C) and high pressure (~2000 psi) is very attractive for this purpose.

Mixed matrix membranes of mesoporous silica matrix and ~100 nm thick MCM-22 crystals were fabricated in Tsapatsis group, which showed promising properties for H_2/CO_2 separation.[132,133] These membranes were made by depositing alternate layers of MCM-22 crystals and mesoporous silica on a flat alumina support. The inorganic nature of membranes makes them suitable for high temperature operation. Replacing 100 nm thick MCM-22 crystals by 2.5 nm thick exfoliated sheets produced in this work (Chapter 5) should further improve the performance of these membranes. Significant improvements in permeability and selectivity are expected by such a replacement due to the faster transport of hydrogen through the thin zeolite sheets and increased tortuosity for CO_2 due to the closer packing of these sheets.

Attempts were made to build mesoporous silica/exfoliated sheets mixed matrix membranes on porous tubular supports (Figure 6.1a). Alternate layers of zeolite sheets and mesoporous silica were built by sequential dip coating from an aqueous dispersion of zeolite and a silica sol[132] respectively. SEM images of resulting membrane after one and three deposition cycles have been shown in Figure 6.1 (each cycle consists of a layer of silica and a layer of zeolite sheets). A good coverage of zeolite layers were obtained as seen in the SEM images. A few uncovered areas were visible after first deposition cycle (highlighted by white circles iin Figure 6.1d). However, no uncovered area can be seen after third deposition cycle. The membranes were not selective for gas separation after three deposition cycles, presumably due to pinholes and defects which could not be seen

in the SEM images. However, the dip-coating approach appears promising, as seen by uniform coverage of support surface. Further work, directed towards optimization of the process and deposition of more bilayers, can eliminate the defects and provide a high temperature-high pressure hydrogen selective membrane.

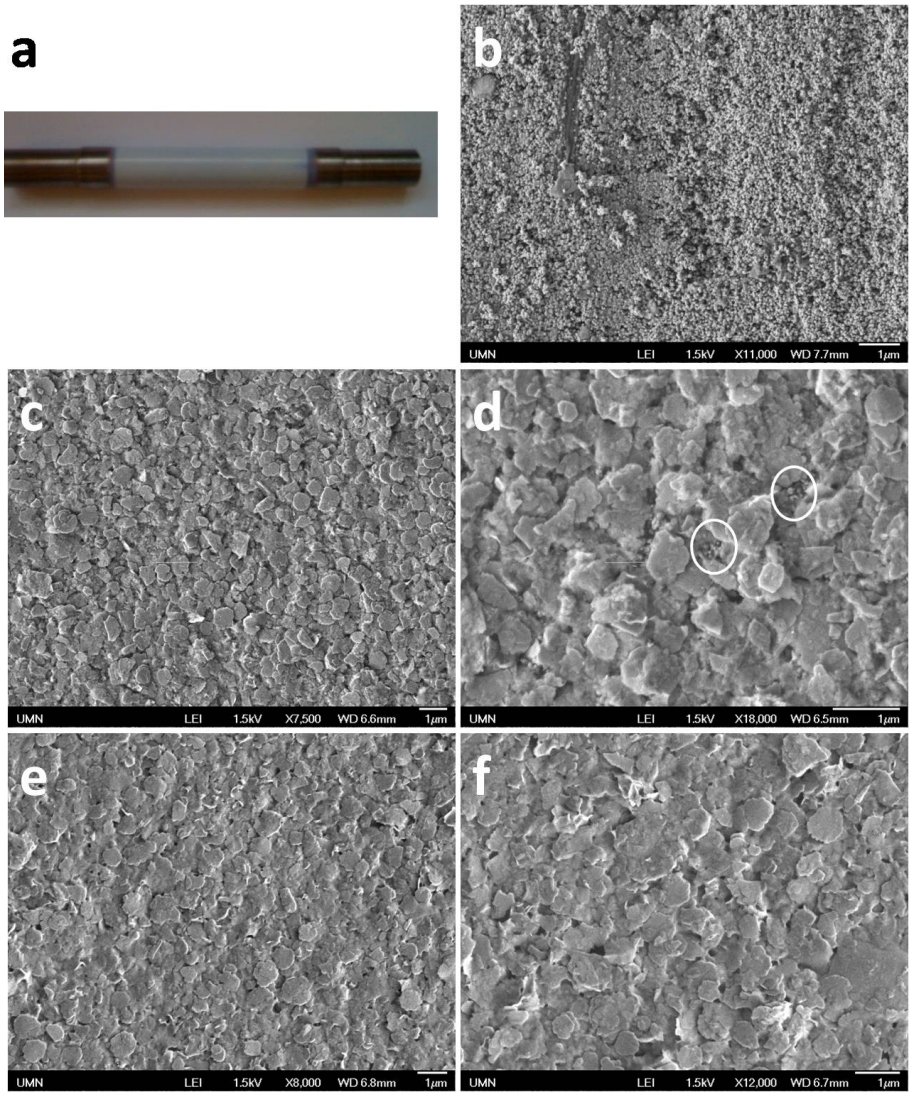

Figure 6.1. a) Optical image of porous zirconia/stainless steel tubular support, b) SEM image of zirconia support layer. Low and high magnification SEM images of film of mesoporous silica/exfoliated MCM layers on top of zirconia layer after one cycle (c, d) and three cycles (e, f). White circles in image d highlight areas not covered with exfoliated MCM-22(P) sheets and show the underlying zirconia layer. No such areas are visible after three deposition cycles.

Bibliography

(1) Toshima, N. *Polymers for Gas Separations*; VCH: New York, 1992.

(2) Prasad, R.; Notaro, F.; Thompson, D. R. *Journal of Membrane Science* **1994**, *94*, 225-248.

(3) Baker, R. W. *Industrial & Engineering Chemistry Research* **2002**, *41*, 1393-1411.

(4) Loeb, S.; Sourirajan, S. *Advances in Chemistry Series* **1963**, *38*, 117-32.

(5) Robeson, L. M. *Journal of Membrane Science* **1991**, *62*, 165-85.

(6) Cornelius, C. J.; Marand, E. *Journal of Membrane Science* **2002**, *202*, 97-118.

(7) Kong, Y.; Du, H.; Yang, J.; Shi, D.; Wang, Y.; Zhang, Y.; Xin, W. *Desalination* **2002**, *146*, 49-55.

(8) Mahajan, R.; Burns, R.; Schaeffer, M.; Koros, W. J. *Journal of Applied Polymer Science* **2002**, *86*, 881-890.

(9) Mahajan, R.; Koros, W. J. *Industrial & Engineering Chemistry Research* **2000**, *39*, 2692-2696.

(10) Pechar, T. W.; Tsapatsis, M.; Marand, E.; Davis, R. *Desalination* **2002**, *146*, 3-9.

(11) Zimmerman, C. M.; Mahajan, R.; Koros, W. J. *Polymeric Materials Science and Engineering* **1997**, *77*, 328-329.

(12) Chung, T.-S.; Jiang, L. Y.; Li, Y.; Kulprathipanja, S. *Progress in Polymer Science* **2007**, *32*, 483-507.

(13) Okada, A.; Usuki, A. *Society of Automotive Engineers, [Special Publication] SP* **2007**, *SP-2113*, 49-60.

(14) Cussler, E. L. *Journal of Membrane Science* **1990**, *52*, 275-88.

(15) *Novel Approaches to Carbon Management: Separation, Capture, Sequestration, and conversion to Useful Products*; The National Academy Press, 2003.

(16) Ockwig, N. W.; Nenoff, T. M. *Chemical Reviews* **2007**, *107*, 4078-4110.

(17) Bates, F. S.; Fredrickson, G. H. *Annual Review of Physical Chemistry* **1990**, *41*, 525-57.

(18) Bates, F. S.; Fredrickson, G. H. *Physics Today* **1999**, *52*, 32-38.

(19) Szwarc, M.; Levy, M.; Milkovich, R. *J. Am. Chem. Soc.* **1956**, *78*, 2656-2657.

(20) Braunecker, W. A.; Matyjaszewski, K. *Progress in Polymer Science* **2007**, *32*, 93-146.

(21) Bielawski, C. W.; Grubbs, R. H. *Progress in Polymer Science* **2007**, *32*, 1-29.

(22) Leibler, L. *Macromolecules* **1980**, *13*, 1602-1617.

(23) Khandpur, A. K.; Forster, S.; Bates, F. S.; Hamley, I. W.; Ryan, A. J.; Bras, W.; Almdal, K.; Mortensen, K. *Macromolecules* **1995**, *28*, 8796-8806.

(24) Fredrickson, G. H.; Helfand, E. *J. Chem. Phys* **1987**, *87*, 697-705.

(25) Matsen, M. W.; Bates, F. S. *Macromolecules* **1996**, *29*, 1091-1098.

(26) Matsen, M. W.; Bates, F. S. *J. Chem. Phys.* **1997**, *106*, 2436-2448.

(27) Matsen, M. W.; Schick, M. *Phys. Rev. Lett.* **1994**, *72*, 2660-2663.

(28) Matsen, M. W.; Thompson, R. B. *J. Chem. Phys.* **1999**, *111*, 7139-7146.

(29) Bailey, T. S., University of Minnesota, 2001.

(30) Adhikari, R.; Michler, G. H. *Progress in Polymer Science* **2004**, *29*, 949-986.

(31) Hermel, T. J.; Hahn, S. F.; Chaffin, K. A.; Gerberich, W. W.; Bates, F. S. *Macromolecules* **2003**, *36*, 2190-2193.

(32) Honeker, C. C.; Thomas, E. L. *Chemistry of Materials* **1996**, *8*, 1702-1714.

(33) Kawai, H.; Hashimoto, T.; Miyoshi, K.; Uno, H.; Fujimura, M. *Journal of Macromolecular Science, Physics* **1980**, *B17*, 427-72.

(34) Gehlsen, M. D.; Almdal, K.; Bates, F. S. *Macromolecules* **1992**, *25*, 939-43.

(35) Mori, Y.; Lim, L. S.; Bates, F. S. *Macromolecules* **2003**, *36*, 9879-9888.

(36) Qiao, L.; Leibig, C.; Hahn, S. F.; Winey, K. I. *Industrial & Engineering Chemistry Research* **2006**, *45*, 5598-5602.

(37) Hiemenz, P. C.; Lodge, T. P. *Polymer Chemistry, Draft of 2nd edition*, 2005.

(38) Koo, C. M.; Wu, L.; Lim, L. S.; Mahanthappa, M. K.; Hillmyer, M. A.; Bates, F. S. *Macromolecules* **2005**, *38*, 6090-6098.

(39) Rickle, G. K. *Journal of Polymer Science, Part A: Polymer Chemistry* **1993**, *31*, 113-21.

(40) Sheffel, J. A.; Tsapatsis, M. *Journal of Membrane Science* **2009**, *326*, 595-607.

(41) Cavicchi, K. A.; Lodge, T. P. *Macromolecules* **2003**, *36*, 7158-7164.

(42) Pangborn, A. B.; Giardello, M. A.; Grubbs, R. H.; Rosen, R. K.; Timmers, F. J. *Organometallics* **1996**, *15*, 1518-20.

(43) Chu, J. H.; Rangarajan, P.; Adams, J. L.; Register, R. A. *Polymer* **1995**, *36*, 1569-75.

(44) Fragouli, P. G.; Iatrou, H.; Hadjichristidis, N. *Journal of Polymer Science, Part A: Polymer Chemistry* **2004**, *42*, 514-519.

(45) Zilliox, J. G.; Roovers, J. E. L.; Bywater, S. *Macromolecules* **1975**, *8*, 573-8.

(46) Fetters, L. J.; Lohse, D. J.; Richter, D.; Witten, T. A.; Zirkel, A. *Macromolecules* **1994**, *27*, 4639-4647.

(47) Epps, T. H., III; Bates, F. S. *Macromolecules* **2006**, *39*, 2676-2682.

(48) Hermel, T. J.; Wu, L.; Hahn, S. F.; Lodge, T. P.; Bates, F. S. *Macromolecules* **2002**, *35*, 4685-4689.

(49) Koppi, K. A. Ph.D. Thesis, University of Minnesota, 1993.

(50) Pye, D. G.; Hoehn, H. H.; Panar, M. *Journal of Applied Polymer Science* **1976**, *20*, 1921-31.

(51) Moore, T. T.; Damle, S.; Williams, P. J.; Koros, W. J. *Journal of Membrane Science* **2004**, *245*, 227-231.

(52) Epps, T. H., III; Cochran, E. W.; Bailey, T. S.; Waletzko, R. S.; Hardy, C. M.; Bates, F. S. *Macromolecules* **2004**, *37*, 8325-8341.

(53) Csernica, J.; Baddour, R. F.; Cohen, R. E. *Macromolecules* **1987**, *20*, 2468-71.

(54) Csernica, J.; Baddour, R. F.; Cohen, R. E. *Macromolecules* **1990**, *23*, 1429-33.

(55) Wang, J.; DeRocher, J. P.; Wu, L.; Bates, F. S.; Cussler, E. L. *Journal of Membrane Science* **2006**, *270*, 13-21.

(56) Lape, N. K.; Mao, H.; Camper, D.; Hillmyer, M. A.; Cussler, E. L. *Journal of Membrane Science* **2005**, *259*, 1-9.

(57) Brandrup, J.; Immergut, E. H.; Editors *Polymer Handbook, Fourth Edition*, 1998.

(58) Bates, F. S.; Fredrickson, G. H.; Hucul, D.; Hahn, S. F. *AIChe Journal* **2001**, *47*, 762-765.

(59) Gehlsen, M. D.; Bates, F. S. *Macromolecules* **1993**, *26*, 4122-4127.

(60) Hucul, D. A.; Hahn, S. F. *Adv. Mater.* **2000**, *12*, 1855-1858.

(61) Ryu, C. Y.; Ruokolainen, J.; Fredrickson, G. H.; Kramer, E. J.; Hahn, S. F. *Macromolecules* **2002**, *35*, 2157-2166.

(62) Patel, R. M.; Hahn, S. F.; Esneault, C.; Bensason, S. *Advanced Materials* **2000**, *12*, 1813-1817.

(63) Balsara, N. P.; Fetters, L. J.; Hadjichristidis, N.; Lohse, D. J.; Han, C. C.; Graessley, W. W.; Krishnamoorti, R. *Macromolecules* **1992**, *25*, 6137-47.

(64) Zhao, J.; Majumdar, B.; Schulz, M. F.; Bates, F. S.; Almdal, K.; Mortensen, K.; Hajduk, D. A.; Gruner, S. M. *Macromolecules* **1996**, *29*, 1204-1215.

(65) Schweizer, K. S.; Curro, J. G. *Macromolecules* **1988**, *21*, 3070-81.

(66) Rosedale, J. H.; Bates, F. S.; Almdal, K.; Mortensen, K.; Wignall, G. D. *Macromolecules* **1995**, *28*, 1429-1443.

(67) Mayes, A. M.; delaCruz, M. O. *J. Chem. Phys.* **1989**, *91*, 7228-7235.

(68) Maurer, W. W.; Bates, F. S.; Lodge, T. P.; Almdal, K.; Mortensen, K.; Fredrickson, G. H. *Journal of Chemical Physics* **1998**, *108*, 2989-3000.

(69) Liu, A. J.; Fredrickson, G. H. *Macromolecules* **1992**, *25*, 5551-3.

(70) Krishnamoorti, R.; Graessley, W. W.; Fetters, L. J.; Garner, R. T.; Lohse, D. J. *Macromolecules* **1995**, *28*, 1252-9.

(71) Graessley, W. W.; Krishnamoorti, R.; Reichart, G. C.; Balsara, N. P.; Fetters, L. J.; Lohse, D. J. *Macromolecules* **1995**, *28*, 1260-70.

(72) Gehlsen, M. D.; Bates, F. S. *Macromolecules* **1994**, *27*, 3611-18.

(73) Dudowicz, J.; Freed, K. F. *Journal of Chemical Physics* **1994**, *100*, 4653-64.

(74) David, E. F.; Schweizer, K. S. *Macromolecules* **1997**, *30*, 5118-5132.

(75) David, E. F.; Schweizer, K. S. *Macromolecules* **1995**, *28*, 3980-94.

(76) Cochran, E. W.; Bates, F. S. *Macromolecules* **2002**, *35*, 7368-7374.

(77) Bates, F. S.; Schulz, M. F.; Rosedale, J. H.; Almdal, K. *Macromolecules* **1992**, *25*, 5547-50.

(78) Bates, F. S.; Fredrickson, G. H. *Macromolecules* **1994**, *27*, 1065-7.

(79) Steinhoff, B.; Ruellmann, M.; Wenzel, M.; Junker, M.; Alig, I.; Oser, R.; Stuehn, B.; Meier, G.; Diat, O.; Boesecke, P.; Stanley, H. B. *Macromolecules* **1998**, *31*, 36-40.

(80) Schwahn, D.; Frielinghaus, H.; Mortensen, K.; Almdal, K. *Macromolecules* **2001**, *34*, 1694-1706.

(81) Frielinghaus, H.; Schwahn, D.; Mortensen, K.; Almdal, K.; Springer, T. *Macromolecules* **1996**, *29*, 3263-71.

(82) Beiner, M.; Fytas, G.; Meier, G.; Kumar, S. K. *Physical Review Letters* **1998**, *81*, 594-597.

(83) Weidisch, R.; Stamm, M.; Schubert, D. W.; Arnold, M.; Budde, H.; Hoering, S. *Macromolecules* **1999**, *32*, 3405-3411.

(84) Russell, T. P.; Karis, T. E.; Gallot, Y.; Mayes, A. M. *Nature* **1994**, *368*, 729-31.

(85) Hashimoto, T.; Hasegawa, H.; Hashimoto, T.; Katayama, H.; Kamigaito, M.; Sawamoto, M.; Imai, M. *Macromolecules* **1997**, *30*, 6819-6825.

(86) Ryu, D. Y.; Lee, D. H.; Jeong, U.; Yun, S.-H.; Park, S.; Kwon, K.; Sohn, B.-H.; Chang, T.; Kim, J. K.; Russell, T. P. *Macromolecules* **2004**, *37*, 3717-3724.

(87) Ryu, D. Y.; Jeong, U.; Kim, J. K.; Russell, T. P. *Nature Materials* **2002**, *1*, 114-117.

(88) Li, C.; Lee, D. H.; Kim, J. K.; Ryu, D. Y.; Russell, T. P. *Macromolecules* **2006**, *39*, 5926-5930.

(89) Phatak, A.; Lim, L. S.; Reaves, C. K.; Bates, F. S. *Macromolecules* **2006**, *39*, 6221-6228.

(90) Almdal, K.; Hillmyer, M. A.; Bates, F. S. *Macromolecules* **2002**, *35*, 7685-7691.

(91) Ndoni, S.; Papadakis, C. M.; Bates, F. S.; Almdal, K. *Review of Scientific Instruments* **1995**, *66*, 1090-5.

(92) Gehlsen, M. D. Ph.D. Thesis, University of Minnesota, 1993.

(93) Rosedale, J. H.; Bates, F. S. *Macromolecules* **1990**, *23*, 2329-2338.

(94) Schwahn, D.; Hahn, K.; Streib, J.; Springer, T. *Journal of Chemical Physics* **1990**, *93*, 8383-91.

(95) Scheffold, F.; Eiser, E.; Budkowski, A.; Steiner, U.; Klein, J.; Fetters, L. J. *Journal of Chemical Physics* **1996**, *104*, 8786-8794.

(96) Hildebrand, J. H.; Scott, R. L. *The Solubility of Nonelectrolytes. 3rd ed*; Van Nostrand-Reinhold: Princeton, NJ, 1950.

(97) Graessley, W. W.; Krishnamoorti, R.; Balsara, N. P.; Fetters, L. J.; Lohse, D. J.; Schulz, D. N.; Sissano, J. A. *Macromolecules* **1993**, *26*, 1137-43.

(98) Graessley, W. W.; Krishnamoorti, R.; Balsara, N. P.; Fetters, L. J.; Lohse, D. J.; Schulz, D. N.; Sissano, J. A. *Macromolecules* **1994**, *27*, 2574-9.

(99) Krishnamoorti, R.; Graessley, W. W.; Balsara, N. P.; Lohse, D. J. *Macromolecules* **1994**, *27*, 3073-81.

(100) Singh, C.; Schweizer, K. S. *Macromolecules* **1997**, *30*, 1490-1508.

(101) Schweizer, K. S.; Singh, C. *Macromolecules* **1995**, *28*, 2063-80.

(102) Fredrickson, G. H.; Liu, A. J.; Bates, F. S. *Macromolecules* **1994**, *27*, 2503-11.

(103) Dudowicz, J.; Freed, K. F. *Macromolecules* **1993**, *26*, 213-20.

(104) Freed, K. F.; Dudowicz, J. *Macromolecules* **1996**, *29*, 625-36.

(105) Dudowicz, J.; Freed, M. S.; Freed, K. F. *Macromolecules* **1991**, *24*, 5096-111.

(106) Dudowicz, J.; Freed, K. F. *Macromolecules* **1991**, *24*, 5076-95.

(107) Kloprogge, J. T. *Journal of Porous Materials* **1998**, *5*, 5-41.

(108) Pinnavaia, T. J. *Science* **1983**, *220*, 365-71.

(109) Yu, J.; Xu, R. *Accounts of Chemical Research* **2003**, *36*, 481-490.

(110) Ma, R.; Liu, Z.; Li, L.; Iyi, N.; Sasaki, T. *Journal of Materials Chemistry* **2006**, *16*, 3809-3813.

(111) Jeong, H.-K.; Nair, S.; Vogt, T.; Dickinson, L. C.; Tsapatsis, M. *Nature materials* **2003**, *2*, 53-8.

(112) Leonowicz, M. E.; Lawton, J. A.; Lawton, S. L.; Rubin, M. K. *Science* **1994**, *264*, 1910-13.

(113) Clearfield, A. *Chemical Reviews* **1988**, *88*, 125-48.

(114) Corma, A.; Fornes, V.; Pergher, S. B.; Maesen, T. L. M.; Buglass, J. G. *Nature (London)* **1998**, *396*, 353-356.

(115) Laforge, S.; Ayrault, P.; Martin, D.; Guisnet, M. *Applied Catalysis, A: General* **2005**, *279*, 79-88.

(116) Giannelis, E. P. *Advanced Materials* **1996**, *8*, 29-35.

(117) Ikeda, T.; Akiyama, Y.; Oumi, Y.; Kawai, A.; Mizukami, F. *Angewandte Chemie, International Edition* **2004**, *43*, 4892-4896, S4892/1-S4892/13.

(118) Li, Z.; Marler, B.; Gies, H. *Chemistry of Materials* **2008**, *20*, 1896-1901.

(119) Marler, B.; Stroeter, N.; Gies, H. *Microporous and Mesoporous Materials* **2005**, *83*, 201-211.

(120) Millini, R.; Carluccio, L. C.; Carati, A.; Bellussi, G.; Perego, C.; Cruciani, G.; Zanardi, S. *Microporous and Mesoporous Materials* **2004**, *74*, 59-71.

(121) Oberhagemann, U.; Bayat, P.; Marler, B.; Gies, H.; Rius, J. *Angewandte Chemie, International Edition in English* **1997**, *35*, 2869-2872.

(122) Schreyeck, L.; Caullet, P.; Mougenel, J. C.; Guth, J. L.; Marler, B. *Microporous Materials* **1996**, *6*, 259-271.

(123) Zanardi, S.; Alberti, A.; Cruciani, G.; Corma, A.; Fornes, V.; Brunelli, M. *Angewandte Chemie, International Edition* **2004**, *43*, 4933-4937.

(124) Choi, S.; Coronas, J.; Jordan, E.; Oh, W.; Nair, S.; Onorato, F.; Shantz, D. F.; Tsapatsis, M. *Angewandte Chemie, International Edition* **2008**, *47*, 552-555.

(125) Schenkel, R.; Barth, J. O.; Kornatowski, J.; Lercher, J. A. *Studies in Surface Science and Catalysis* **2002**, *142A*, 69-76.

(126) Wu, P.; Nuntasri, D.; Ruan, J.; Liu, Y.; He, M.; Fan, W.; Terasaki, O.; Tatsumi, T. *Journal of Physical Chemistry B* **2004**, *108*, 19126-19131.

(127) Zubowa, H.-L.; Schneider, M.; Schreier, E.; Eckelt, R.; Richter, M.; Fricke, R. *Microporous and Mesoporous Materials* **2008**, *109*, 317-326.

(128) Yu, J.; Li, J.; Sugiyama, K.; Togashi, N.; Terasaki, O.; Hiraga, K.; Zhou, B.; Qiu, S.; Xu, R. *Chemistry of Materials* **1999**, *11*, 1727-1732.

(129) Huang, Q.; Wang, W.; Yue, Y.; Hua, W.; Gao, Z. *Microporous and Mesoporous Materials* **2004**, *67*, 189-194.

(130) Peng, L.; Yu, J.; Li, J.; Li, Y.; Xu, R. *Chemistry of Materials* **2005**, *17*, 2101-2107.

(131) Ravishankar, R.; Bhattacharya, D.; Jacob, N. E.; Sivasanker, S. *Microporous Materials* **1995**, *4*, 83-93.

(132) Choi, J.; Lai, Z.; Ghosh, S.; Beving, D. E.; Yan, Y.; Tsapatsis, M. *Industrial & Engineering Chemistry Research* **2007**, *46*, 7096-7106.

(133) Tsapatsis, M. *Report to DOE* **2008**.

(134) Ray, S. S.; Okamoto, M. *Progress in Polymer Science* **2003**, *28*, 1539-1641.

(135) Kresge, C. T.; Roth, W. J. US Patent 5266541, 1993.

(136) Kresge, C. T.; Roth, W. J. US Patent 5278115, 1994.

(137) Kresge, C. T.; Roth, W. J.; Simmons, K. G.; Vartuli, J. C. WO Patent 9211935, 1992.

(138) Corma, A.; Fornes, V.; Martinez-Triguero, J.; Pergher, S. B. *Journal of Catalysis* **1999**, *186*, 57-63.

(139) Corma, A.; Diaz, U.; Fornes, V.; Guil, J. M.; Martinez-Triguero, J.; Creyghton, E. J. *Journal of Catalysis* **2000**, *191*, 218-224.

(140) Chu, C. T.; Husain, A.; Huss, A., Jr.; Kresge, C. T.; Roth, W. J. U.S. Patent 5258569 1993.

(141) Hellring, S. D.; Huss, A., Jr.; Landis, M. E.; Marler, D. O.; Teitman, G. J.; Timken, H. K. C.; Trewella, J. C. US Patent 5639931 1997.

(142) Barth, J.-O.; Kornatowski, J.; Lercher, J. A. *Journal of Materials Chemistry* **2002**, *12*, 369-373.

(143) Roth, W. J.; Vartuli, J. C. *Studies in Surface Science and Catalysis* **2002**, *141*, 273-279.

(144) Aiello, R.; Crea, F.; Testa, F.; Demortier, G.; Lentz, P.; Wiame, M.; Nagy, J. B. *Microporous and Mesoporous Materrials* **2000**, *35-36*, 585-595.

(145) Camblor, M. A.; Corma, A.; Diaz-Cabanas, M.-J.; Baerlocher, C. *Journal of Physical Chemistry B* **1998**, *102*, 44-51.

(146) Kennedy, G. J.; Lawton, S. L.; Rubin, M. K. *Journal of the American Chemical Society* **1994**, *116*, 11000-3.

(147) Lawton, S. L.; Fung, A. S.; Kennedy, G. J.; Alemany, L. B.; Chang, C. D.; Hatzikos, G. H.; Lissy, D. N.; Rubin, M. K.; Timken, H.-K. C.; et al. *Journal of Physical Chemistry* **1996**, *100*, 3788-98.

(148) Vuono, D.; Pasqua, L.; Testa, F.; Aiello, R.; Fonseca, A.; Koranyi, T. I.; Nagy, J. B. *Microporous and Mesoporous Materials* **2006**, *97*, 78-87.

(149) Camblor, M. A.; Corell, C.; Corma, A.; Diaz-Cabanas, M.-J.; Nicolopoulos, S.; Gonzalez-Calbet, J. M.; Vallet-Regi, M. *Chemistry of Materials* **1996**, *8*, 2415-2417.

(150) Kennedy, G. J.; Lawton, S. L.; Fung, A. S.; Rubin, M. K.; Steuernagel, S. *Catalysis Today* **1999**, *49*, 385-399.

(151) Dorset, D. L.; Roth, W. J.; Gilmore, C. J. *Acta Crystallographica, Section A: Foundations of Crystallography* **2005**, *A61*, 516-527.

(152) Hunger, M.; Ernst, S.; Weitkamp, J. *Zeolites* **1995**, *15*, 188-92.

(153) Kolodziejski, W.; Zicovich-Wilson, C.; Corell, C.; Perez-Pariente, J.; Corma, A. *Journal of Physical Chemistry* **1995**, *99*, 7002-8.

(154) Ma, D.; Deng, F.; Fu, R.; Han, X.; Bao, X. *Journal of Physical Chemistry B* **2001**, *105*, 1770-1779.

(155) Burkett, S. L.; Davis, M. E. *Journal of Physical Chemistry B* **1994**, *98*, 4647-53.

(156) He, Y. J.; Nivarthy, G. S.; Eder, F.; Seshan, K.; Lercher, J. A. *Microporous and Mesoporous Materials* **1998**, *25*, 207-224.

(157) Roth, W. J.; Kresge, C. T.; Vartuli, J. C.; Leonowicz, M. E.; Fung, A. S.; McCullen, S. B. *Studies in Surface Science and Catalysis* **1995**, *94*, 301-8.

(158) Fornes, T. D.; Yoon, P. J.; Keskkula, H.; Paul, D. R. *Polymer* **2001**, *42*, 09929-09940.

(159) Wang, Z.; Wang, H.; Mitra, A.; Huang, L.; Yan, Y. *Advanced Materials* **2001**, *13*, 746-749.

(160) Mitra, A.; Wang, Z.; Cao, T.; Wang, H.; Huang, L.; Yan, Y. *Journal of the Electrochemical Society* **2002**, *149*, B472-B478.

(161) Giannakopoulos, I. G.; Kouzoudis, D.; Grimes, C. A.; Nikolakis, V. *Advanced Functional Materials* **2005**, *15*, 1165-1170.

(162) Coronas, J.; Santamaria, J. *Topics in Catalysis* **2004**, *29*, 29-44.

(163) van den Berg, A. W. C.; Bromley, S. T.; Flikkema, E.; Wojdel, J.; Maschmeyer, T.; Jansen, J. C. *Journal of Chemical Physics* **2004**, *120*, 10285-10289.

(164) Maheshwari, S.; Jordan, E.; Kumar, S.; Bates, F. S.; Penn, R. L.; Shantz, D. F.; Tsapatsis, M. *Journal of the American Chemical Society* **2008**, *130*, 1507-1516.

(165) Leach, E. S. H.; Hopkinson, A.; Franklin, K.; Van Duijneveldt, J. S. *Langmuir* **2005**, *21*, 3821-3830.

(166) Ida, S.; Shiga, D.; Koinuma, M.; Matsumoto, Y. *Journal of the American Chemical Society* **2008**, *130*, 14038-14039.

(167) Ma, R.; Takada, K.; Fukuda, K.; Iyi, N.; Bando, Y.; Sasaki, T. *Angewandte Chemie, International Edition* **2008**, *47*, 86-89.

(168) Snyder, M. A.; Lee, J. A.; Davis, T. M.; Scriven, L. E.; Tsapatsis, M. *Langmuir* **2007**, *23*, 9924-9928.

(169) Dennis, H. R.; Hunter, D. L.; Chang, D.; Kim, S.; White, J. L.; Cho, J. W.; Paul, D. R. *Polymer* **2001**, *42*, 9513-9522.

(170) Brandao, L. S.; Mendes, L. C.; Medeiros, M. E.; Sirelli, L.; Dias, M. L. *Journal of Applied Polymer Science* **2006**, *102*, 3868-3876.

(171) Chen, G.; Chen, X.; Wang, H.; Wu, D. *Journal of Applied Polymer Science* **2007**, *103*, 3470-3475.

(172) Ray, S. S.; Maiti, P.; Okamoto, M.; Yamada, K.; Ueda, K. *Macromolecules* **2002**, *35*, 3104-3110.

(173) Zhou, Z.; Zhai, H.; Xu, W.; Guo, H.; Liu, C.; Pan, W.-P. *Journal of Applied Polymer Science* **2006**, *101*, 805-809.

(174) Verreck, G.; Decorte, A.; Li, H.; Tomasko, D.; Arien, A.; Peeters, J.; Rombaut, P.; Van den Mooter, G.; Brewster, M. E. *Journal of Supercritical Fluids* **2006**, *38*, 383-391.

(175) Mahajan, R.; Koros, W. J. *Polymer Engineering and Science* **2002**, *42*, 1420-1431.

(176) Ho, D. L.; Glinka, C. J. *Chemistry of Materials* **2003**, *15*, 1309-1312.

(177) Wang, B.; Wu, J.; Yuan, Z.; Xiang, S. *Cuihua Xuebao* **2009**, *30*, 60-64.